

# Impact of wind shear on aerosol–cloud interactions and convective precipitation

Master's Thesis in Meteorology  
by

**Mathis Tonn**

November 2023



INSTITUTE OF METEOROLOGY AND CLIMATE RESEARCH (IMK)  
KARLSRUHE INSTITUTE OF TECHNOLOGY (KIT)

Advisor:

Prof. Dr. Corinna Hoose

Co-Advisor:

Prof. Dr. Michael Kunz



*This document is licenced under the Creative Commons Attribution-ShareAlike 4.0 International Licence.*

# Abstract

This study deals with the impact of wind shear on convective precipitation and aerosol–cloud interactions based on ICON real-case simulations. Therefore, three convective active days are simulated with a 1-km ICON grid, two of them from the Swabian MOSES 2021 field campaign. To study the impact of the vertical wind shear, the simulations for each day are performed with the reference shear from the initial and boundary data but also with increased and decreased initial wind shear. For the aerosol effects, model output for four different concentrations of cloud condensation nuclei (CCNs) is generated. Besides the simulations, radar data from the German Weather Service and soundings from the Swabian MOSES field campaign are used to compare the model output with observations.

For the analysis of the real-case simulations, spatial averages of several atmospheric variables over Germany and some bordering regions are used to explain precipitation in this area. For some explanations, also variables averaged over the domain of the Swabian MOSES campaign are utilized. A higher potential for convection is always found for stronger wind shear. But nevertheless, no generally valid statement can be made for the effect of wind shear on convective precipitation. On one simulation day, the precipitation amount systematically increases with increasing wind shear, and on the other two days, it decreases. Therefore, many different atmospheric variables are shown for each day in the present work to give an overview of atmospheric conditions leading to the individual precipitation response.

The precipitation amount clearly varies less for varying CCN concentration than for varying wind shear. As for the shear dependency, there is no clear systematic behavior of the CCN dependency of total precipitation as all different shear realizations show an increase in precipitation for increasing CCN concentration on one day and a decrease on the other day, some an increase and some a decrease on the third day. The magnitude of the CCN sensitivity is not influenced in a systematic way by the vertical wind shear. The vertically integrated hydrometeor variables and microphysical process rates behave more similarly on the three simulation days than precipitation. They are used together with some similar atmospheric variables as before and vertical profiles to explain the precipitation response of the different simulations. At the end of the model output evaluations, the precipitation efficiency, the

---

relation of precipitation and precipitation generation, is shown. The precipitation efficiencies behave very similarly on each day with increasing values for increasing CCN concentration. This CCN sensitivity is stronger the greater the vertical wind shear is. The thesis closes with an outlook on how further research could look like following from the mostly individual results for the different simulation days in this work.

# Zusammenfassung

Die vorliegende Arbeit beschäftigt sich mit dem Einfluss der Windscherung auf konvektiven Niederschlag und Aerosol–Wolke–Wechselwirkungen basierend auf realen Simulationen mit dem Modell ICON. Dafür werden drei Tage mit konvektiver Aktivität mit 1 km Auflösung simuliert, wobei zwei der Tage aus dem Zeitraum der Swabian MOSES Messkampagne von 2021 sind. Um den Einfluss der vertikalen Windscherung zu untersuchen, werden die Simulationen für jeden Tag mit der Referenzscherung aus den Anfangs- und Randdaten, aber auch mit vergrößerter und verringerter vertikaler Windscherung erzeugt. Für die Aerosol Effekte werden Simulationen mit vier verschiedenen Konzentrationen an Kondensationskeimen für Wolken (*cloud condensation nuclei*: CCNs) erstellt. Neben den Simulationen werden auch Radardaten vom Deutschen Wetterdienst und Radiosondenaufstiege von der Swabian MOSES Messkampagne genutzt, um die Ergebnisse der Simulationen mit Beobachtungsdaten zu vergleichen.

Für die Analyse der realen Simulationen werden verschiedene atmosphärische Variablen, räumlich gemittelt über Deutschland und angrenzende Regionen, verwendet, um den Niederschlag in diesem Gebiet zu erklären. Für manche Erklärungen werden auch über das Gebiet der Swabian MOSES Kampagne gemittelte Variablen gezeigt. Ein höheres Konvektionspotential tritt an allen Simulationstagen für stärkere Windscherung auf. Allerdings kann keine generelle Aussage darüber getroffen werden, wie sich die Windscherung auf den konvektiven Niederschlag auswirkt. An einem Simulationstag wächst die Niederschlagsmenge systematisch für ansteigende Windscherung, wohingegen sie an den beiden anderen Tagen systematisch sinkt. Infolgedessen werden in der vorliegenden Arbeit viele verschiedene atmosphärische Variablen für die einzelnen Tage gezeigt, um einen Überblick darüber zu geben, wie die Atmosphärenbedingungen sind, die zu den einzelnen Niederschlagsmengen führen.

Die Niederschlagsmenge verändert sich eindeutig weniger bei sich verändernder CCN-Konzentration als bei sich verändernder Windscherung. Wie bei der Abhängigkeit

---

von der Scherung gibt es keine eindeutige systematische Abhängigkeit des Niederschlags von der CCN-Konzentration, nachdem die verschiedenen Windscherungssimulationen alle mehr Niederschlag für mehr CCNs an einem Tag, alle weniger Niederschlag am anderen Tag und manche mehr, manche weniger Niederschlag am dritten Tag zeigen. Dabei ist die Größe der CCN-Sensitivität nicht systematisch von der vertikalen Windscherung abhängig. Die vertikal integrierten Hydrometeormengen und mikrophysikalischen Prozessraten verhalten sich ähnlicher an den drei Simulationstagen als der Niederschlag. Zusammen mit ähnlichen atmosphärischen Variablen wie zuvor und Vertikalprofilen werden Hydrometeormengen und Prozessraten dazu genutzt, den Niederschlag der verschiedenen Simulationen zu erklären. Am Ende der Auswertungen wird die Niederschlagseffizienz, welche sich als das Verhältnis von Niederschlag und Erzeugung von Niederschlag berechnet, gezeigt. Diese verhält sich an allen drei Tagen sehr ähnlich, wobei die Werte für wachsende CCN-Konzentration zunehmen. Dieser Effekt ist stärker, je größer die vertikale Windscherung ist. Die Arbeit schließt mit einem Ausblick darauf, wie in Anbetracht der Ergebnisse der vorliegenden Studie zukünftige Forschung aussehen könnte.

# Contents

<b>1</b>	<b>Introduction</b>	<b>1</b>
<b>2</b>	<b>Theoretical Background</b>	<b>3</b>
2.1	Deep convection . . . . .	3
2.1.1	Potential and equivalent potential temperature . . . . .	3
2.1.2	Lapse rate of a lifted air parcel . . . . .	5
2.1.3	Atmospheric stability . . . . .	6
2.1.4	Convective measures . . . . .	7
2.1.5	Convective cells . . . . .	9
2.2	Aerosol–cloud interactions . . . . .	14
2.2.1	Formation of cloud droplets . . . . .	14
2.2.2	Formation of raindrops . . . . .	16
2.2.3	Albedo and lifetime effect . . . . .	17
2.2.4	Aerosol–cloud interactions in convective clouds . . . . .	17
<b>3</b>	<b>Data basis and processing</b>	<b>21</b>
3.1	Swabian MOSES 2021 field campaign . . . . .	21
3.2	ICON simulations . . . . .	21
3.3	Data for comparison of model output with reality . . . . .	26
<b>4</b>	<b>Observed precipitation on simulation days</b>	<b>29</b>
4.1	23 June 2021 . . . . .	29
4.2	28 June 2021 . . . . .	30
4.3	22 July 2015 . . . . .	31
<b>5</b>	<b>Impact of wind shear on convective precipitation and ACI</b>	<b>33</b>
5.1	Effect on convective precipitation . . . . .	33
5.1.1	Case of 23 June 2021 . . . . .	33
5.1.2	Case of 28 June 2021 . . . . .	38
5.1.3	Case of 22 July 2015 . . . . .	43
5.1.4	General conclusions . . . . .	46
5.2	Effect on ACI . . . . .	47
5.2.1	Case of 23 June 2021 . . . . .	48

5.2.2	Case of 28 June 2021 . . . . .	52
5.2.3	Case of 22 July 2015 . . . . .	55
5.2.4	General conclusions . . . . .	60
5.3	Precipitation efficiency . . . . .	60
<b>6</b>	<b>Conclusion and discussion</b>	<b>65</b>
	<b>Bibliography</b>	<b>I</b>

# 1. Introduction

Convective clouds and storms are not only fascinating in terms of their appearance. They are often associated with severe weather like hail, heavy rain or severe wind gusts. Therefore, they pose a risk to human health and often cause large damage to infrastructure, buildings, vehicles and agriculture. As an example, one very intense event occurred at the end of July 2013. There was a series of heavy thunderstorms over Germany, including supercells with hail. One of the cells produced hail with a diameter of 10 cm along a path of 120 km which also hit the densely populated region of Stuttgart and therefore caused damage of more than EUR 1 billion (Kunz et al., 2018). The whole event, defined for a period of 72 hours, led to insured loss of around EUR 2.8 billion and total economic loss of around EUR 3.5 billion (SwissRe, 2014).

During a three-day period around 23 June 2021, severe hailstorms occurred over southern Germany, France, Switzerland, Austria and Czech Republic. They caused a total insured loss of around EUR 4 billion as they were associated with hail of maximum diameters of 4 cm, hail accumulations on the ground of around 30 cm depth in maximum and heavy rainfall, which led to flooding (Kunz et al., 2022). There were many more severe convective events in the past years, which could be listed here. However, the point is only to illustrate how large the damage can be, which is why a successful forecast of such events is of great importance.

Over the past decades, the forecast skill of numerical weather prediction (NWP) models has largely improved. Nowadays, more observational data are available, which are assimilated in a better way. Furthermore, a higher computing power is available. This led to an improvement of the models, and simulations can be done with a higher resolution and with more appropriate parameterizations of sub-scale physical processes nowadays (Magnusson and Källén, 2013). Also ensemble modeling strategies are often used to get information about the accuracy of the model forecast (Buizza, 2019). However, the forecast of convective precipitation is still an ongoing challenge as it is influenced by many different aspects. The orography, heterogeneities of the land surface and the synoptic-scale flow determine the triggering of convection (Kirshbaum et al., 2018; Barthlott et al., 2022a). On the other side, the complex microphysics in the formation of cloud droplets when interacting with aerosols (aerosol–cloud interactions: ACI) are also a source of uncertainty for the prediction of convection (Seifert et al., 2012; Fan et al., 2013).

Therefore, many studies have been done in the past years to get a better understanding of how aerosols influence convective clouds and precipitation (e.g., Fan et al., 2016). Differences in the convection intensities for cleaner and more polluted conditions were the focus (e.g., Tao et al., 2007), sometimes in combination with

different variables like soil moisture content (e.g., Barthlott et al., 2022a; Schneider et al., 2019) or vertical wind shear (Fan et al., 2009). In this latter study, the authors found a dominant impact of the wind shear on the aerosol effects in convective clouds using idealized simulations. For strong wind shear, more aerosols reduce the amount of precipitation. However, for weak shear, more aerosols increase the amount of precipitation up to an optimum concentration. For higher concentrations, the precipitation amount decreases again. In the present study, this line of investigation is expanded by real-case simulations. Three days with convective activity are simulated, and both vertical wind shear and aerosol concentration are varied. Two of the days are from the Swabian MOSES (Modular Observation Solutions for Earth Systems) field campaign, which took place in the summer of 2021 in southwestern Germany. Due to the still ongoing challenge of forecasting convection, it is necessary to get a better insight in the event chain of convective storms, which was the goal of the measurement campaign together with the study of heat waves (Kunz et al., 2022). During the severe weather around 23 June 2021 mentioned above, measurements were taken as part of Swabian MOSES. Therefore, 23 June 2021 is the first simulation day, 28 June 2021, a day also with a supercell of smaller hail with a maximum diameter of 3 cm (Kunz et al., 2022), is the second simulation day. The third day is 22 July 2015, which was found in the data set of Tonn et al. (2023) as a day with supercells over Germany.

The thesis is structured as follows: In chapter 2, meteorological background information concerning deep convection and ACI is presented. First, it is described how convection can develop, by which measures it can be characterized, and in which form it can occur. Afterwards, an overview of how cloud droplets form microphysically using aerosols and how they grow into raindrops is given, and how aerosols affect cloud properties in general and in convective clouds in particular. After some information about the Swabian MOSES field campaign at the beginning of chapter 3, the model simulations and used observation data are described in this chapter, with emphasis on the former. In chapter 4, the precipitation observations for the three simulation days are described, which can give information about how well the simulations represent the reality. For the simulations in chapter 5, the focus is first on the effect of wind shear on convective precipitation. Therefore, the three simulation days are presented one after the other. Afterwards, the focus is on how the aerosol effects change with varying wind shear and how this has an effect again on the convective precipitation. Also the impact of wind shear and CCN concentration on precipitation efficiency is presented. The thesis closes with a summary of the main results and an outlook on future research in chapter 6.

## 2. Theoretical Background

This chapter deals with meteorological background relevant for the present thesis. First, the focus is on deep convection. Information about atmospheric stability is given and how deep convection can develop. Convective measures used in the context of atmospheric convection are presented, as well as different convective cells and their characteristics. Afterwards, ACI are introduced. It is presented how cloud droplets form using aerosols and how the droplets can grow into precipitation particles. The general effect on cloud albedo and lifetime is explained, as well as how different aerosol concentrations influence convective clouds.

### 2.1 Deep convection

According to Emanuel (1994), convection refers to those movements in the atmosphere that are related to the effect of a steady gravitational field upon density changes in a fluid. In meteorology, the vertical motion of air parcels due to buoyancy, characterized by vertical transport of mass, heat, water, momentum and vorticity, is called atmospheric convection (Lin et al., 2022). It is distinguished between shallow convection, which refers to cumulus clouds, and deep convection, which refers to thunderstorms in their different manifestations (Section 2.1.5).

The initiation of convection can be free or forced. In the case of free convection, the initiation occurs due to thermal buoyancy, e.g., as a consequence of strong heating of the air close to the ground or cold advection of air in higher levels. An air parcel is lifted dry adiabatically up to the level of free convection (LFC), above saturation is reached and condensation connected with release of latent heat takes place. The lifting occurs as long as the air parcel is positively buoyant. The height where the buoyancy becomes neutral is called the equilibrium level (EL). In the case of forced convection, an external influence, e.g., orography or near-surface convergence, forces the air to rise above a height, where lifting takes place due to buoyancy analogously to the free convection. This height is called lifting condensation level (LCL) (Markowski and Richardson, 2010).

Independent of the triggering mechanism, the stratification of the atmosphere is of great importance for the evolution of deep convection. To make a statement about the stability or instability of the atmospheric stratification, potential and equivalent potential temperature can be used.

#### 2.1.1 Potential and equivalent potential temperature

For the derivation of these quantities, the first law of thermodynamics

$$dU = \delta Q + \delta W = \delta Q - p d\alpha \quad (2.1)$$

is necessary (Vallis, 2017). This fundamental relation states that in a closed system, the change of the internal energy  $dU$  can be achieved through input of heat  $\delta Q$  or work done  $\delta W$ , expressed by the pressure  $p$  and the specific volume  $\alpha = \rho^{-1}$ . The preceding  $d$  expresses a total, and the  $\delta$  an inexact differential.

For the enthalpy  $h = U + p\alpha$  the differential  $dh$  becomes

$$dh = dU + p d\alpha + \alpha dp = \delta Q + \alpha dp. \quad (2.2)$$

by using equation 2.1. Assuming a dry ideal gas, which is a reasonable assumption for a dry atmosphere, the internal energy is only influenced by the temperature (Vallis, 2017). By inserting the ideal gas law

$$p\alpha = R_L T \quad (2.3)$$

with the specific gas constant  $R_L$  for dry air ( $R_L = 287.05 \text{ J kg}^{-1} \text{ K}^{-1}$ ) in equation 2.2, it becomes visible that  $dh$  is only a function of temperature:

$$dh = dU(T) + R_L dT = dh(T). \quad (2.4)$$

Therefore, it is possible to write

$$dh = \left( \frac{\partial h}{\partial T} \right)_p dT = c_p dT \quad (2.5)$$

with the heat capacity at constant pressure  $c_p$ . From equating the equations 2.2 and 2.5, the first law of thermodynamics results in

$$\delta Q = c_p dT - \alpha dp. \quad (2.6)$$

From this form of the first law of thermodynamics, the potential temperature can be derived. Dry adiabatic motion is assumed, which means that the process takes place without the exchange of heat ( $\delta Q = 0$ ). This is a necessary prerequisite as the potential temperature of an air parcel is defined as the temperature this parcel would have if it is lifted (and therefore expanded) or lowered (and therefore compressed) adiabatically to a reference pressure (Markowski and Richardson, 2010). After using the ideal gas law to replace  $\alpha$  and integrating of the modified version of equation 2.6, the potential temperature  $\theta$  can be written as

$$\theta = T \left( \frac{p_0}{p} \right)^\kappa. \quad (2.7)$$

with  $\kappa = R_L/c_p$  and the reference pressure  $p_0$ , which is usually chosen as 1000 hPa.

For the relevant convective processes, the assumption of dry adiabatic motion is no longer valid as the air parcel reaches saturation at the condensation level. Above, water vapor condenses, and latent heat is released ( $\delta Q \neq 0$ ). Equivalent potential temperature is therefore introduced as the temperature an air parcel would have if the latent heat released during the condensation of all the water vapor inside the parcel was converted into sensible heat (Trapp, 2013). The water is removed instantaneously as convection is assumed to be a pseudo-adiabatic process. The equivalent potential temperature  $\theta_e$  can be written according to Bolton (1980) as

$$\theta_e = T \left( \frac{1000}{p} \right)^{0,2854(1-0,28 \cdot 10^{-3}r)} \exp \left[ \left( \frac{3,376}{T_{\text{LCL}}} - 0,00254 \right) \cdot r(1+0,81 \cdot 10^{-3}r) \right]. \quad (2.8)$$

In this, the pressure  $p$  in hPa and the mixing ratio  $r$  in  $\text{g kg}^{-1}$  must be inserted,  $T_{\text{LCL}}$  is the temperature at the LCL in K. By connecting humidity and temperature in the equivalent potential temperature, this measure can be used as an indicator for atmospheric stability.

### 2.1.2 Lapse rate of a lifted air parcel

During the lifting of an air parcel, its temperature and therefore density changes. When combining the first law of thermodynamics and the hydrostatic approximation

$$\frac{dp}{dz} = -\rho g \quad (2.9)$$

where  $g$  describes the free fall acceleration due to gravity, the dry adiabatic lapse rate  $\Gamma_d$  is computed as the fraction of free fall acceleration and specific heat capacity (Markowski and Richardson, 2010):

$$\Gamma_d = -\frac{dT}{dz} = \frac{g}{c_p} = 0,98 \text{ K } (100 \text{ m})^{-1}. \quad (2.10)$$

Below the condensation level, the temperature of the air parcel is therefore reduced by around 1 K per 100 m. Above the condensation level, the cooling rate of the air parcel is reduced. This is a consequence of the latent heat release during condensation. From Clausius–Clapeyron equation, approximately

$$e_s \approx 6.112 \exp \frac{17.67T}{T + 243.5} \quad (2.11)$$

can be formulated. Herein,  $e_s$  is the saturation vapor pressure and  $T$  the temperature in °C. It becomes visible that warm air contains more water vapor at saturation than cold air (Markowski and Richardson, 2010). Therefore, the moist adiabatic lapse rate  $\Gamma_m$  is dependent on the actual air parcel temperature. In warmer air, the lapse rate

is smaller, and in colder air more similar to the dry adiabatic lapse rate.

### 2.1.3 Atmospheric stability

The atmospheric stratification can be described with the lapse rate of the environment around the air parcel  $\gamma_e$  or the vertical gradient of potential and equivalent potential temperature. Absolutely stable conditions occur for  $\gamma_e < \Gamma_m$ . A lifted parcel would get a lower temperature than the environment, leading to negative buoyancy independently of saturation. The potential and equivalent potential temperature increase with height within this type of stratification. In contrast, absolutely unstable conditions occur for  $\gamma_e > \Gamma_d$ . Even below saturation, the parcel stays warmer than the environment during lifting, leading to positive buoyancy. Potential and equivalent potential temperature both decrease with height for absolutely unstable conditions.

If  $\gamma_e$  is between  $\Gamma_m$  and  $\Gamma_d$ , the stratification is conditionally unstable. For a saturated air parcel, the atmosphere is unstable, and for an air parcel without saturation, stable. For conditional instability, the potential temperature increases with height while the equivalent potential temperature decreases. If the lapse rate of the environment is equal to the dry or moist adiabatic lapse rate, the stratification is dry neutral or saturated neutral, respectively. Dry neutral stratification is also characterized by a constant potential and decreasing equivalent potential temperature with height. In saturated neutral conditions, the potential temperature increases with height, and the equivalent potential temperature stays constant (Kraus, 2004; Trapp, 2013).

If whole layers are lifted, as could be the case in frontal zones, the stability of the air layer can change. As is visible from Fig. 2.1, the vertical temperature gradient can be changed during lifting. If the lower end of the layer ( $A$ ) is more humid than the higher end ( $B$ ), saturation and cooling with moist adiabatic temperature gradient occurs earlier below. The upper part of the layer is cooled stronger, which leads to a destabilization of the layer (Fig. 2.1(a)). This is known as potential instability. If the upper part is moister and saturation takes place earlier, the layer  $AB$  becomes stabilized through the lifting. This is called potential stability. As is visualized in Fig. 2.1(b), even an inversion would be possible after lifting (Iribarne and Cho, 1980).

For all considerations of stability, simplifications are made. In reality, the environment is disturbed by the uplift of the air parcel. To balance this upward motion, the air in the environment slowly sinks down for continuity reasons. As a consequence, the environment is slightly heated, reducing the instability. In addition, entrainment of environmental air into the parcel is neglected. This process also reduces the

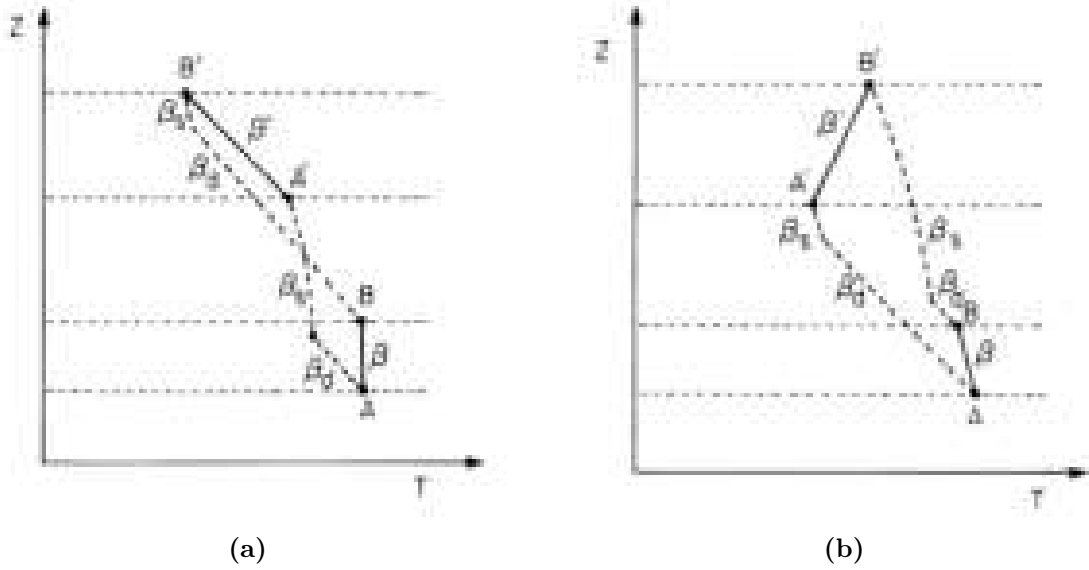


**Figure 2.1:** (a) Destabilization of an air layer in potential instability and (b) stabilization of an air layer in potential stability.  $\beta_s$  herein indicates the moist adiabatic lapse rate  $\Gamma_m$  and  $\beta_d$  the dry adiabatic lapse rate  $\Gamma_d$ .  $A$ ,  $B$  and  $\beta$  show the air layer profile before lifting,  $A'$ ,  $B'$  and  $\beta'$  afterwards. Figure from Iribarne and Cho, 1980.

temperature difference between the environment and the lifted parcel and therefore the instability (Kraus, 2004).

### 2.1.4 Convective measures

Several measures connected with convection are used in meteorology which represent the stratification. One of these measures is the convective available potential energy (CAPE). As the name implies, CAPE expresses how much potential energy is available in a vertical column to be converted into vertical motion after the triggering of convection. According to Trapp (2013), it is computed as the vertical integral from LFC to EL over the buoyancy  $B$ :

$$\text{CAPE} = \int_{z_{\text{LFC}}}^{z_{\text{EL}}} B dz. \quad (2.12)$$

Large CAPE indicates a high potential for deep convection. However, as high values of this measure are a necessary, though not sufficient condition for convection, there is no guarantee that convection actually will be triggered. Therefore, the convective inhibition (CIN) plays a role. It is computed in a similar way as CAPE but integrated from the surface to the LFC:

$$\text{CIN} = \int_{z_{\text{sfc}}}^{z_{\text{LFC}}} B dz. \quad (2.13)$$

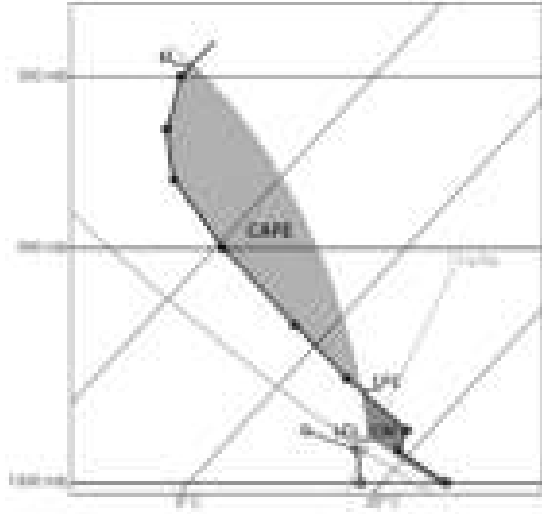


**Figure 2.2:** Thermodynamic diagram (skew  $T - \ln p$ ) with an exemplary sounding (black line) showing a negative area for CIN (blue) between surface and LFC and a positive one for CAPE (orange) between LFC and EL. Figure from Trapp (2013).

Large values of CIN can prevent the development of convection even if the CAPE is sufficient. Low values are favorable for the consumption of CAPE and its conversion in vertical motion (Trapp, 2013). In the case of free convection, CIN equals  $0 \text{ J kg}^{-1}$ . Via conservation of energy the two velocities  $w_{\text{CIN}}$  and  $w_{\text{max}}$  can be calculated:

$$w_{\text{CIN}} = \sqrt{2\text{CIN}} \quad \text{and} \quad w_{\text{max}} = \sqrt{2\text{CAPE}}. \quad (2.14)$$

Here,  $w_{\text{CIN}}$  is the vertical velocity a parcel must exceed in the boundary layer to overcome the CIN barrier and reach the LFC. For further uplift of the parcel,  $w_{\text{max}}$  describes the possible maximum vertical velocity. This value is usually too high due to limitations in the parcel theory described at the end of section 2.1.3 (Markowski and Richardson, 2010).

The CAPE and CIN can also be visualized with a thermodynamic diagram (Fig. 2.2). CAPE is the orange-shaded area between LFC and EL, and CIN is the blue-shaded area below. It is visible that CAPE would increase if cold air is advected in higher layers, leading to a shift of the temperature line to the left. Warmer and moister air near the surface would also lead to a larger CAPE as a consequence of a lower LFC. CIN is reduced for these conditions and increased for a lower temperature at the ground and an inversion above. After equivalent potential temperature  $\theta_e$  is a measure combining humidity and temperature, there is a linear correlation between CAPE and low-level  $\theta_e$  confirmed in a study by Kohler et al. (2010), starting for values around  $\theta_e = 344 \text{ K}$  (Fig. 2.3).

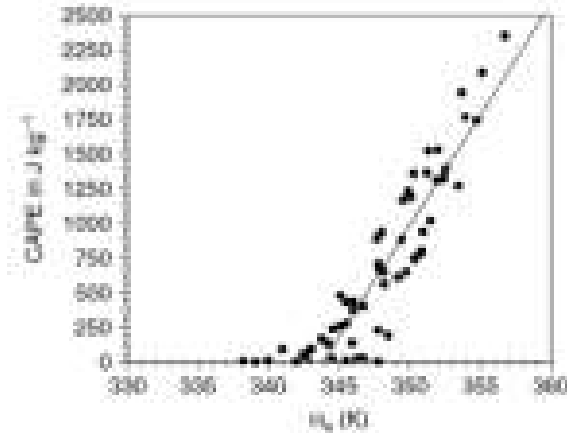


**Figure 2.3:** Linear correlation between equivalent potential temperature  $\theta_e$  and CAPE. Values for  $\theta_e$  are averaged over the lower part of the boundary layer (25 hPa). Figure from Kohler et al. (2010).



**Figure 2.4:** Single cells, multicells and supercells dependent on the vertical wind shear. Figure from Markowski and Richardson (2010).

Besides the energy measures CAPE and CIN, the vertical wind shear is also important in the context of deep convection as it is responsible for the organization of convection. Usually, the wind shear is calculated as the difference between the wind vectors in 6 km and near the surface and is referred to as deep-layer shear (DLS), even though it is actually a velocity difference and no shear. High values of DLS tend to support the organization of convection and lead to a longer lifetime of convective cells. However, too strong wind shear can also be obstructive for the convection as it can dissolve weak updrafts or prevent the initiation by larger entrainment (Markowski and Richardson, 2010).

### 2.1.5 Convective cells

As mentioned above, vertical wind shear mainly influences the organization of convection and therefore the type of convective cell. From Fig. 2.4, it becomes visible that single cells usually develop in weak shear environments, multicells in medium shear environments and supercells in strong shear environments. Some overlap occurs due to secondary factors like the vertical distribution of buoyancy or moisture (Markowski and Richardson, 2010).

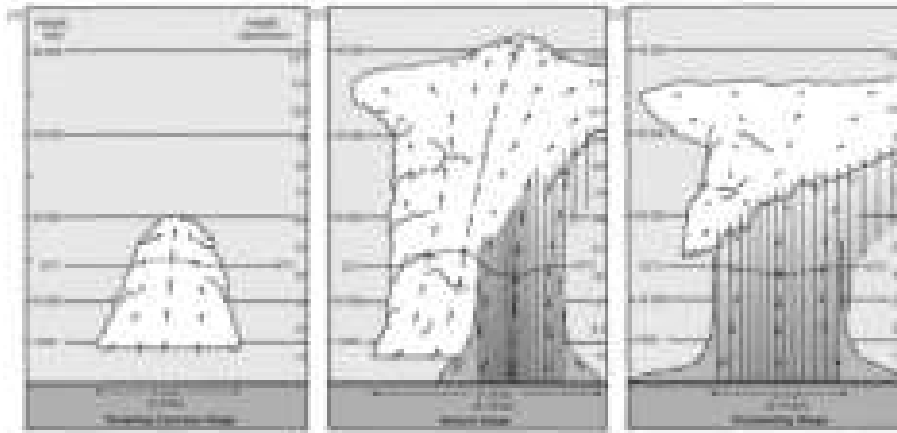


**Figure 2.5:** (a) Towering cumulus stage, (b) mature stage and (c) dissipating stage of a single cell during its lifetime. Figure from Markowski and Richardson (2010), based on Byers and Braham (1948) and Doswell (1985).

### Single cells

The single cells within a weak vertical wind shear environment are characterized by one updraft and no subsequent organized convection. Severe weather like hail or severe wind gusts is rare for a single cell during its short lifetime of roughly 30–60 min. During the lifetime, a single cell goes through three characteristic stages shown in Fig. 2.5: the first stage is the towering cumulus stage, where only the cell's updraft exists. It is most of the time initiated by the diurnal cycle of the boundary layer, where the maximum heating during daytime increases CAPE and reduces CIN. After the initiation of the updraft, precipitation particles large enough to fall through the convective updraft are formed within the mature stage. Because the hydrometeors fall and partly evaporate, a downdraft is induced, which co-exists close to the updraft. The downdraft hits the ground with a relatively low temperature, flows out horizontally to the sides (cold pool) and initiates the gust front at the leading edge. Due to the small vertical wind shear, the gust front is usually too weak to initiate new cells. In the dissipating stage, the cold pool cuts off the updraft from potentially buoyant air from the ground. This leads to a weakening of the updraft. The downdraft completely dominates and the cell dissipates (Markowski and Richardson, 2010; Doswell, 1985).

### Multicells

As could be seen from Fig. 2.4, multicells occur in an environment of moderate vertical wind shear. The gust front becomes asymmetrical and is able to initiate new cells repeatedly, mainly on the downshear flank (Fig. 2.6). The wind shear

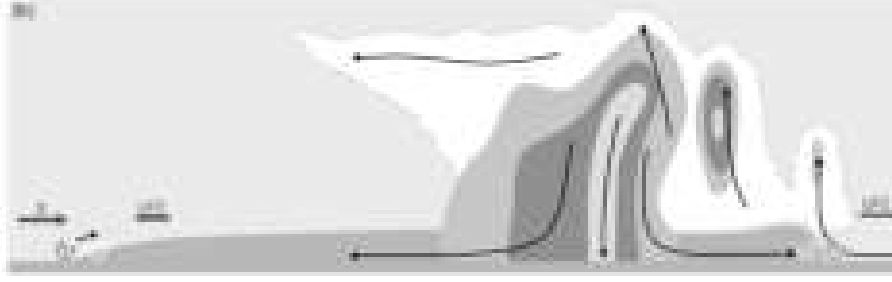


**Figure 2.6:** Lifting by the gust front for a multicell in moderate westerly wind shear. Green and yellow areas indicate areas of precipitation, the darker blue area the cold pool. With the black arrows some storm-relative streamlines are indicated and the LFC is depicted. The white circular arrows show in which sense the cold pools induce horizontal vorticity, and the purple ones how the wind shear affects the vorticity. Figure from Markowski and Richardson (2010).

induces an anticyclonic<sup>1</sup> horizontal vorticity. On the downshear flank of the cells, the cold outflow of the cells produces cyclonic horizontal vorticity, which can add up with the anticyclonic one from the wind shear along the gust front. Lifting of air parcels from the ground up to the LFC and the development of new cells, mainly on the downshear flank, are the consequences. Thus, a multicell consists of several ordinary cells in different stages of their life cycle. The movement of the system is then determined by the advection of the cells with the mean wind and a propagation component due to the lifting along the gust front. Multicells live longer and severe weather is more likely than in single cells, which increases the risk of damage along their path (Markowski and Richardson, 2010).

## Supercells

Supercells are the rarest storm type, but as they are connected with strong updrafts with high vertical velocities, severe weather like large hail or heavy precipitation can be formed. As a consequence, supercells produce large damage like in the case of the events at the end of July 2013 and June 2021 mentioned in the introduction, or like in the case of the Munich hailstorm in June 2019, which was responsible alone for a loss of almost EUR 1 billion (Munich Re, 2020, Wilhelm et al., 2020). As mentioned above, supercells form in an environment of strong vertical wind shear, therefore, a lot of horizontal vorticity is available. From the linearized vorticity equation of the vertical component  $\zeta$

$$\left(\frac{\partial \zeta'}{\partial t}\right)_{\text{sr}} = \underbrace{-(\vec{v} - \vec{c}) \cdot \nabla_{\text{h}} \zeta'}_{\text{advection}} + \underbrace{\vec{S} \times \nabla_{\text{h}} w' \cdot \hat{k}}_{\text{tilting}}, \quad (2.15)$$

<sup>1</sup>In the present work, cyclonic and anticyclonic are defined as on the northern hemisphere, which means that cyclonic describes a counterclockwise and anticyclonic a clockwise rotation.

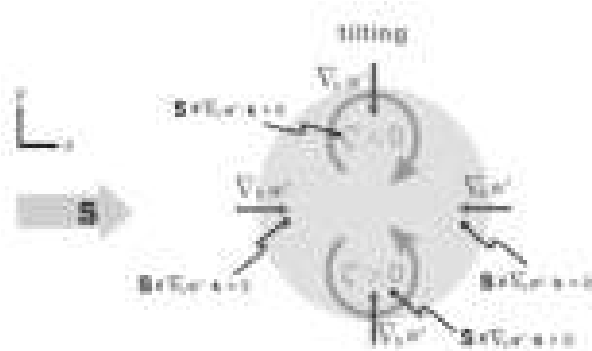


**Figure 2.7:** Vortex pair in the updraft of the supercell after tilting horizontal in vertical vorticity. Figure from Markowski and Richardson (2010).

with the storm-relative wind ( $\vec{v} - \vec{c}$ ) and the shear vector  $\vec{S}$ , it follows that the horizontal vorticity can be tilted into vertical vorticity. A vortex pair with an anticyclonic rotation on the left side and a cyclonic rotation on the right side of the updraft is generated (Fig. 2.7). For an environment with directional shear and therefore streamwise vorticity<sup>2</sup>, the cyclonic vortex is advected into the center of the updraft, and the anticyclonic vortex is shifted into the downdraft region and dissipates. This way, deep and persistent rotation within the updraft region, which is called a mesocyclone, can be generated. This mesocyclone is the defining criterion for supercells. It is usually 3–8 km wide and has a rotation of  $10^{-2} \text{ s}^{-1}$ . For the time an air parcel rises through the entire updraft, the mesocyclone should persist ( $\approx 20 \text{ min}$ ) (Markowski and Richardson, 2010).

As well as in the other storm types, precipitation particles form within the updraft and rise high into the atmosphere. In supercells, the strong storm-relative winds in middle and high levels lead to transport of the hydrometeors and therefore a spatial displacement of the updraft and the forming downdrafts (Fig. 2.8). The downdrafts are especially located forward and rearward from the updraft (Trapp, 2013). The spatial displacement of updrafts and downdrafts enables a longer lifetime of a supercell compared to ordinary cells (1–4 h common, even longer is possible) (Markowski and Richardson, 2010).

During their lifetime, supercells are subject to nonlinear and linear pressure perturbations. The nonlinear pressure perturbations lead to an upward directed pressure gradient force within each of the vortices at the side of the updraft that were shown in Fig. 2.7. The updraft splits into two cells, right and left of the original updraft. The new cells are called right-mover and left-mover, which refers to the position

---

<sup>2</sup>Streamwise vorticity means that the storm-relative wind points in the same direction as the vorticity gradient. In contrast, crosswise vorticity indicates that storm-relative wind and vorticity gradient are perpendicular.

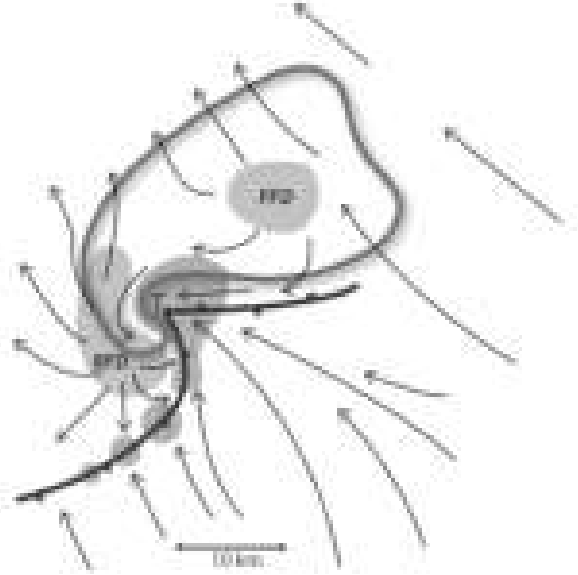


**Figure 2.8:** Plan-view schematic of a supercell at low levels. Arrows indicate streamlines, red shading regions the updraft and blue shading regions the downdrafts, which are named as forward-flank downdraft (FFD) and rear-flank downdraft (RFD). Figure from Trapp (2013), adapted from Lemon and Doswell (1979).

relative to the vector of the vertical wind shear. Precipitation can support the splitting, which, however, is not a necessary requirement. The splitting can take place several times as long as there is enough crosswise vorticity. The linear pressure perturbations lead to high pressure upshear and low pressure downshear. If the shear vector veers with height like in the situation of a clockwise hodograph, this induces an upward-directed pressure gradient force on the right side of the updraft and a downward force on the left side. The right-mover would strengthen, and the left-mover weaken in that situation. It is the other way round for a counterclockwise hodograph (Markowski and Richardson, 2010).

Thus, supercells not only have an advective component from the mean wind but also a propagation to the right for right-movers or to the left for left-movers. A widely used parameterization for the motion of supercells

$$\vec{v}_{\text{rm}} = \vec{v}_{\text{m}} + D \left[ \frac{\vec{v}_{\text{s}} \times \hat{k}}{|\vec{v}_{\text{s}}|} \right] \quad \vec{v}_{\text{lm}} = \vec{v}_{\text{m}} - D \left[ \frac{\vec{v}_{\text{s}} \times \hat{k}}{|\vec{v}_{\text{s}}|} \right] \quad (2.16)$$

was set up by Bunkers et al. (2000), where the first summand  $\vec{v}_{\text{m}}$  represents the advection by the mean wind of the lowest 6 km, and the second one the deviation perpendicular to the right (left) of the shear vector  $\vec{v}_{\text{s}}$ , computed with a mean wind between 5.5 and 6 km as upper tail and between 0.5 and 0 km as lower tail. Bunkers et al. (2000) showed that  $D = 7.5 \text{ m s}^{-1}$  works best to represent the deviation from the mean wind for a dataset of supercells over the United States. However, Tonn

et al. (2023) found that the deviation from the mean wind is smaller for supercells over Germany and  $D = 4.0 \text{ m s}^{-1}$  works best.

### Mesoscale convective systems

A mesoscale convective system (MCS) is an ensemble of several thunderstorm cells. This ensemble extends over a large area with contiguous precipitation (100 km or more in at least one direction) so that the Coriolis acceleration becomes significant (Markowski and Richardson, 2010). According to Trapp (2013), they have a much longer lifetime than the isolated cells of often nine hours up to one day. One subset of MCS is the mesoscale convective cluster (MCC), which is defined over several conditions for its cloud anvil (Maddox, 1980). Another form of MCS is the squall line with a large extent in only one direction. The squall line is usually characterized by the arrangement of the convective cells along a line in the front part and a large area behind with stratiform precipitation.

## 2.2 Aerosol–cloud interactions

For all convection types described above, microphysical processes take place, which are responsible for the formation of clouds and rain. In the following, the focus is on these processes to create an understanding of how cloud droplets form using aerosols and how they become precipitation particles. Afterwards, some general ACI are presented. At the end of the chapter, the focus is on convective clouds and how they are affected by aerosols.

### 2.2.1 Formation of cloud droplets

Cloud droplets are formed via nucleation, which is the process where a liquid or solid phase of water is initiated from water vapor. A solid ice phase in cold clouds can form from the gas phase either directly via deposition or via the freezing of previously created liquid droplets. Even if convective clouds spread vertically far, and thus the ice phase also plays a role, the focus in this section is on the processes in warm clouds where liquid droplets are formed. There is homogeneous nucleation where the condensed phase directly forms from the vapor. In this case, the atmosphere has to be extremely supersaturated. The vapor saturation ratio  $S = e/e_s$  with the water partial pressure  $e$  and the equilibrium vapor pressure  $e_s$  has to exceed values of four, which is unrealistic high for atmospheric clouds (Lamb and Verlinde, 2011).

In heterogeneous nucleation, some aerosols in the atmosphere facilitate the formation of the condensed phase by lowering the free energy of germ formation. These aerosols are termed cloud condensation nuclei (CCNs) or ice nucleating particles (INPs) if

ice particles are formed directly from the vapor. In the atmosphere, there are very different aerosols in different sizes, shapes, compositions, concentrations, etc., also dependent on the location of the earth. There are insoluble aerosol particles that can serve as CCNs. The heterogeneous nucleation is then a function of the contact angle with the aerosol’s surface and the size of the particle. Large particles with small contact angles serve as better CCNs (Lamb and Verlinde, 2011).

Much more effective is the formation of a liquid droplet with a water-soluble aerosol particle. This procedure starts with the deliquescence how the dissolving of a solid particle into a liquid solution is called. As the entropy increases during the process, the deliquescence is actually not a nucleation but an equilibrium transformation. At the deliquescence point, which is below 100% relative humidity but different for the different soluble substances in the atmosphere, dissolution takes place. A further increase of humidity beyond the deliquescence point leads to further growth of the solution particle (Lamb and Verlinde, 2011).

For the formation of a cloud droplet from the solution droplet, the so called activation is necessary. For the activation, a critical supersaturation must be reached. The supersaturation ( $S_K - 1$ ) can be calculated via the Köhler saturation ratio

$$S_K - 1 = \frac{A}{r_d} - \frac{BiN_s}{r_d^3} \quad (2.17)$$

with the droplet radius of the solution  $r_d$ , the slightly temperature dependent parameters  $A$  and  $B$ , the van’t Hoff factor  $i$  and  $N_s$  expressing the solute content. The first summand on the right-hand side of equation 2.17 represents the curvature effect of the droplets, showing that the saturation ratio is increased in comparison to a flat surface especially for small droplets. The second summand is the solution effect lowering the saturation ratio. In combination, these two terms result in the Köhler curve shown in Fig. 2.9 where for small radii the solution effect dominates until the supersaturation is high enough to reach the critical radius  $r_c$ . Above this size, no further supersaturation is necessary for further growth (Lamb and Verlinde, 2011).

The larger  $N_s$  of a solution is, the lower the required supersaturation is due to a stronger solution effect. As the solute content is proportional to the size of the diluted aerosols, for larger aerosols, a lower supersaturation is needed for the activation. Therefore, only the larger aerosols become activated as CCNs. The actual activation size that separates not-activated aerosols from CCNs depends on the actual conditions in a cloud, but as the maximum supersaturations in atmospheric clouds are below 10%, particles smaller than about  $0.01 \mu\text{m}$  cannot become CCNs (Lamb and Verlinde, 2011).

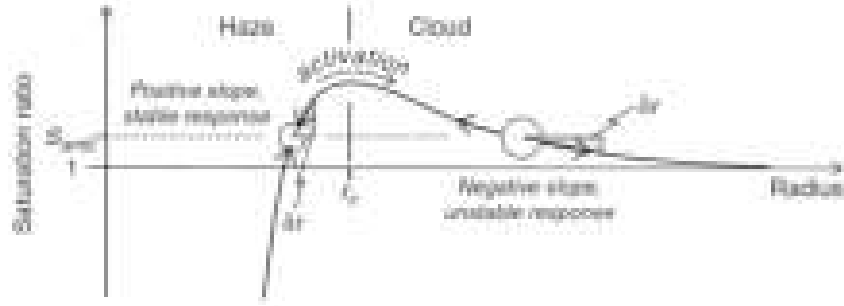


**Figure 2.9:** Schematic illustration of the Köhler function in equation 2.17. Figure from Lamb and Verlinde (2011).

### 2.2.2 Formation of raindrops

Once a cloud droplet is formed, it can grow by condensation of water vapor. From the growth rate in Lamb and Verlinde (2011), the following proportionality can be seen for the condensational droplet growth:

$$\frac{dr_d}{dt} \sim r_d^{-1}. \quad (2.18)$$

The smaller the droplets are, the faster the growth is. For droplets in the order of  $20 \mu\text{m}$ , the condensational growth becomes very small and inefficient in forming raindrops of typical diameters in excess of a millimeter. Therefore, collection must take place by which relatively large droplets collide and coalesce with each other. To get collisions of droplets in a cloud, significant relative motions between the droplets are necessary. First, similar-sized droplets can collide in a stochastic collection process through turbulence. For this turbulent physical process, the model used in this work employs a parameterization referred to as autoconversion. Afterwards, a few larger droplets exist among many smaller cloud droplets. Due to the different masses, different gravitational speeds occur for the larger and smaller droplets. The continuous collection, which is also called accretion, takes place where the large droplets collect many of the small droplets within their pathway. This droplet growth is efficient in forming raindrops as the increase of the droplet radius is exponential with time (Lamb and Verlinde, 2011).

If the ice phase coexists within a cloud, the droplet growth can take place via deposition or riming. The depositional growth of ice crystals is analogous to the condensational growth of liquid droplets and therefore more relevant for the small ice crystals. It occurs, for example, in the Wegener-Bergeron-Findeisen process, where a gas-phase diffusion transfers water vapor from an evaporating droplet to a growing ice crystal in a very specific range of supersaturation. After reaching a

critical size, the ice crystals grow via riming, in which analogously to the collision–coalescence for liquid droplets, the falling ice crystals collect many small supercooled cloud droplets. There is the possibility for the ice crystals to grow to graupel or even hail and remain in the solid state as they continue falling, or to return to the liquid state as ambient conditions change (Lamb and Verlinde, 2011).

### 2.2.3 Albedo and lifetime effect

The actual microphysics and macrophysics of a cloud can highly differ dependent on the aerosol concentrations. There are regions with less aerosols, like over the sea and regions with more aerosols, like urban areas over land. In polluted areas, more CCNs can be activated, leading to more but smaller cloud droplets than in cleaner conditions. These differences have an impact on the earth’s radiant energy balance as the size of the droplets determines the optical thickness  $\tau$ . From Twomey (1977),

$$\tau \sim r_d^{-1} \quad (2.19)$$

with the droplet diameter  $r_d$  follows, meaning that the optical thickness is larger in clouds with smaller droplets. As albedo and cloud optical thickness are connected, more radiation is reflected by the clouds in case of polluted conditions and less in clean conditions. This is referred to as the albedo or Twomey effect (Twomey, 1974; Lamb and Verlinde, 2011).

Besides the albedo, aerosol concentrations also determine the lifetime of a cloud. As there are bigger cloud droplets in clean conditions, the coalescence is more active than in polluted conditions where the coalescence is inhibited. Therefore, efficient rain can occur in clean conditions. Afterwards, a lot of the cloud water is removed, and the remaining part of the cloud can evaporate in relatively dry air. The cloud dissolves. In contrast, the air stays relatively moist in polluted conditions as only little rain may occur. Therefore, the cloud persists for a longer time, which is referred to as the lifetime effect (Lamb and Verlinde, 2011).

### 2.2.4 Aerosol–cloud interactions in convective clouds

How aerosols affect convective clouds is of special interest for the present work. Rosenfeld et al. (2008) states the theory of cold-phase convective invigoration, which is visualized in Fig. 2.10. In the case of clean conditions, less but larger cloud droplets exist, which can grow as a consequence of coalescence. Therefore, rain falls out before reaching the 0°C isotherm. In contrast, this is not possible for the smaller droplets in polluted conditions. The droplets reach higher atmospheric layers, where they freeze onto ice precipitation that falls and melts in lower layers. The freezing above

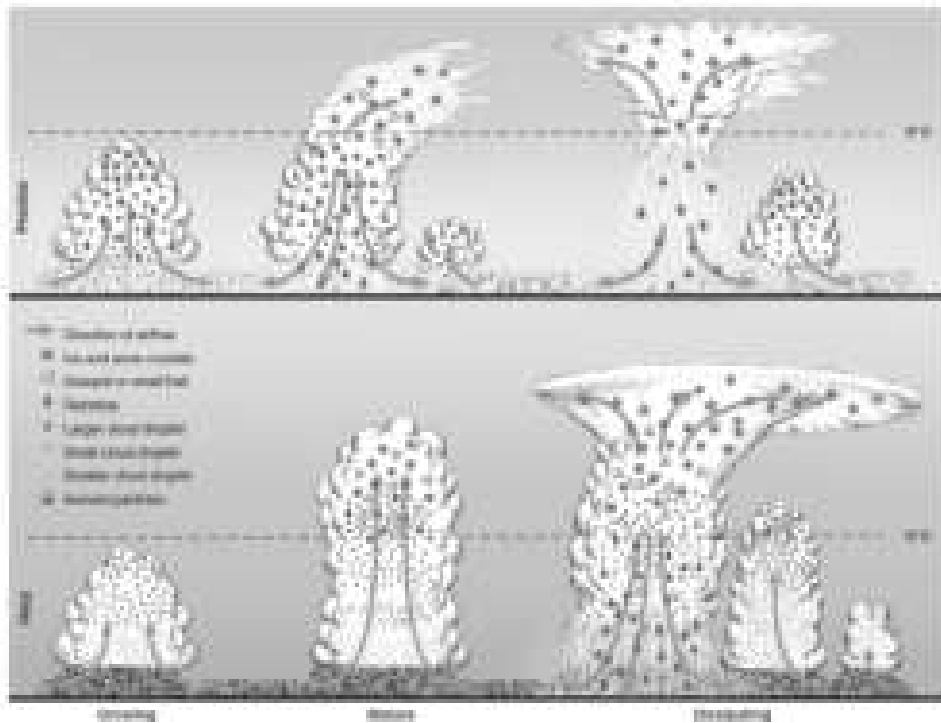


**Figure 2.10:** Evolution of a deep convective cell with its hydrometeors in pristine (top panel) and polluted conditions (bottom panel). Figure from Rosenfeld et al. (2008).

is connected with energy release and the melting below with energy consumption. This leads to an enhanced upward energy transport in polluted conditions. In this theory, the larger consumption of CAPE leads to a greater amount of released kinetic energy that could invigorate the convection and lead to greater overturning and more precipitation. However, there is also the radiative aerosol effect influencing the convection: more pollution means higher albedo and more absorbed radiation by the aerosols in the atmosphere resulting in a more stable atmosphere and less energy at the surface for the initiation of convection. Therefore, Rosenfeld et al. (2008) showed a maximum in convective invigoration for moderate CCN concentrations ( $1200 \text{ CCNs cm}^{-3}$  for supersaturations of 0.4%). For more CCNs the energy release is again lower.

Besides this theory by Rosenfeld et al. (2008), there is also the theory of warm-phase convective invigoration. The theory states that in environments with higher pollution, a greater net surface area is available for condensation. Therefore, the latent heat release by condensation is increased leading to stronger convection (Cotton and Walko, 2021). However, there are recent studies that can not confirm this theory (e.g., Öktem et al., 2023). Another theory posits that more CCNs can increase the humidity of the environment as a consequence of stronger moisture detrainment. This leads to a higher temperature and therefore large-scale ascent and stronger

convection (Abbott and Cronin, 2021). Independent of the physical process leading to a convection invigoration, several studies in the past years were not able to provide evidence for the invigoration hypothesis as certain environmental conditions can lead to differences between the real cloud and the idealized invigoration scenario (Altaratz et al., 2014).

In reality, there are many more atmospheric parameters that influence the aerosol effects on clouds. Relative humidity, vertical wind shear and CAPE mainly determine the aerosol impact on convection intensity and precipitation (Fan et al., 2016). A dominant role of vertical wind shear was found by Fan et al. (2009) where the aerosol effects for isolated deep convective clouds were assessed systematically with idealized cloud-resolving model simulations. For strong wind shear, increasing CCN concentration reduces the amount of convective precipitation systematically. For weak wind shear, the effect is as stated in Rosenfeld et al. (2008), with an invigoration up to an optimum CCN concentration and a decrease for even more CCNs. Also the influence of humidity was seen in Fan et al. (2009) with a stronger decreasing rate of convective strength in humid air.

In other studies, simulations of real weather events were classified by their synoptic situations (e.g., Barthlott and Hoose, 2018; Barthlott et al., 2022b). In Barthlott et al. (2022b), also a decrease of convective precipitation for increasing aerosol loading was shown. For the cases with weak synoptic-scale forcing, the response of convective precipitation was stronger than for the strongly forced cases. In Barthlott and Hoose (2018), the response was also stronger for the weakly forced cases, even if it was not as systematic as the decrease for the strongly forced cases.

Thus, there are studies that do not necessarily support the theory of convective invigoration or identify specific conditions under which increasing CCN concentrations negatively affect precipitation. Especially the study by Fan et al. (2009) mentioned above is of great interest for the present work as a strong impact of the vertical wind shear on the convection was elaborated. Therefore, this work is intended to give new and generally valid statements about the impact of the wind shear by using real-case simulations.



## 3. Data basis and processing

This chapter lists which model simulations and observation data are used in the present thesis. First, an overview of the Swabian MOSES campaign is given because two days of this field campaign are simulated in the present work. The grid used for the real case simulations is described afterwards, and what parameters of the simulations are modified to study the impact of the wind shear on ACI and convective precipitation. Also sounding and radar data used to compare the model output with observations are presented in this chapter.

### 3.1 Swabian MOSES 2021 field campaign

Swabian MOSES was a field campaign coordinated by the Karlsruhe Institute of Technology (KIT) and conducted by five Helmholtz research centers, three universities and the German Weather Service (DWD) (Kunz et al., 2022). It took place between May and September 2021. The measuring area was southwestern Germany, including the Neckar Valley and Swabian Jura (red dashed box in Fig. 3.1). In this area, highly flexible and mobile observation modules like the KITcube (Kalthoff et al., 2013) or radio soundings were used to study hydro-meteorological extremes. The extremes include large-scale heat waves with associated droughts that are not part of the present work but also local-scale thunderstorms with associated hail and heavy precipitation. These hydro-meteorological extreme events occur more often in the measuring area and cause tens of millions of euros in damage per year (Kunz et al., 2022), which is why this area was chosen. The research goal of the field campaign was to capture and explore the whole event chain of an extreme. For a convective cell, this means to cover the whole life cycle of the cell, including the first initiation, the further development with associated impacts like hail development, including also consideration of possible damage, and the dissipation of the cell (The ATMO Hub of KIT, 2023). In the summer of 2023, a follow-up campaign with a modified measurement strategy took place.

### 3.2 ICON simulations

To study the impact of wind shear on ACI and convective precipitation, three days with convective activity were chosen for which simulations with the ICOsahedral Non-hydrostatic (ICON) model were done. As mentioned above, two of the days, 23 June 2021 and 28 June 2021, are days from the Swabian MOSES campaign. The third simulation day, 22 July 2015, was found in the data set of Tonn et al. (2023) as a day with strong convective activity, even with supercells over Germany. In

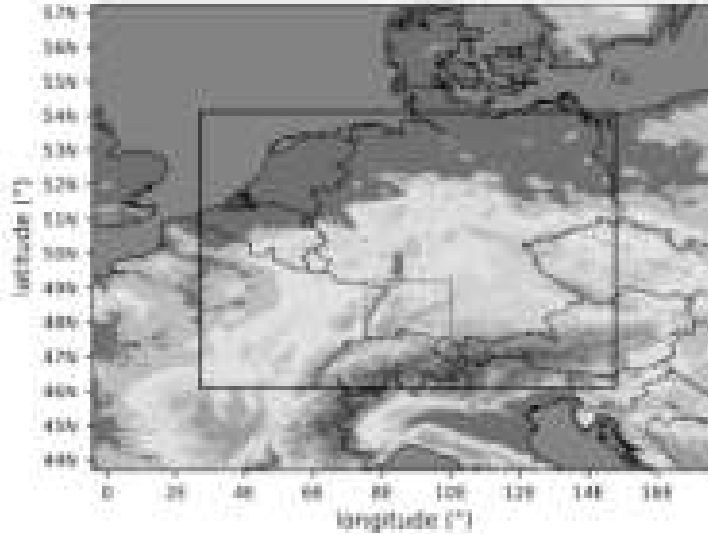


**Figure 3.1:** Map of the ICON-D2 model area. Black framed domain inside indicates the model area for the simulations performed for the present study. The red dashed box shows the location of the Swabian MOSES field campaign.

all simulation days, there is a diurnal cycle of the convection developing within the simulation area, which makes the days suitable for this work.

The ICON model is the global and regional NWP model at DWD, which replaced the former operational global model GME in January 2015. There is the capability to run global simulations with so called nests, domains of special interest where the resolution is increased inside. This is done for the operational ICON over Europe (ICON-EU) since June 2015, which replaced the former model COSMO-EU (Consortium for Small-scale Modeling). The special feature of the ICON model is that the horizontal grid is constructed from an icosahedron projected onto a sphere. The grid consists of 20 equilateral spherical triangles that span the whole sphere. An ICON grid ( $\mathbf{RnBk}$ ) with a special resolution is created from these 20 triangles by an initial root division of the edges into  $n$  equal sections followed by  $k$  bisection steps. A set of vertical layers with height-based vertical coordinates is used as a vertical grid. All of the vertical layers have the same horizontal triangular grid structure. From that, the ICON 3D-grid results. The vertical layers are terrain following in the lower atmosphere. In higher layers, the terrain signal is smoothed out. As the ICON model utilizes the smooth level vertical (SLEVE) coordinate (Leuenberger et al., 2010), a faster transition to a smoothed signal in the upper troposphere is possible. As a regional model, the convection-permitting ICON-D2 model (R19B07) is used operationally with a horizontal resolution of 2 km by DWD. This model replaced the former COSMO-D2 model, which was used until February 2021 (Reinert et al., 2023).

**Table 3.1:** Parameterizations in the ICON model used in the present thesis.

Model aspect	Setting
Heterogeneous ice nucleation	Based on mineral dust concentrations (Hande et al., 2015)
Homogeneous ice nucleation	Physically based cirrus nucleation scheme (Kärcher and Lohmann, 2002; Kärcher et al., 2006)
Convection parameterization	Shallow and deep convection: explicitly resolved
Land-surface model	Multi-layer land surface scheme TERRA (Heise et al., 2006)
Turbulence scheme	Scheme based on prognostic equation for turbulent kinetic energy (Raschendorfer, 2001)
Radiation scheme	Rapid radiative transfer model (Mlawer et al., 1997)

In the present work, a regional model extending over the black framed area within the ICON-D2 domain visualized in Fig. 3.1 is used for the simulations. The used model has a horizontal resolution of 1 km (R19B08) and covers nearly whole Germany as well as some bordering regions. 101 half levels extending from the surface up to 22 km above ground level, in intervals that increase with altitude, are used in the vertical. The half levels are the boundaries of the vertical layers, and the vertical velocities and the turbulent kinetic energy are defined at these levels. All other prognostic variables are defined at the 100 full levels, which are the centers of the layers.

The model simulations are initialized at 0 UTC, and the model output is generated half-hourly for an integration time of 24 hours. A two-time-level predictor-corrector scheme, explicit except for the terms that describe the vertical sound-wave propagation, is used for the time integration (Zängl et al., 2015). For 23 June 2021 and 28 June 2021, ICON-EU operational analysis (R03B08) with a horizontal resolution of 6.5 km are used as initial and boundary data, which are mapped on the regional 1-km limited-area grid. For the third simulation day, 22 July 2015, the initial and boundary data are from the Integrated Forecasting System (IFS) of the European Center for Medium-Range Weather Forecasts (ECMWF) because an index to describe the soil moisture was implemented only in 2018 in the ICON data. As well as on the other days, the data are mapped on the R19B08 ICON grid to have analogous simulations for the three days.

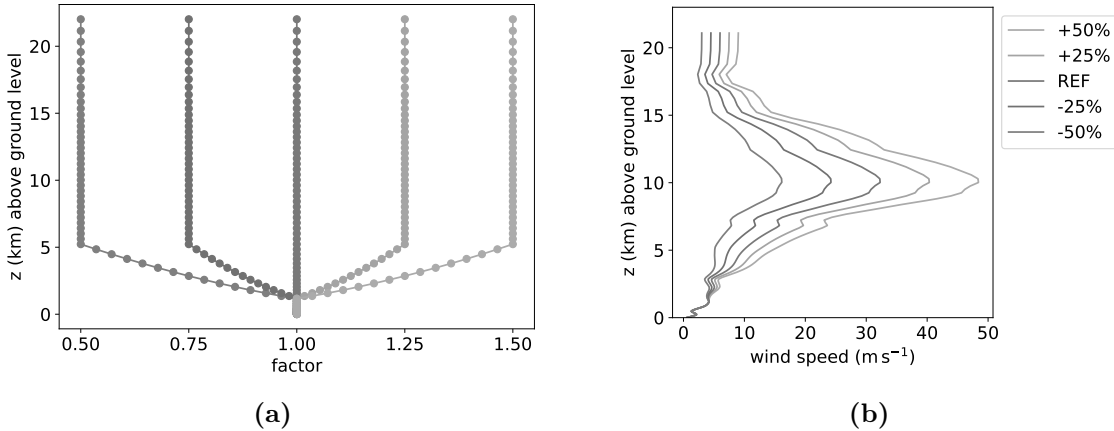


**Figure 3.2:** (a) Factors that are multiplied with the wind speed of the initial and boundary data in the corresponding height to change the vertical wind shear of the simulations on 23 June 2021 and 28 June 2021. For the IFS data on 22 July 2015, the level heights are slightly different. (b) Resulting vertical profile of horizontal wind speed in the model simulations with continental CCN concentration at the grid point closest to the Swabian MOSES sounding location in Stuttgart at 23 June 2021, 0 UTC.

Aerosol effects on the microphysics of mixed-phase clouds are considered in the model simulations via the two-moment bulk microphysics scheme of Seifert and Beheng (2006). This scheme predicts the mass and number concentrations of the liquid hydrometeors cloud droplets and raindrops as well as of the solid hydrometeors cloud ice, snow, graupel and hail. With that scheme, it is possible to create four reference simulations (in the following also sometimes named REF in the figures) per day with a different CCN concentration  $N_{\text{CCN}}$  in each run by using the CCN activation of Segal and Khain (2006). The simulations are performed with maritime ( $N_{\text{CCN}} = 100 \text{ cm}^{-3}$ ), intermediate ( $N_{\text{CCN}} = 250 \text{ cm}^{-3}$ ), continental ( $N_{\text{CCN}} = 1700 \text{ cm}^{-3}$ ) and continental polluted conditions ( $N_{\text{CCN}} = 3200 \text{ cm}^{-3}$ ). Further physics parameterizations of the model underlying the simulations shown in the present thesis can be looked up in Table 3.1.

After generating the reference simulations, the wind shear is changed in the initial data in order to consider the effect of the wind shear on ACI and convective precipitation before repeating the four runs for the different CCN concentrations. However, the wind shear can be changed in several ways and magnitudes. It was decided to multiply only the wind speed of the initial data with a factor changing with height (Fig. 3.2a). The direction of the wind is the same in the initial data of all simulations.

For the ICON-EU initial data, the wind speed in the lowest 1.15 km (IFS: 1.092 km) above ground level is kept constant. Above, the factor is increased (decreased) linearly with height up (down) to a constant factor used in a height of 5.23 km (IFS:

5.18 km) and above. Although the boundary layer height varies and can also be higher than 1.15 km, the setup described above is chosen to get no strong disturbances of the boundary layer but also a relevant wind shear difference for the storm inflow layer (1–3 km commonly assumed according to Markowski and Richardson (2010)). The layer with the linear increased (decreased) factor is important to have not an abrupt rise (fall) of the wind speed above the boundary layer. On the other side, it is important to choose the upper end of this layer not too high to have already large (small) factors in lower atmospheric layers, which are responsible for the storm organization and not only in the upper troposphere.

As can be seen from Fig. 3.2a, four different shear cases are considered apart from the reference simulation, two of them with a decreased and two with an increased vertical wind shear. The wind speed above 5.23 km is increased and reduced by 25% and 50% according to which the simulations are named in the following. The different cases cover a wide range of different vertical wind shear as can be seen for one grid point near Stuttgart on 23 June 2021, 0 UTC in Fig. 3.2b. The modification of the vertical wind shear in the way described above leads to differences in the DLS, which makes organized convection favorable at some grid points in the simulations with increased shear, while it is not the case for the same grid points in the simulations with decreased shear. An even stronger increase and decrease than 50% would lead to even larger upper tropospheric differences in the different simulations. As they are already large for the performed simulations (Fig. 3.2b), no further increase and decrease of the initial wind speed profile is done.

Even if the wind direction is not changed in the initial data, the horizontal wind in the vertical layers can vary in the simulations with different shear. This is due to the fact that the wind field is connected with the pressure field. After changing the wind speed in the free atmosphere, the pressure field initially adjusts. A higher wind speed is connected with a larger pressure gradient (Fig. 3.3a). As the pressure is also related to the temperature, all variables that influence the thermodynamics in the simulations can lead to some changes in the pressure field, which then has again an effect on the wind. In geostrophic balance, which is a good approximation for the free atmosphere, the wind is parallel to the isobars. This explains the differences that occur exemplary on 23 June 2021, 12 UTC, between the +50%-simulation with southwesterly winds over whole Germany and the -50%-simulation with mainly southerly winds, even with a slight easterly component, in northern Germany (Fig. 3.3). These differences can lead to a propagation of the cells in different directions even if the wind direction of the initial data is kept constant.

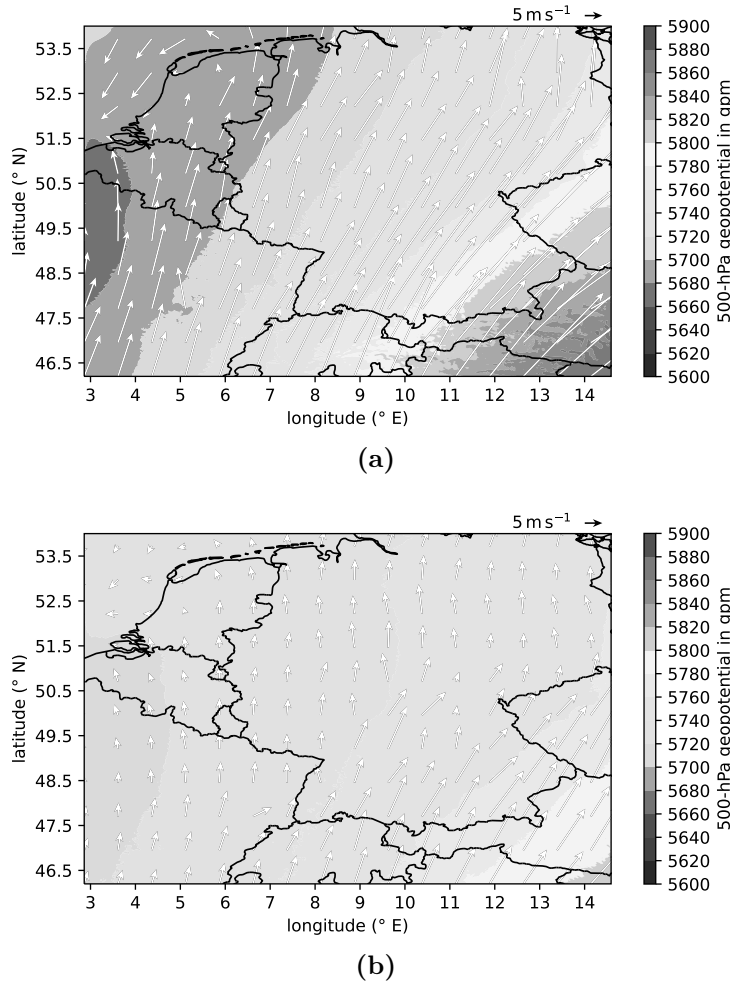


**Figure 3.3:** Field of 500 hPa geopotential and 500 hPa horizontal wind for the whole ICON simulation domain on 23 June 2021, 12 UTC in the (a) +50%-simulation and (b) -50%-simulation.

### 3.3 Data for comparison of model output with reality

For the comparison of the simulations with atmospheric observations, radiosoundings of the Swabian MOSES field campaign on 23 and 28 June 2021 and RADOLAN precipitation data from DWD are used. The radiosondes were launched in Stuttgart, Rottenburg and at the Campus North of KIT several times per day during the days with convective activity. Therefore, vertical profiles of atmospheric variables are known for the launching times. The wind profile of the model output in the reference simulation can be compared with the one measured by the sounding. They should be similar in order to produce reasonable results for convective activity with the model. In the first hours of the day, there are still some discrepancies in the wind direction of the lowest layers. The wind speed is already represented well by the model. After a few hours, wind speed and wind direction are fairly similar in the sounding and model, as is shown exemplary for one location and time step in Fig. 3.4. Some discrepancies can occur also during the day because the model profile is taken from

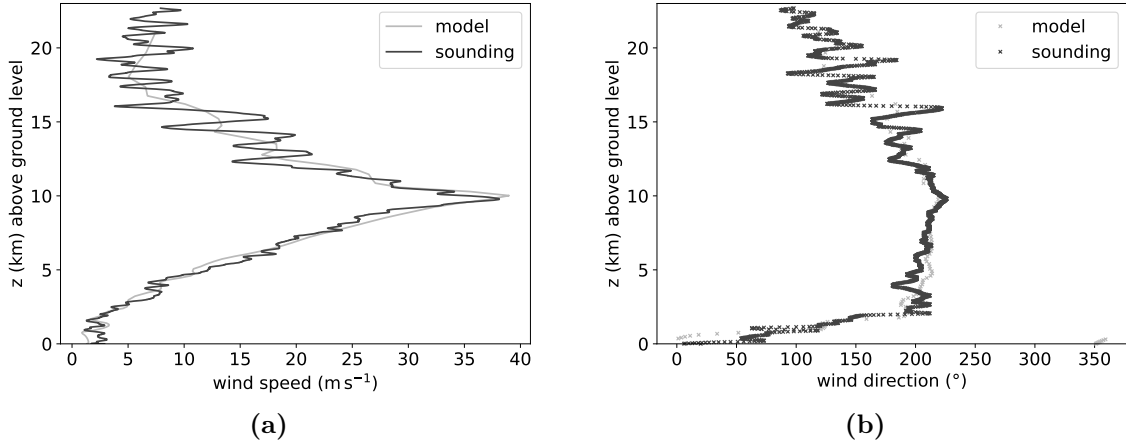


**Figure 3.4:** Comparison of (a) wind speed and (b) wind direction from the model simulation with continental CCN concentration and the radiosounding of the Swabian MOSES campaign in Stuttgart on 23 June 2021, 11:30 UTC.

one grid point closest to the launching point of the sonde, whereas the sonde does not stay at the same coordinate during lifting. Also lifting up to the tropopause needs around 45 minutes, whereas the model output in the different heights is taken at the same time point. In the evening, after the convection occurred, there are again larger differences between the model and sounding at some locations dependent on how the convection evolved in the model.

The RADOLAN precipitation data are compared with the model precipitation to see if the model produces reasonable precipitation amounts and most of the convective cells. The RADOLAN data are based on radar data. However, as a radar does not measure surface precipitation directly but only signals reflected by hydrometeors in atmospheric layers, radar data do not give an exact amount of surface precipitation. Therefore, the spatial distribution of precipitation is taken from the radar and combined with the amount of surface precipitation measured by classical ombrometers on the ground, named RADOLAN data (DWD, 2023). The RADOLAN data are available in hourly resolution.



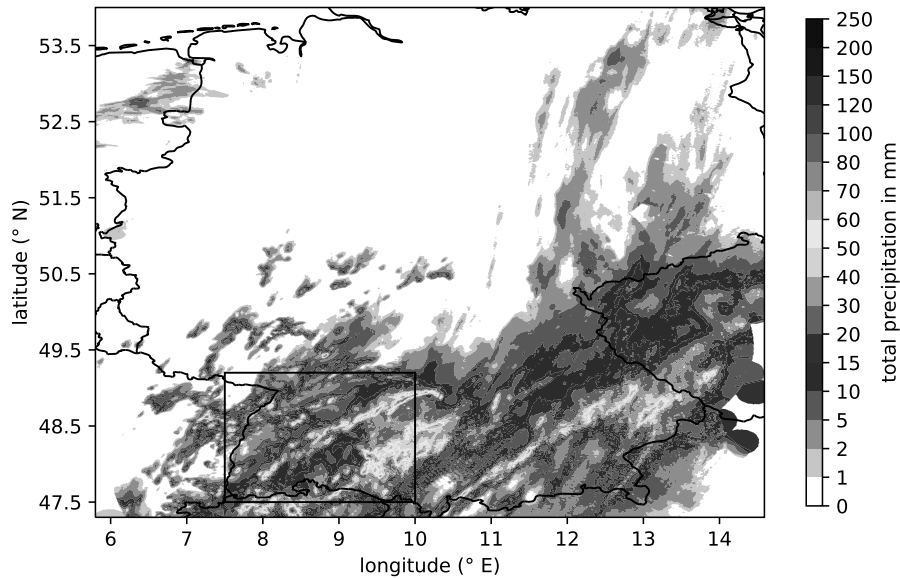


**Figure 4.1:** Accumulated surface precipitation over Germany and some bordering regions on 23 June 2021 according to RADOLAN data. The domain of the Swabian MOSES campaign is indicated by the black box.

## 4. Observed precipitation on simulation days

For an overview of the surface precipitation, the RADOLAN data described in section 3.3 are used. The resulting surface precipitation in its diurnal development as well as in its accumulated feature on the three simulation days is described in the following sections.

### 4.1 23 June 2021

On the first simulation day of the Swabian MOSES field campaign, 23 June 2021, the precipitation mainly occurs over southern Germany (Fig. 4.1). Some less intense precipitation features occur also in northeastern Germany and in the northwestern part on the Dutch border. Some isolated cells also occur over western central Germany. In the first hours of the day, some precipitation cells already exist over Baden Württemberg and more intense over Bavaria. The precipitation features intensify while the cells move towards the northeast. Around 10 UTC, there are only some low intense remnants over northeastern Germany from the former precipitation cells over Bavaria. Around 12 UTC, the first smaller-scale but more intense cells develop inside the Swabian MOSES area and north of it. The first cells dissipate fast, but in the afternoon, there is a supercell with high rain intensity over Baden Württemberg, which can be tracked for several hours and whose storm track is also visible in

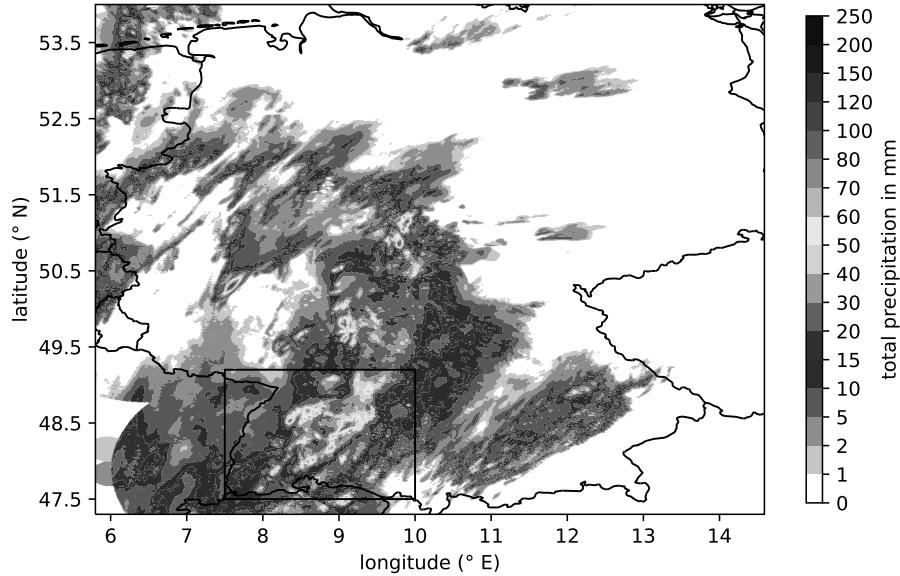


**Figure 4.2:** Same as in Fig. 4.1, but for the second simulation day of the Swabian MOSES field campaign, 28 June 2021.

Fig. 4.1. This cell existed for 7.5 hours and along a path of around 190 km (Barthlott et al., 2023). South of it, some small-scale cells merge to a larger precipitation feature. Over Bavaria, also a longer-lived cell and a merged larger precipitation feature can be seen in the accumulated surface precipitation.

## 4.2 28 June 2021

The second simulation day, 28 June 2021, is characterized by large precipitation features within the domain of the Swabian MOSES campaign and north of it in central Germany (Fig. 4.2). There is some precipitation over Bavaria, but less compared to the first simulation day. Some smaller-scale cells with relatively high intensities occur over the western and northwestern part of the area shown in Fig. 4.2. In the first hours of the day, there are only some light precipitating features, mostly inside the MOSES-domain. In the following hours, some precipitation is advected from regions west of the displayed domain. In the afternoon around 14 UTC, the first intense convective cells develop over the Black Forest mountains but also in western Germany. During the following hours, some quite intense cells develop close to each other in the MOSES-domain and north of it, resulting in a large contiguous area with accumulated large precipitation amounts. In the last hours of the day, there is nearly no precipitation over the MOSES-domain anymore, but over Bavaria, cells develop and move towards the northeast. Some cells also occur in central Germany during the last hours of the day.

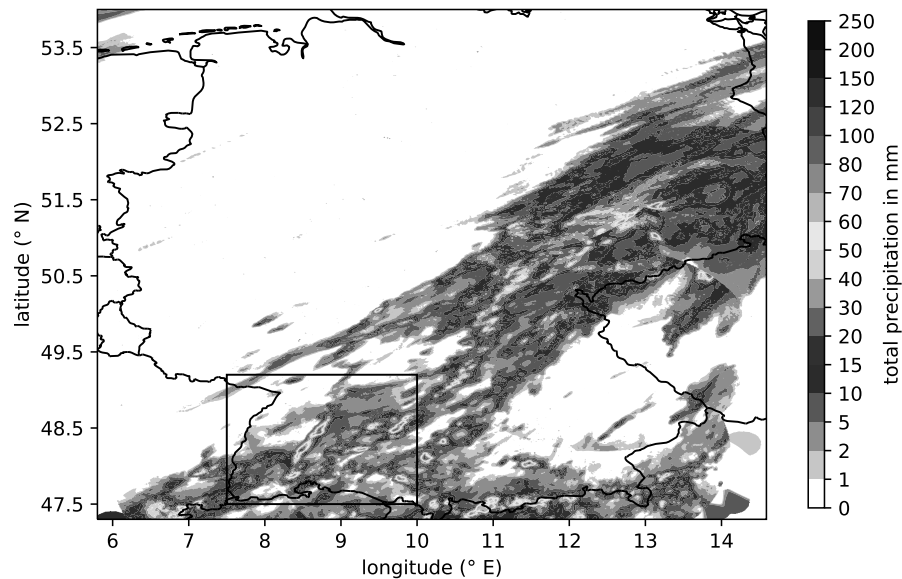


**Figure 4.3:** Same as in Fig. 4.1 and Fig. 4.2, but for the third simulation day, 22 July 2015.

### 4.3 22 July 2015

On 22 July 2015, the most intense cells develop within the area where the Swabian MOSES campaign takes place six years later (Fig. 4.3). Quite large precipitation amounts also occur in a larger feature extending from southwest to northeast in the central eastern part of Germany. Some very intense cells are embedded in this feature. In the Alps, along the Austria–Germany border, intense cells develop as well. On this day, no precipitation occurs in the first hours of the day. The first cells appear around noon. They mainly develop over the Alps, one cell also west of the MOSES area. Due to the propagation of this cell and some new developing convection in southwestern Germany, intense precipitation occurs inside the MOSES area in the following hours. Most of the cells along the Alps dissipate until the evening. The cells from the MOSES-domain move towards northeast, where also new cells develop. This leads in accumulation to quite intense precipitation over eastern Germany in Fig. 4.3. Around 22 UTC, new convective cells develop inside the MOSES area after a few hours of no convective activity.



# 5. Impact of wind shear on convective precipitation and ACI

In the first part of this chapter, the focus is solely on the influence of the wind shear on convective precipitation. Discrepancies in thermodynamic and dynamic variables are presented to explain differences in the simulations of the five shear realizations. In the second part, CCN concentration is introduced as an additional variable. The effect of the aerosols on the convective precipitation is shown, as well as how the aerosol effects change with varying wind shear. For the investigations in this chapter, mostly spatial averages and sums over a domain named DE-domain extending from 5.8°E to 14.59°E and from 47.3°N to 54.0°N are used, sometimes also results of the MOSES-domain (Fig. 3.1) when convection mostly takes place in this area. At the end of this chapter, the precipitation efficiencies of the simulations are presented.

## 5.1 Effect on convective precipitation

To investigate the impact of wind shear on convective precipitation without considering CCN dependency, only the simulations with continental CCN concentration are considered. This condition is closest to the reality over a continental region like the DE-domain. In the following, different variables in five simulations with the same CCN concentration but different wind shear are therefore compared for each of the three simulation days.

### 5.1.1 Case of 23 June 2021

The model simulations with reference, decreased and increased vertical wind shear all show, on average, a similar diurnal cycle for the DLS with a maximum between 15 and 18 UTC (Fig. 5.1). As could be seen from Fig. 2.4, a value of around  $20 \text{ m s}^{-1}$  and more for the DLS is a favorable condition for the development of supercells. In the reference run, the maximum DLS value is only around  $15 \text{ m s}^{-1}$  and not favorable for supercell development. However, this is an averaged value over a larger domain and locally higher values exist in regions where the supercell formed. Looking at the share of grid points that exceed a special threshold (not shown), around 25% of all grid points have values above  $20 \text{ m s}^{-1}$  in the afternoon, and some grid points have even higher values than  $25 \text{ m s}^{-1}$ . When lowering the vertical wind shear in the initial conditions, the DLS gets also smaller not only on average but also for the single grid points in that way that nearly no grid points fulfill the threshold of  $20 \text{ m s}^{-1}$  in the -50%-simulation. In contrast, nearly half of all grid points have larger DLS than  $20 \text{ m s}^{-1}$  in the +50%-simulation.

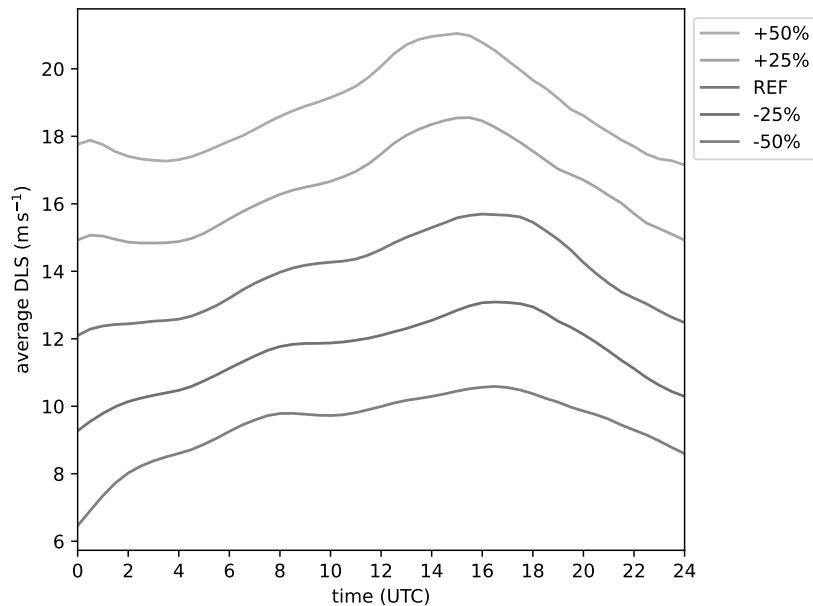


**Figure 5.1:** DLS averaged over the DE-domain on 23 June 2021; different colors indicate different vertical wind shear (reference and modified) in the initial ICON-EU data.

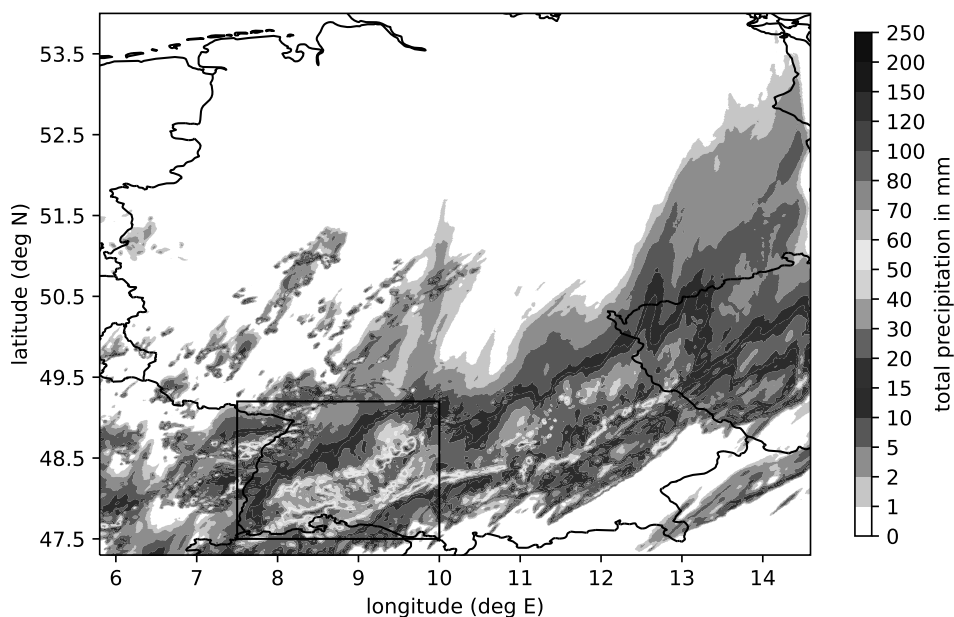


**Figure 5.2:** Distribution of total precipitation over the DE-domain on 23 June 2021 for the reference shear simulation; black box indicates the area of the Swabian MOSES field campaign.

After DLS affects what type of convective cells occur, the model output of precipitation varies greatly depending on the shear case. For the reference run, there is most of the precipitation over the southern German federal states of Baden-Württemberg and Bavaria (Fig. 5.2). The accumulated precipitation in these areas results mostly

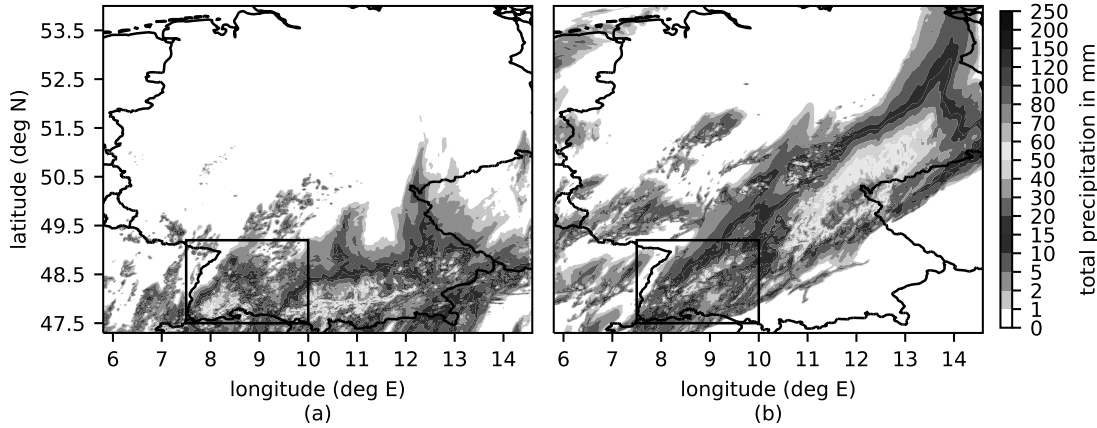


**Figure 5.3:** Distribution of total precipitation over the DE-domain on 23 June 2021 for (a) the  $-50\%$ -simulation and (b) the  $+50\%$ -simulation; black box indicates the area of the Swabian MOSES field campaign.

from longer-lived cells, which can be tracked with the 30 min precipitation data. In addition, there are some short-lived cells over central western Germany. In the northern part of Germany, there is no precipitation in the simulation.

When comparing the model output with the precipitation data from RADOLAN (Fig. 4.1), it is visible that the most intense convective features are well captured by the simulation. This includes the intense cells embedded in the larger regions with much precipitation within the Swabian MOSES area and Bavaria. However, it is noticeable that there is no precipitation in southeastern Bavaria in the simulation, where some takes place in reality. Also the positions of the convective cells are slightly shifted. This is also the case for the smaller-scale cells in the France–Germany border region or in central western Germany, which are well represented by the model. Even if the diurnal cycle of the precipitation is also well captured by the simulations, there are some representation problems for the low intense precipitation in the first hours of the simulation. This also explains why no precipitation can be seen in northwestern Germany in the model output. However, such weak and already existing precipitation is not of interest for the present thesis.

For simulations with changed wind shear in the initial and boundary data, differences to the reference simulation and also the RADOLAN data are expected. The smaller the DLS, the less organized is the convection on 23 June 2021 (Fig. 5.3a). In the case of the  $-50\%$ -simulation, the accumulated precipitation results from cells with a shorter lifetime. Most of the cells occur over southern Germany. Also cells during the morning which reached further north into eastern Germany in the reference run have a more eastward movement in the reduced wind shear simulation, leading to less precipitation northeast of Bavaria. In contrast, the convection is

more organized for increased vertical wind shear, resulting in a large feature of large precipitation amounts (Fig. 5.3b). The system in the morning hours has a more northerly component. Also later in the day, the cells embedded in larger precipitation systems reach further northeast in Germany. Because both times the cells and their propagation area have a similar location, a band of accumulated precipitation reaching from southwest to northeast with the largest amounts further northeast than in the reference simulation is visible. Note here, that the different accumulated precipitation distributions are also a consequence of a direction change of cell propagation even if only the wind speed is changed in the initial conditions, as it is explained in section 3.2 and Fig. 3.3. Considering the major damage on that day mentioned above, it is of interest to see that in the case of increased shear, larger but also different areas would be affected by very heavy rainfall.

Longer-lived and more organized convection in the increased shear cases leads not only to a different spatial distribution of the precipitation but also to differences in the amount of fallen precipitation. The five different shear case simulations on 23 June 2021 performed for this work show that an increase in the vertical shear leads to a systematical increase of the precipitation amounts over Germany (Fig. 5.4a). This is due to more organized convective cells, whose tracks can be followed in the half-hourly precipitation rates and become visible in the accumulated precipitation as a coherent feature. The amount of precipitation is more than 30% larger in the +50%-simulation than in the reference simulation. A decrease of shear leads to a systematical decrease of the precipitation sum with a maximum decrease in the -50%-simulation of around -28%.

The temporal distribution of precipitation among the day is similar for the different simulations (Fig. 5.4b). In all cases, there are already cells early in the course of the day. After a minimum of precipitation rate around 12 to 15 UTC, larger values occur in the late afternoon and evening in all cases, with a maximum around 22 UTC. Only the intensity of the precipitation is strongly differing between the different shear cases.

The main reason for the higher precipitation intensities in the stronger wind shear cases is the different evolution of mixed-layer CAPE. The CAPE is larger, the greater the wind shear (Fig. 5.5a), leading to the possibility of more intense convection when the CAPE is consumed. For all simulations, the diurnal cycle is nearly the same. In the -50%-simulation, it is only weakly pronounced. But for the CAPE values, there is a maximum difference of more than  $400 \text{ J kg}^{-1}$  between the +50%- and -50%-simulation even if the variable is averaged over the whole DE-domain. Locally, there are much larger differences between the simulations, which favor intense convection with cloud and precipitation development in the increased shear cases compared to

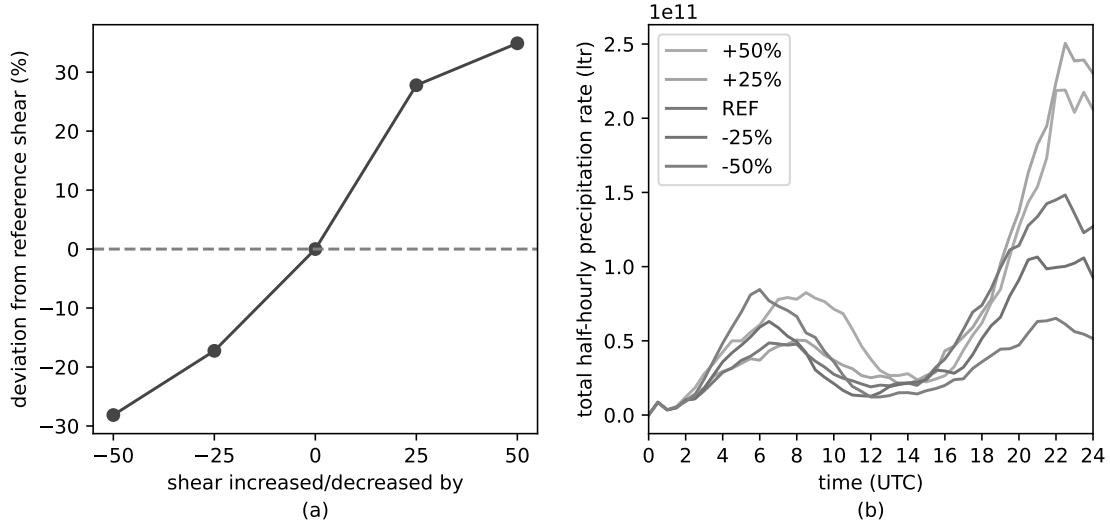


**Figure 5.4:** (a) Deviation of the total precipitation sum in the different shear case simulations from the reference shear simulation and (b) half-hourly precipitation rate with different colors indicating the initial vertical wind shear, both inside the DE-domain on 23 June 2021.

the decreased ones.

The differences in CAPE are mainly due to the different evolution of clouds in the different runs (Fig. 5.5b). The reason for the different cloud cover remains unclear even if considering several variables of the model output. During the day, when the incoming shortwave radiation is greatest, the cloud cover is smaller the stronger the wind shear is. This holds for low-level, mid-level and high-level clouds (not shown). Note that this is already the case before noon, even if the precipitation rate is clearly highest at this time for the +50%-simulation. As the share of grid points with precipitation (not shown) behaves similarly to the precipitation rate, there are more non-precipitating clouds in the weaker shear simulations. In the late afternoon, the behavior of the total cloud cover is not that systematic anymore, especially due to an increase in high-level clouds in the simulations with increased shear.

Nevertheless, the different cloud cover in the different simulations leads to differences in the averaged net radiation on the surface of maximum  $44 \text{ W m}^{-2}$  between the -50%- and the +50%-simulation (Fig. 5.5c). After more radiation is available on the surface for stronger shear cases, a stronger sensible and latent heat flux leads to a higher 2-m temperature and 2-m humidity for those cases. Temperature and humidity together result in the equivalent potential temperature  $\theta_e$ . As it is depicted in Fig. 5.5d, large differences occur in the averaged 2-m equivalent potential temperature between the different shear case simulations over the whole course of the day. In the afternoon, the +50%-simulation has more than 6 K higher values

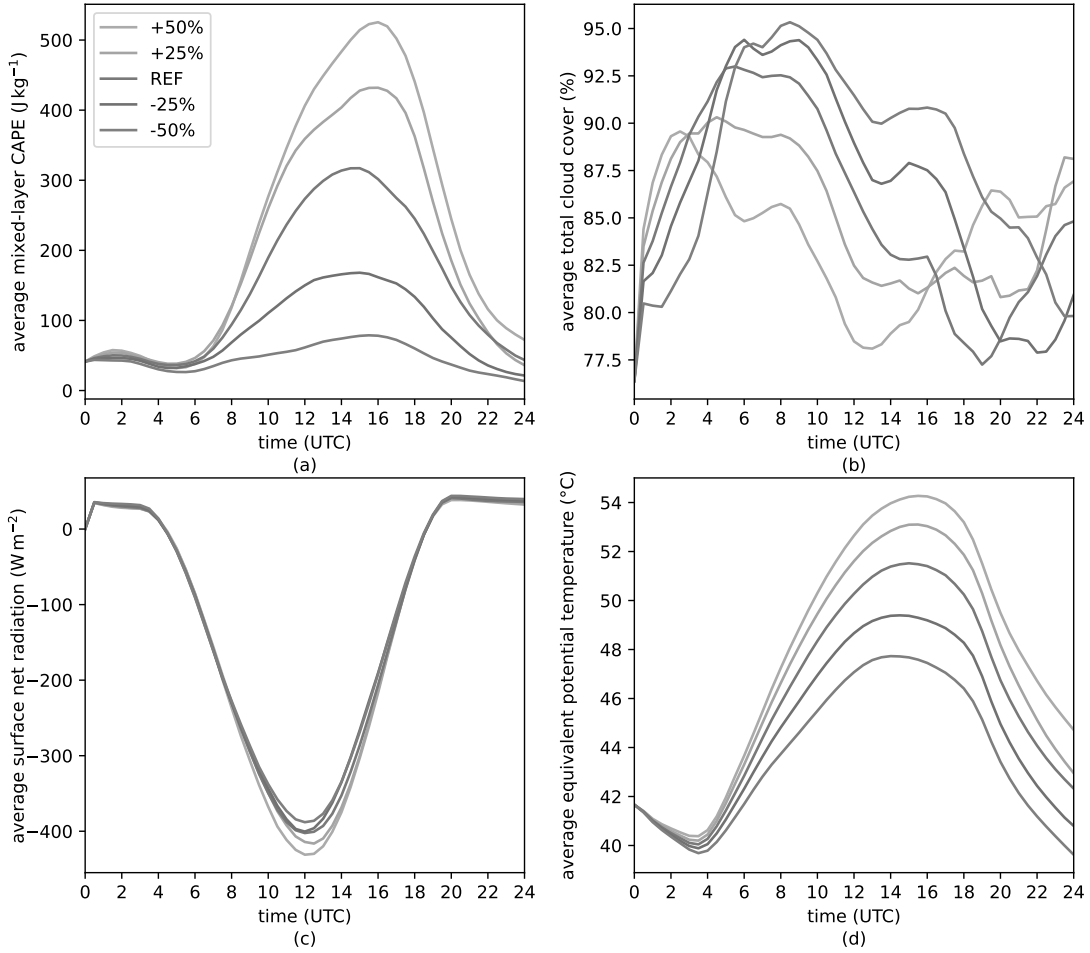


**Figure 5.5:** (a) Mixed-layer CAPE, b) total cloud cover, (c) net radiation on the surface and (d) 2-m equivalent potential temperature averaged over the DE-domain on 23 June 2021.

than the  $-50\%$ -simulation.

As mentioned in section 2.1.4, there is a correlation between equivalent potential temperature and CAPE. Since the values of  $\theta_e$  are averaged in this work over the whole DE-domain, the values in Fig. 5.5d are below the range shown in Fig. 2.3, but there are grid points with clearly higher  $\theta_e$ . Differences of several Kelvin between the stronger and weaker wind shear simulations can explain why the mixed-layer CAPE, and as a consequence of this, the precipitation are that different in the simulations with different wind shear on 23 June 2021.

### 5.1.2 Case of 28 June 2021

On 28 June 2021, the time of the day when the highest values of DLS occur is a bit shifted compared to 23 June, especially for the weak shear simulations in which the maximum already takes place in the morning (Fig. 5.6a). However, considering the

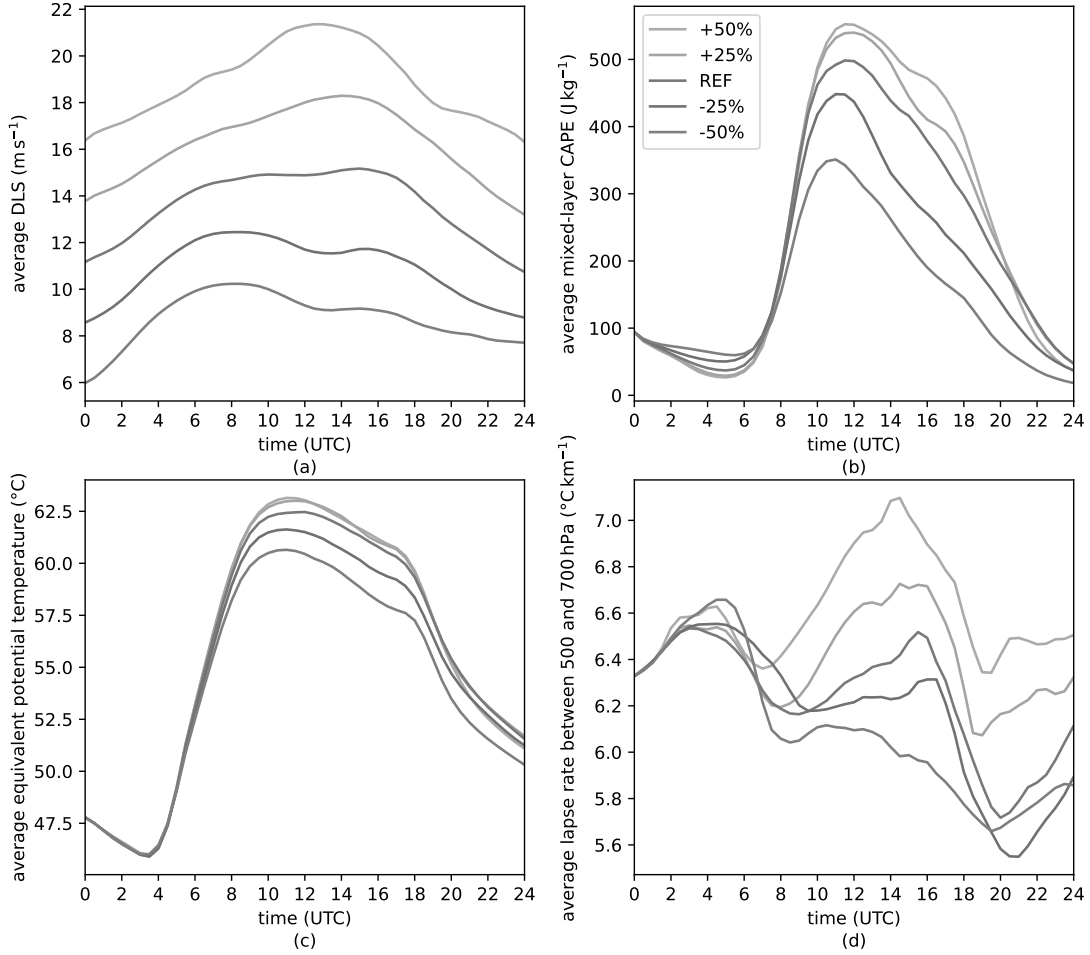


**Figure 5.6:** (a) DLS, (b) mixed-layer CAPE, (c) 2-m equivalent potential temperature, all three averaged over the DE-domain and (d) lapse-rate between 500 and 700 hPa averaged over the MOSES-domain on 28 June 2021.

average values for DLS and the share of grid points above different thresholds (the latter one not shown), the two simulation days, 23 June and 28 June, can be classified as similar in terms of vertical wind shear. As on the first simulation day, the potential for convection indicated by the mixed-layer CAPE is higher for the strong shear than for the weak shear cases during the day (Fig. 5.6b). The differences between the shear cases mainly have two reasons: as above, differences in the equivalent potential temperature play a role (Fig. 5.6c). Second, earlier triggering of convection in the weaker shear cases, also visible in an earlier onset of precipitation (Fig. 5.7b), is responsible. The earlier convection at some places increases the stability locally and therefore leads to a weaker development of CAPE in the daily cycle. The stabilization can be seen from the lapse rate between 500 and 700 hPa, averaged over the MOSES-domain where most of the early convection takes place in the  $-50\%$ -simulation (Fig. 5.6d). In this area, differences of around  $1 \text{ K km}^{-1}$  result

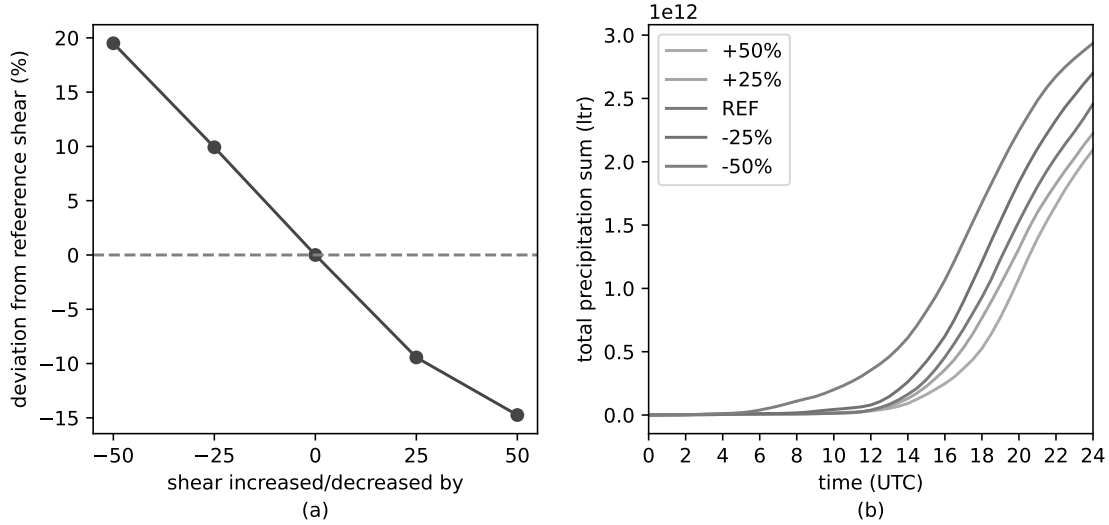


**Figure 5.7:** (a) Deviation of the total precipitation sum in the different shear case simulations from the reference shear simulation and (b) accumulated total precipitation, both over the DE-domain on 28 June.

after stabilization. However, in comparison with 23 June, the differences in CAPE between the different shear cases are not that large as a consequence of much smaller differences in equivalent potential temperature of maximum 2.5 K.

Even if the CAPE differs less between the shear cases on 28 June, the two variables DLS and CAPE suggest that convection could develop similarly to that on the first simulation day in section 5.1.1. However, the precipitation output of the simulations shows an exactly opposite systematic behavior than on 23 June: the weaker the vertical wind shear in the initial data, the larger the precipitation amount (Fig. 5.7a). The relative differences between the different shear cases are smaller than on 23 June, reaching from +20% in the -50%-simulation to -15% in the +50%-simulation. The absolute differences are also smaller (not shown here but visible in Fig. 5.17b and Fig. 5.19b in section 5.2).

The earlier onset of precipitation contributes to the overall higher precipitation values in simulations with weaker shear. Partly cells formed by local-scale uplift mechanisms over the Alps in Switzerland during the first hours of the day move inside the DE-domain in the weak shear cases a few hours later. Those cells cannot be seen in the other simulations. Regardless of these cells, the precipitation rate is higher in weak shear cases also in the morning hours up to noon when the cells are initiated within the DE-domain. The reason for that and for less precipitation in the increased shear cases is the CIN. As mentioned in section 2.1.4, the convective potential in the atmosphere expressed by the CAPE can only be exploited if the CIN can be overcome. Therefore, the combination of both variables is important

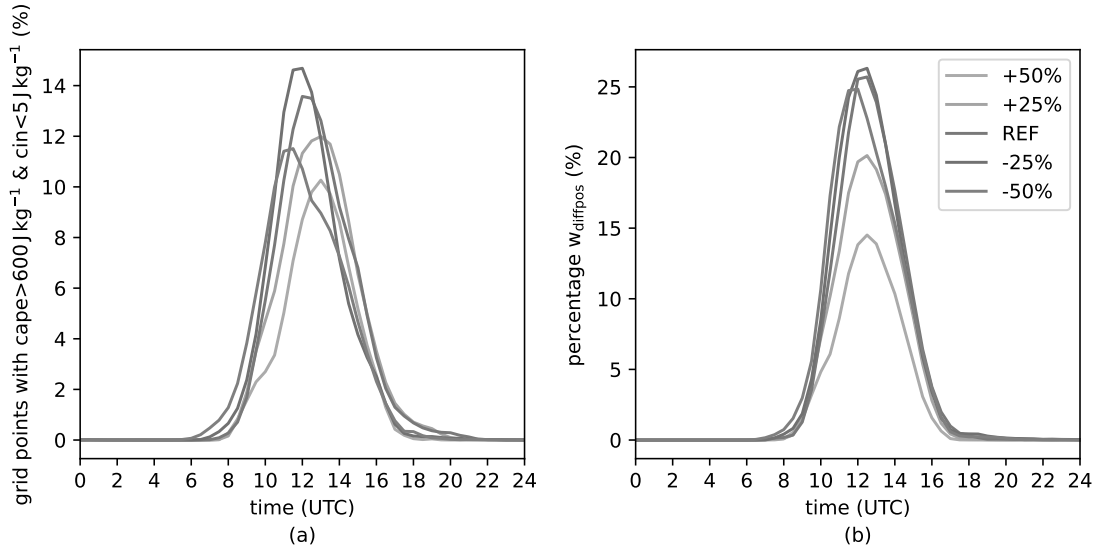


**Figure 5.8:** Share of grid points with (a) a mixed-layer CAPE larger than  $600 \text{ J kg}^{-1}$  and a mixed-layer CIN smaller than  $5 \text{ J kg}^{-1}$  and (b) a higher vertical velocity within the lowest 2 km than is necessary to overcome the energy barrier of the CIN (named as  $w_{\text{diffpos}}$ ) in the DE-domain on 28 June 2021.

for the triggering of convection. Fig. 5.8a shows that the lowest share of grid points in the DE-domain fulfills the criterion of exemplary values for the CAPE of more than  $600 \text{ J kg}^{-1}$  (can be much larger) and for the CIN of less than  $5 \text{ J kg}^{-1}$  in the +50%-simulation even if the CAPE is larger in these cases. However, a greater CIN ensures that convection cannot be triggered at some places with large CAPE.

Also a variable called  $w_{\text{diff}}$  is calculated:

$$w_{\text{diff}} = w_{\text{max},2\text{km}} - w_{\text{cin}}. \quad (5.1)$$

This variable contains the difference of actual maximum vertical velocities within the lowest 2 km ( $w_{\text{max},2\text{km}}$ ) and the vertical velocity necessary to overcome the CIN energy barrier ( $w_{\text{cin}}$ ), the latter one known from equation 2.14. Positive values for  $w_{\text{diff}}$  indicate that convection can be triggered and the CAPE can be released (Schneider et al., 2018). From looking at how many grid points show positive values for that variable (named as  $w_{\text{diffpos}}$ ), it is visible that clearly less grid points can overcome the energy barrier of CIN in the stronger shear cases than in the reference and weaker shear cases (Fig. 5.8b). For the -50%-simulation, the amount of grid points that fulfill the CAPE and CIN threshold criterion is not largest during the day, which is related to the earlier onset of precipitation in those simulations.

With the same variable as in Fig. 5.8 but for a domain only in the southwestern region of the model area reaching further southwest than the DE-domain where convection is triggered over the Alps, the difference between the -50%-simulation

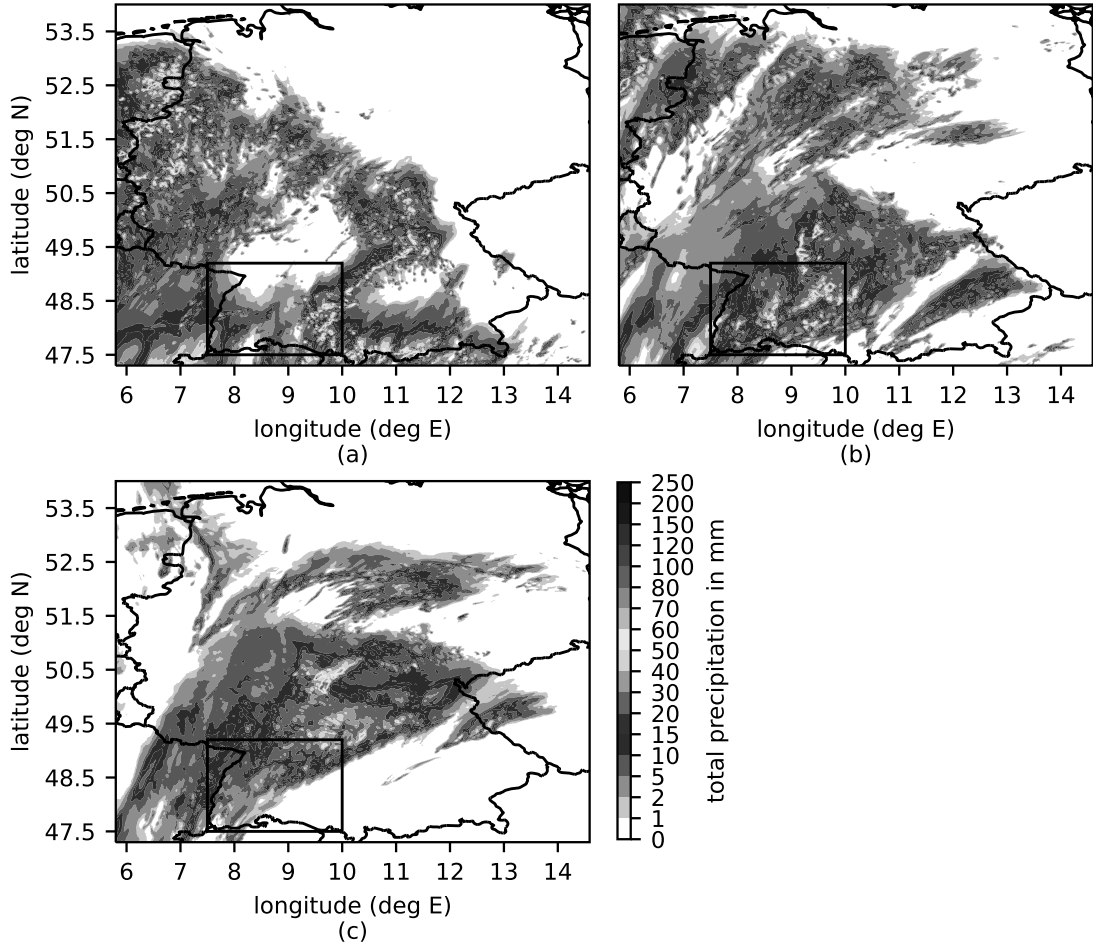


**Figure 5.9:** Spatial distribution of total precipitation on 28 June 2021 in the DE-domain for (a) the  $-50\%$ -shear simulation, (b) the reference shear simulation and (c) the  $+50\%$ -shear simulation; black box indicates the area of the Swabian MOSES field campaign.

and the others becomes even clearer (not shown). This indicates and confirms that favorable convective conditions are reached earlier in the  $-50\%$ -simulation. Even if the averaged values are not that large during the morning, the CAPE is in general greater in this simulation at this time as a consequence of clearly more mid-level and low-level clouds, therefore less outgoing radiation and therefore slightly higher  $\theta_e$ . CIN is also smaller, which is a consequence of higher specific humidity in the surface layer and therefore on average lower altitude of the LFC (not shown). The combination of CAPE and CIN leads to an earlier triggering of convection at some locations in the southwestern model area, including the MOSES-domain.

The spatial distributions of accumulated precipitation differ on this day (Fig. 5.9) compared to the first simulation day, as it was also in reality (Fig. 4.2). As on 23 June, the distribution is characterized by many small cells for decreased shear. The greater the shear gets, the more contiguous the precipitation feature looks like. This similarity to 23 June fits with the condition of somehow similar wind shear.

In principle, the most intense precipitation accumulation in the reference simulation takes place in southwestern Germany within the area of the Swabian MOSES field campaign (Fig. 5.9b). Some rain also occurs over Bavaria and many smaller cells over a larger domain in northern and northwestern Germany. Compared to the RADOLAN data (Fig. 4.2), the model produces less precipitation in central Germany and more precipitation over northern Germany. A good representation of the cells over Bavaria and the northwestern DE-domain is possible with the model, as well as the temporal evolution of the cells within the MOSES-domain, even if they are slightly spatially displaced.

In the increased shear case in Fig. 5.9c, the main precipitation field is shifted further northwards, mainly outside of the MOSES-domain. Less single cells occur over the northwestern part of Germany, and the precipitation is focused more on one smaller region in central to northern Germany. In the decreased shear cases, different regions with precipitation occur (Fig. 5.9a). Eyecatching are the large precipitation amounts over northwestern Germany and over the Alps along the Austria–Germany border, which are much greater than in the other shear cases. North of the MOSES-domain, where most of the precipitation takes place in the +50%-simulation, there is no precipitation, but over northern Bavaria instead.

These spatial differences reflect the previously elaborated results on CAPE and CIN. Higher values for the CAPE can be seen over the Alps for the increased shear simulations (not shown). The problem is that CIN is also too large to trigger convection in this stronger shear simulation. However, there is some CAPE in the –50%-simulation, and the CIN is very small, which ensures that cells are formed, which contribute to a large part to the large precipitation amounts in the –50%-simulation. The same also applies to the northwestern region with strong precipitation.

### 5.1.3 Case of 22 July 2015

The third simulation day, 22 July 2015, is characterized by larger DLS on average than the other two simulation days (Fig. 5.10a). The diurnal cycle is different as well and dependent on the shear in the initial data. However, these high average values are strongly influenced by very large DLS in northern Germany, where nearly no CAPE and no precipitation occur on that day. When considering the Swabian MOSES area, which represents an area where a large part of the precipitating cells are initiated on that day, the shear averaged over that area is actually well below the other days (not shown).

The diurnal cycles of the mixed-layer CAPE in the different simulations (Fig. 5.10b) are similar to the ones from 28 June 2021 (Fig. 5.6b). The differences between the CAPE in the weakest and strongest shear simulations are even smaller on 22 July

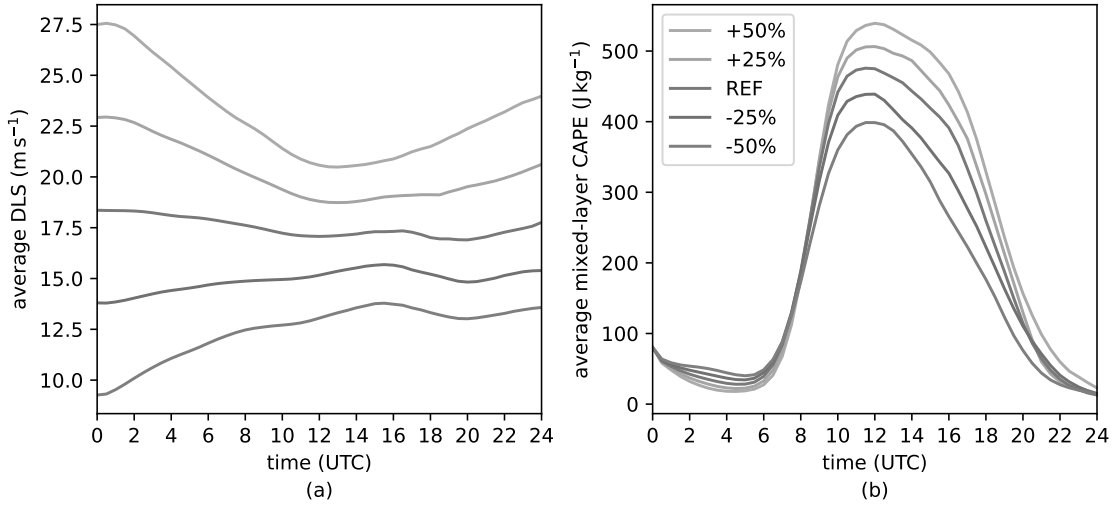


**Figure 5.10:** (a) DLS and (b) mixed-layer CAPE averaged over the DE-domain on 22 July 2015.

2015. The reason for that is that precipitation starts at the same time in the different simulations on the third simulation day (Fig. 5.11a) because there is not a region with a clearly earlier evolution of favorable convective conditions as on the second simulation day. Therefore, no earlier stabilization, which reduces the CAPE, takes place in the weak shear simulation. The difference in CAPE is then determined by the different equivalent potential temperature alone, which is fairly similar to that variable on 28 June 2021 (Fig. 5.11b). Different equivalent potential temperatures follow from different 2-m humidity and 2-m temperature as a consequence of different low and medium cloud cover (not shown).

In contrast to 28 June, the CIN combined with CAPE (Fig. 5.12a) and also the variable  $w_{\text{diffpos}}$  (Fig. 5.12b) indicate less favorable convective conditions for the simulations with reduced wind shear. The most favorable conditions occur in the +25%-simulation, the least favorable ones in the -25%-simulation. From the shown averaged variables, it has to be expected that the higher convective potential and the possibility to overcome the CIN leads to more convective precipitation in the stronger wind shear cases. However, this is not the case. For the decreased shear simulations, the amounts of precipitation are larger and for increased shear, the amounts of precipitation become strongly smaller with around -60% for the +50%-simulation (Fig. 5.13d).

As mentioned in section 2.1.4, strong shear could also dissolve weak updrafts or prevent the initiation of convection. However, this can not explain the precipitation amounts of Fig. 5.13 because most of the convection develops in southern Germany on this day, where DLS is smaller than on the other days. The explanation for the

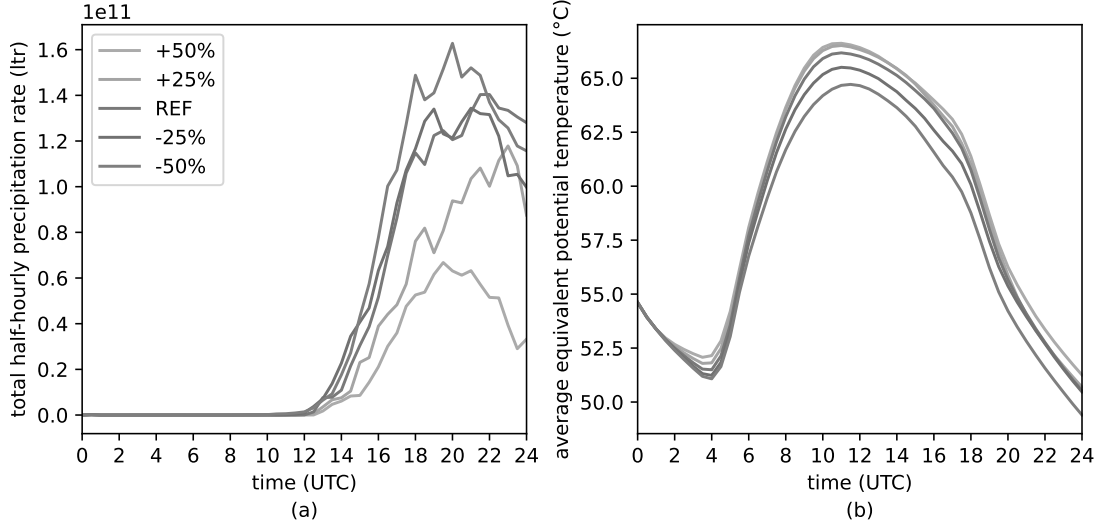


**Figure 5.11:** (a) Half-hourly precipitation rate and (b) averaged 2-m equivalent potential temperature inside the DE-domain on 22 July 2015.

large amounts of rainfall in the weaker shear case simulations can be found in regional differences in the decisive variables. On 22 July 2015, the cells mainly form over southwestern Germany in all simulations. Favorable conditions for convection in the weaker shear simulations occur in this region. CAPE has a completely opposite CCN dependency compared to the DE-domain, which follows from a different evolution of the vertical temperature profile already in the first hours of the day (not shown). Until the afternoon, higher maximum values for CAPE occur the smaller the shear is. CIN combined with CAPE and  $w_{\text{diffpos}}$  inside the MOSES-domain (Fig. 5.12c and d) also suggest that stronger cells can develop in the weaker shear cases in southwestern Germany. This leads to the different precipitation amounts in Fig. 5.13.

In the reference simulation, the cells move towards northeast, some of them intensify in regions of large CAPE in eastern Germany and merge into bigger systems. The accumulated precipitation feature reaching from southwest to northeast reflects the actual precipitation from the RADOLAN data well (Fig. 4.3). In the +50%-simulation, the cells do not intensify that much as in the reference simulation because most of them move a bit further south in a region of smaller CAPE than the cells in the reference simulations do. In the -50%-simulations, more cells are generated in the southwestern part of Germany, which fits with the better conditions of large CAPE and small CIN in the Swabian MOSES region (Fig. 5.12c and d). These cells move mainly towards the north, where convergence in a region of large CAPE helps to regenerate new cells or to keep them alive.

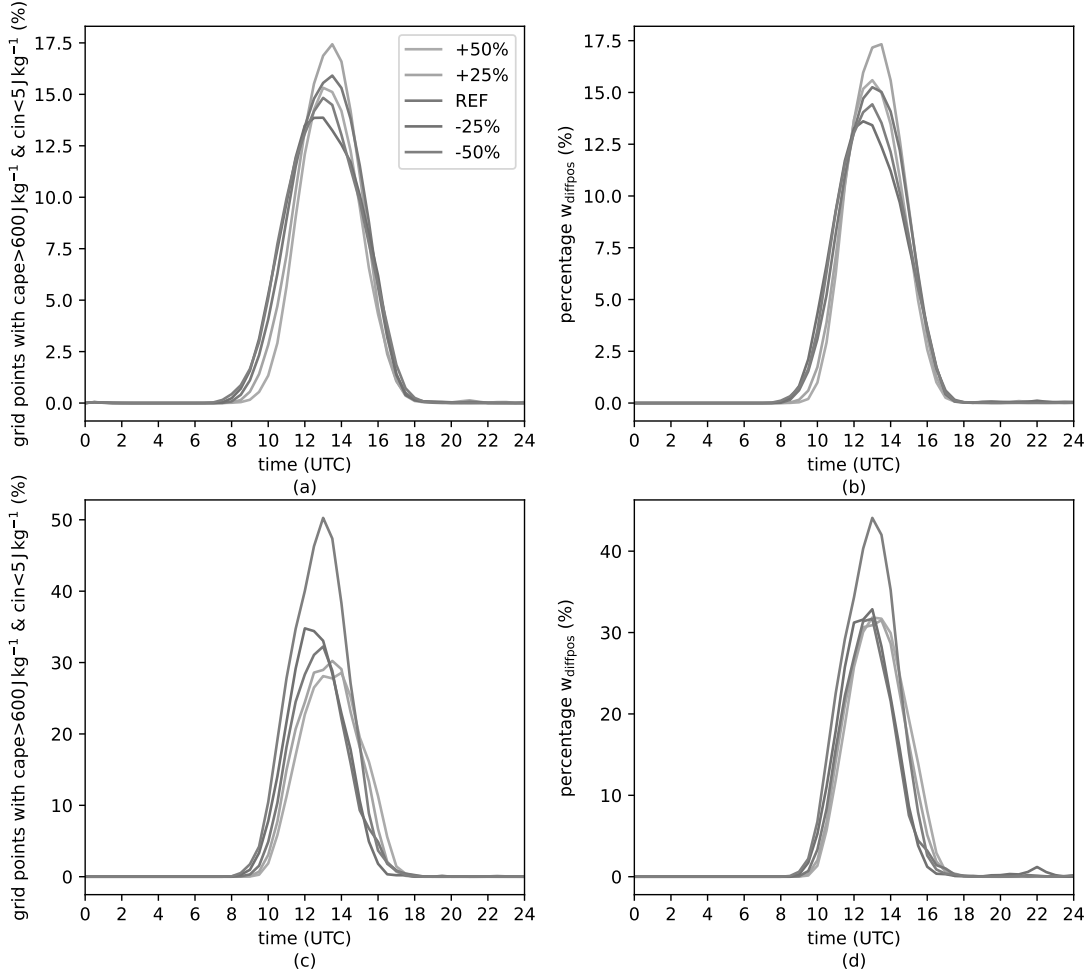


**Figure 5.12:** Share of grid points with (a) a mixed-layer CAPE larger than  $600 \text{ J kg}^{-1}$  and a mixed-layer CIN smaller than  $5 \text{ J kg}^{-1}$  and (b) a larger vertical velocity within the lowest 2 km than is necessary to overcome the energy barrier of the CIN (named as  $w_{\text{diffpos}}$ ) in the DE-domain on 22 July 2015; (c) is analogous to (a) and (d) to (b), but for the domain of the Swabian MOSES field campaign.

#### 5.1.4 General conclusions

From the three days with real-case simulations, it is not possible to state how vertical wind shear affects convective precipitation in general. For the first simulation day, a systematic increase in the amount of precipitation in the DE-domain was found for increasing wind shear, on the other two simulation days, a systematic decrease. The potential for convection expressed by the mixed-layer CAPE averaged over the DE-domain was always higher for the greater wind shear cases. This could be mainly attributed to the surface-near equivalent potential temperature, and on 28 June 2021 also to an earlier onset of convection in the weak shear cases accompanied by stabilization. On the first simulation day, 23 June 2021, the higher convective potential in the strong shear cases was released, resulting in stronger convection with more precipitation than in the small shear cases. In contrast, on the second

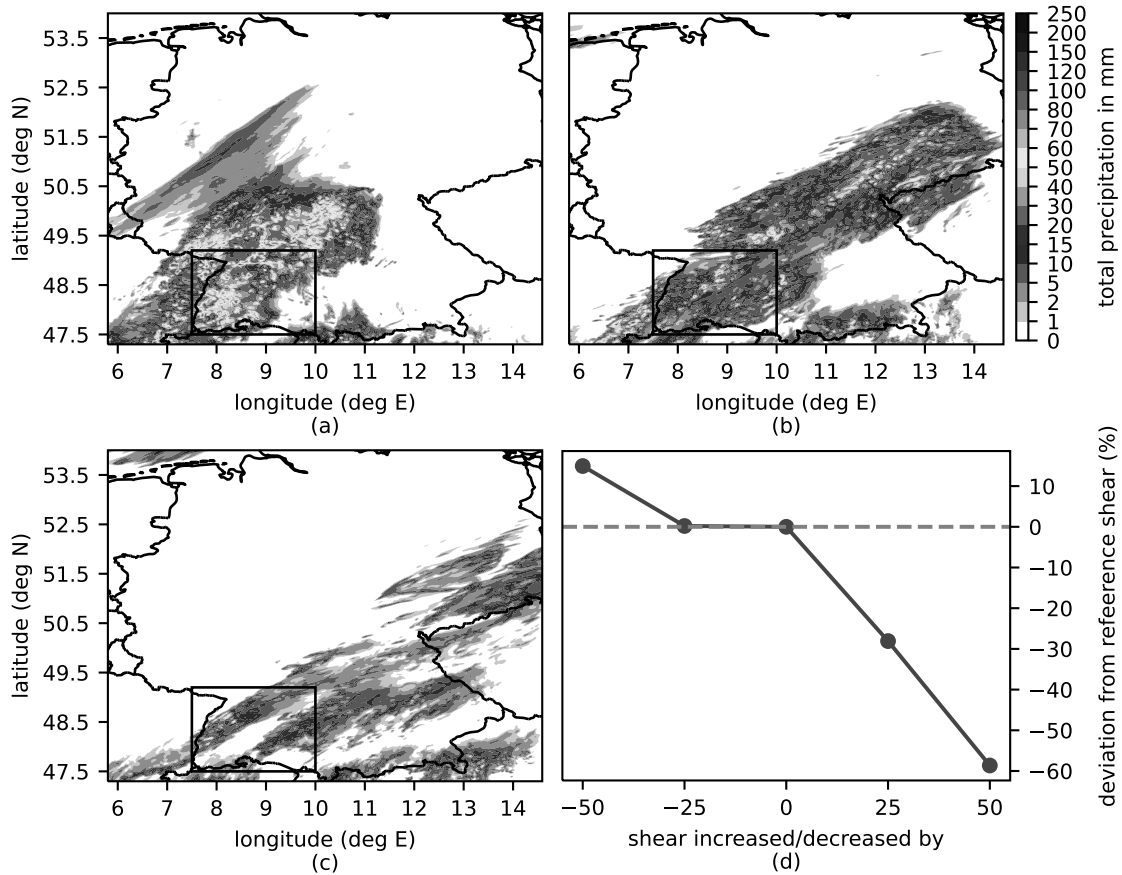


**Figure 5.13:** Spatial distribution of total precipitation on 22 July 2015 in the DE-domain for (a) the  $-50\%$ -shear simulation, (b) the reference shear simulation and (c) the  $+50\%$ -shear simulation with the black box indicating the domain of the Swabian MOSES field campaign; (d) deviation of the total precipitation sum in the different shear case simulations from the reference shear simulation over the DE-domain on 22 July 2015.

simulation day, 28 June 2021, the larger mixed-layer CAPE in the strong shear cases could not be released as the CIN was also greater on that day. A combination of both variables showed more favorable conditions for convection in the weak shear cases, resulting in the decreasing precipitation amounts with increasing vertical wind shear. From the third simulation day, 22 July 2015, it could be seen that a more local approach might be valuable if the cell development is mostly in a smaller domain. Favorable convective conditions in the smaller shear cases in the MOSES-domain representing southwestern Germany explained the decreasing precipitation amounts for increasing wind shear, which was not possible with the values averaged over the DE-domain.

## 5.2 Effect on ACI

In the following, all 20 simulations for each day consisting of the five shear cases from above and the four CCN concentrations maritime (m), intermediate (i), continental

(c) and continental polluted (p) are considered. Dynamic and thermodynamic variables are shown as well as hydrometeor contents and microphysical process rates to explain how varying wind shear affects the ACI and how this has an effect on the convective precipitation.

### 5.2.1 Case of 23 June 2021

There is a clear systematic increase for the total column integrated cloud water with increasing CCN concentration, in a similar way for the different shear cases (Fig. 5.14a). This increase is connected with the increasing amount of CCNs on which nucleation can take place. In contrast, the integrated rainwater decreases with increasing pollution. This is the consequence of a more efficient collision–coalescence for fewer but larger cloud droplets in low CCN concentrations, which is reflected in the systematical decrease with increasing CCN concentration in autoconversion and accretion (Fig. 5.14b). The CCN dependency for the warm rain processes is stronger for the stronger shear cases. However, this stronger dependency is not visible in the rainwater where a higher sensitivity occurs for the weaker shear cases, as also phase changes of frozen hydrometeors and evaporation can vary the amount of rainwater.

For the frozen hydrometeors ice and snow, an increase with increasing CCN concentration occurs in the simulations. The sensitivity is higher for snow. In the case of graupel, it is the other way around, and more CCNs lead to less graupel. The CCN dependency is stronger for the stronger shear cases than for the weaker ones. Hail is the least systematic variable but mainly increasing for increasing CCN concentration (Fig. 5.14a).

The development of cloud ice and snow is mainly dominated by the deposition of water vapor in the Wegener-Bergeron-Findeisen process. The increasing deposition rate with increasing CCN concentration explains the CCN sensitivity of snow and of cloud ice at least between maritime and continental CCN concentrations. However, as there are also some different processes that can determine the cloud ice content like freezing of liquid water droplets or raindrops, riming or melting of cloud ice, the exact same relationship as for deposition can not be expected for the cloud ice. The smaller sensitivity in deposition for weaker wind shear results in a smaller sensitivity at least in  $t_{qs}$  for these conditions. The deposition shown in Fig. 5.14b is combined of all frozen hydrometeors. When looking at the individual deposition rates (not shown), the CCN dependency is stronger for the deposition on snow than on cloud ice, explaining the higher sensitivity in  $t_{qs}$  compared to  $t_{qi}$ .

For the larger hydrometeors graupel and hail, the deposition can only slightly influence the results because riming is much stronger and more dominant. The riming rate decreases systematically for increasing CCN amounts in all shear cases. This is

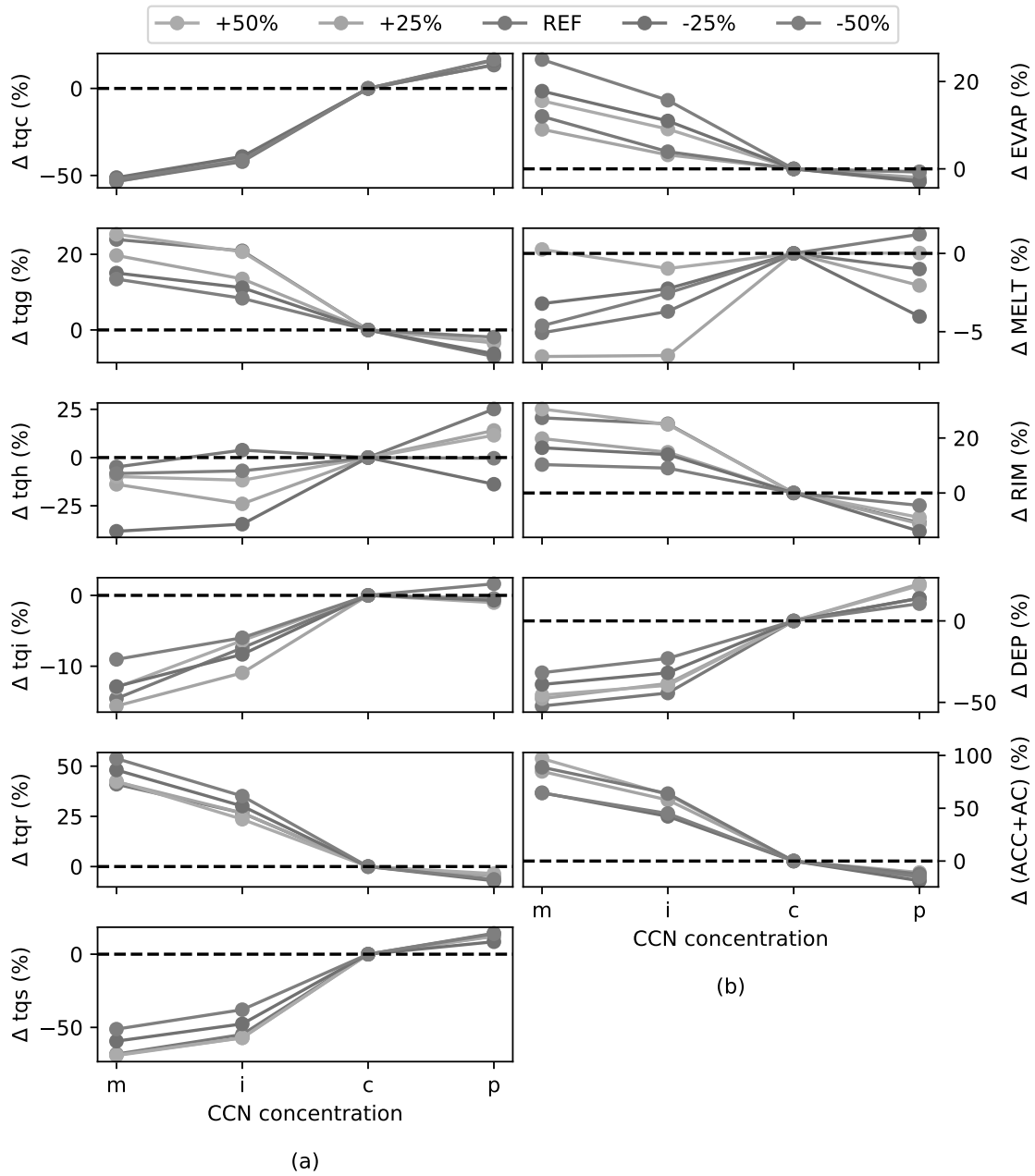


**Figure 5.14:** Percentage deviations from continental CCN concentration of spatiotemporal averages of (a) total cloud water (tqc), graupel (tqg), hail (tqh), ice (tqi), rainwater (tqr) and snow (tqs) and of (b) the vertically integrated microphysical process rates rainwater evaporation (EVAP), melting (MELT), riming (RIM), deposition (DEP) and warm rain formation processes accretion (ACC) and autoconversion (AC) together where the latter one is the smaller contributor. Different colors indicate the different wind shear cases. All shown simulations are for 23 June 2021 and the variables are averaged over the DE-domain.

a consequence of a smaller graupel-drop collision kernel in more polluted conditions (Cui et al., 2011). The decrease of the riming rate, also with the different CCN sensitivities for the different simulations, explains the behavior of tqg shown above. As the riming rates of graupel and hail are connected in the model output, it is not

possible to give an answer why the response of  $t_{qh}$  is contrary to  $t_{qg}$  and as would be expected from the decreasing riming rate. Overall, from riming and deposition, but also accretion and autoconversion, it can be seen that all precipitation formation processes are more CCN-dependent in the stronger shear cases.

As more rainwater occurs in lower CCN concentrations, a larger amount of it can evaporate. Therefore, the evaporation is decreasing with increasing CCN concentration, and the CCN sensitivity for the different shear cases is similar in evaporation and  $t_{qr}$ . An additional reason for the decrease in evaporation could be that, due to more but smaller cloud droplets, the raindrops can grow to larger diameters by collision-coalescence in polluted conditions (Altaratz et al., 2008). The larger the surface of the raindrop is in comparison to its volume, the easier evaporation can take place. Therefore, smaller raindrops in maritime conditions can evaporate more easily than larger drops in polluted conditions. The melting can be influenced by the size and amount of frozen hydrometeors. As there are frozen hydrometeors of increasing and decreasing amounts with increasing aerosol loading, the CCN dependency of the melting is not systematic and generally small.

The results for the CCN dependency of hydrometeor variables and microphysical process rates in Fig. 5.14 mainly fit with the results found in Barthlott et al. (2022b). In the cited study, graupel and rainwater also show a systematic decrease, and ice, snow and cloud water also a systematic increase for increasing CCN concentration. Only the percentage deviations differ in some cases. In contrast to the present study, hail amount decreases for increasing CCN amount in their simulations. The microphysical process rates are also similar, only for melting they found mainly a larger sensitivity, with a decrease for more CCNs. However, also in Barthlott et al. (2022b) there are cases which barely show any systematic for melting.

As rain is the main contributor to total precipitation, more vertically integrated rainwater ( $t_{qr}$ ) in maritime conditions could indicate more total precipitation on the ground compared to more polluted conditions. However, the melting of frozen hydrometeors as well as the evaporation of rain can vary the rainwater content of a specific atmospheric layer and therefore be decisive for how much rain reaches the ground. For 23 June 2021, it can be seen that over the whole height with relevant amounts of rainwater (about 8 km above ground level) highest values occur for maritime, lowest for continental polluted conditions (exemplary for reference simulations in Fig. 5.15a). This holds also for the lowest layers relevant for the surface precipitation. The rainwater evaporation is stronger for lower CCN concentrations as well (Fig. 5.15b). As a consequence of this, the lines are slightly closer together in the lowest layers. However, they do not intersect. Hail is less relevant as its contribution to the total precipitation is much smaller, but from the vertical profile, also larger

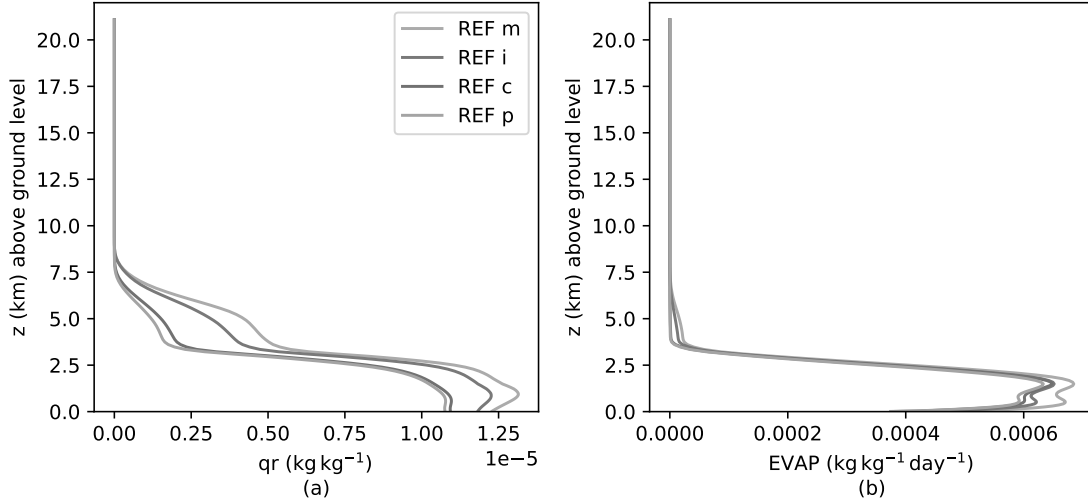


**Figure 5.15:** Spatiotemporal averages over the DE-domain for the vertical profiles of (a) rainwater ( $qr$ ) and (b) evaporation rate of rainwater (EVAP) exemplary for the reference simulations on 23 June 2021. Different colors indicate different CCN concentrations.

hail amount in the lowest layers follows for less pollution (not shown).

Over the course of the day, the reference simulations with less aerosols produce more precipitation until 15 UTC (Fig. 5.16a). Later, the cases with higher pollution have similar or even slightly higher values. In accumulation, there is a larger surface precipitation sum for less aerosols, largest in the intermediate conditions (Fig. 5.16b). As a consequence of the stronger convection with more precipitation in the low CCN cases earlier in the day, a larger amount of the mixed-layer CAPE is consumed. On average, slightly lower values are therefore reached for CAPE in maximum (Fig. 5.16c). The differences are much smaller than between the different wind shear simulations (Fig. 5.5d).

The behavior of total precipitation and CAPE is similar to above also in the other shear cases. For all of them, a larger precipitation amount can be seen for the lower CCN concentrations (Fig. 5.17) similar to the results in Fan et al. (2009). Only in the reference simulations, a slight increase between maritime and intermediate CCN concentrations takes place as it was the case for the weak shear cases in the cited study. However, in the decreased shear cases in the present thesis as well as in the increased shear cases, there is a steady decrease of precipitation with increasing CCN concentration. Note that simulations are done with four different CCN concentrations only, making it difficult to resolve a potential maximum.

With that, 23 June 2021 is very systematic, with increasing precipitation amount for increasing wind shear and decreasing CCN concentration. Only how strong the precipitation varies with changing CCN concentration is not systematically dependent

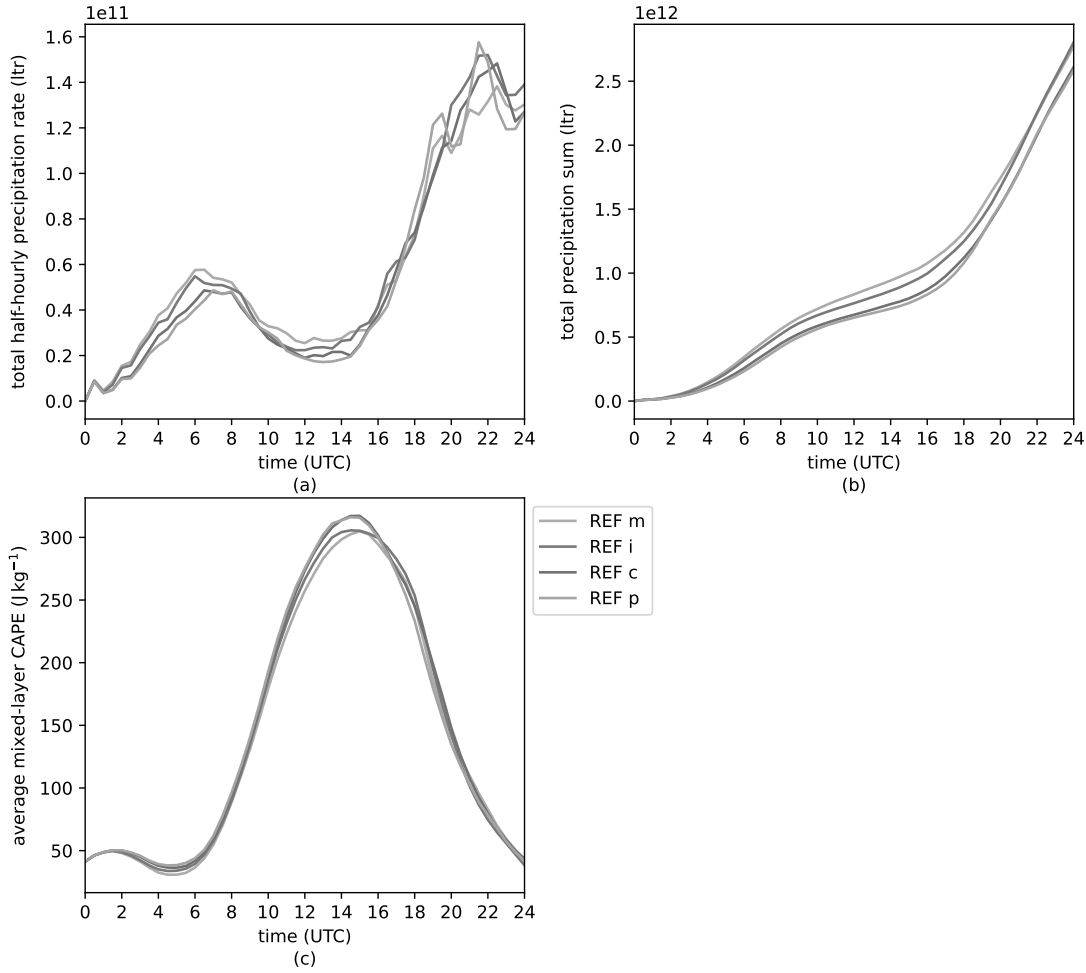


**Figure 5.16:** (a) Half-hourly precipitation rate, (b) total precipitation amount and (c) averaged mixed-layer CAPE inside the DE-domain for the reference simulations on 23 June 2021.

on the vertical wind shear. Overall, the wind shear dependency is much stronger than the CCN dependency. This is also visible from the spatial distributions of the daily precipitation where similar precipitation features occur for the different CCN concentrations (not shown) while large differences could be seen before for different shear cases (e.g., Fig. 5.3).

### 5.2.2 Case of 28 June 2021

On 28 June 2021, the liquid hydrometeors cloud water and rainwater show a similar decrease with increasing CCN concentration as on the first simulation day (Fig. 5.18a). The same is valid for the warm rain production processes autoconversion and accretion (Fig. 5.18b). The CCN dependency of the collision-coalescence is slightly lower than on 23 June, which is also reflected in the dependency of  $t_{qr}$ . For the solid hydrometeors ice and snow, there is an increase, and for graupel a decrease

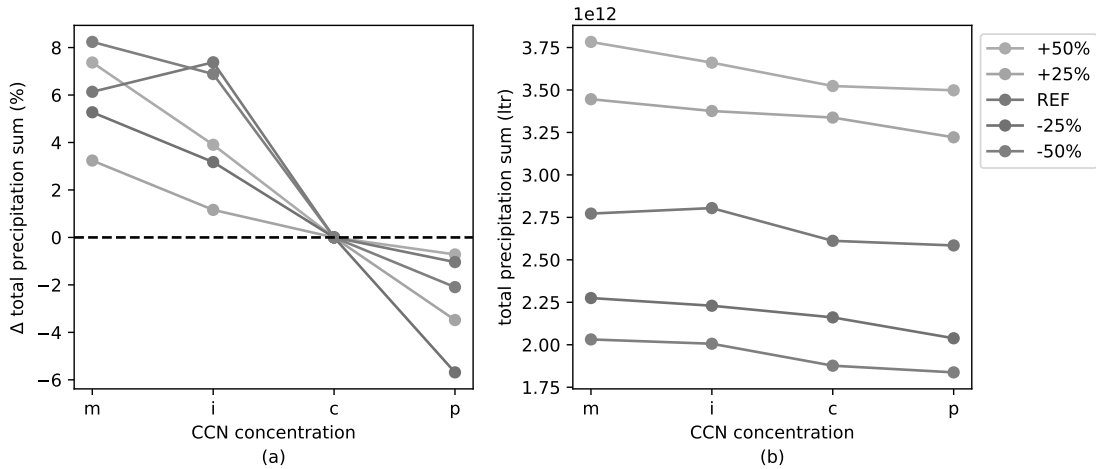


**Figure 5.17:** (a) Percentage deviations of total precipitation sum from the respective simulation with continental CCN concentration and (b) absolute values of the total precipitation sum of the different simulations on 23 June 2021. Different colors indicate different shear cases.

for increasing CCN concentration. However, the sensitivity of the different shear cases differs a bit: for tqi, there is the highest sensitivity for the  $-50\%$ -simulations on 28 June 2021, for which there was the lowest on 23 June. For tq<sub>s</sub>, the differences between the shear cases are smaller than on 23 June. Hail is least systematic, but as before, mainly with an increase for increasing CCN concentration.

Deposition systematically increases with increasing CCN concentration. The differences between the different shear cases are smaller on that day, and the highest sensitivity can be seen for the  $-50\%$ -simulations. This explains the differences compared to 23 June mentioned above for tqi and tq<sub>s</sub>. Riming becomes systematically smaller for increasing CCN concentration. The lowest sensitivity of the  $-50\%$ -simulations is also reflected by the lowest sensitivity in tqg. As on the first simulation day, evaporation decreases with increasing CCN concentration with a slightly higher CCN sensitivity for the weaker shear simulations. Melting shows only a weak CCN dependency. The systematic behavior differs in the simulations (e.g., increase in  $-50\%$ -simulations, decrease in  $-25\%$ -simulations, neither increase nor decrease in  $+25\%$ -simulations).

Even if hydrometeor variables and process rates show similar behavior on 23 and 28 June 2021, the response of total precipitation is different on 28 June (Fig. 5.19). As shown before in section 5.1.2, there is more precipitation for smaller shear on that day. But also the CCN dependency is different compared to 23 June 2021. On the second simulation day, only the reference and the  $-25\%$ -simulations show systematically decreasing precipitation sums with increasing pollution, the latter one

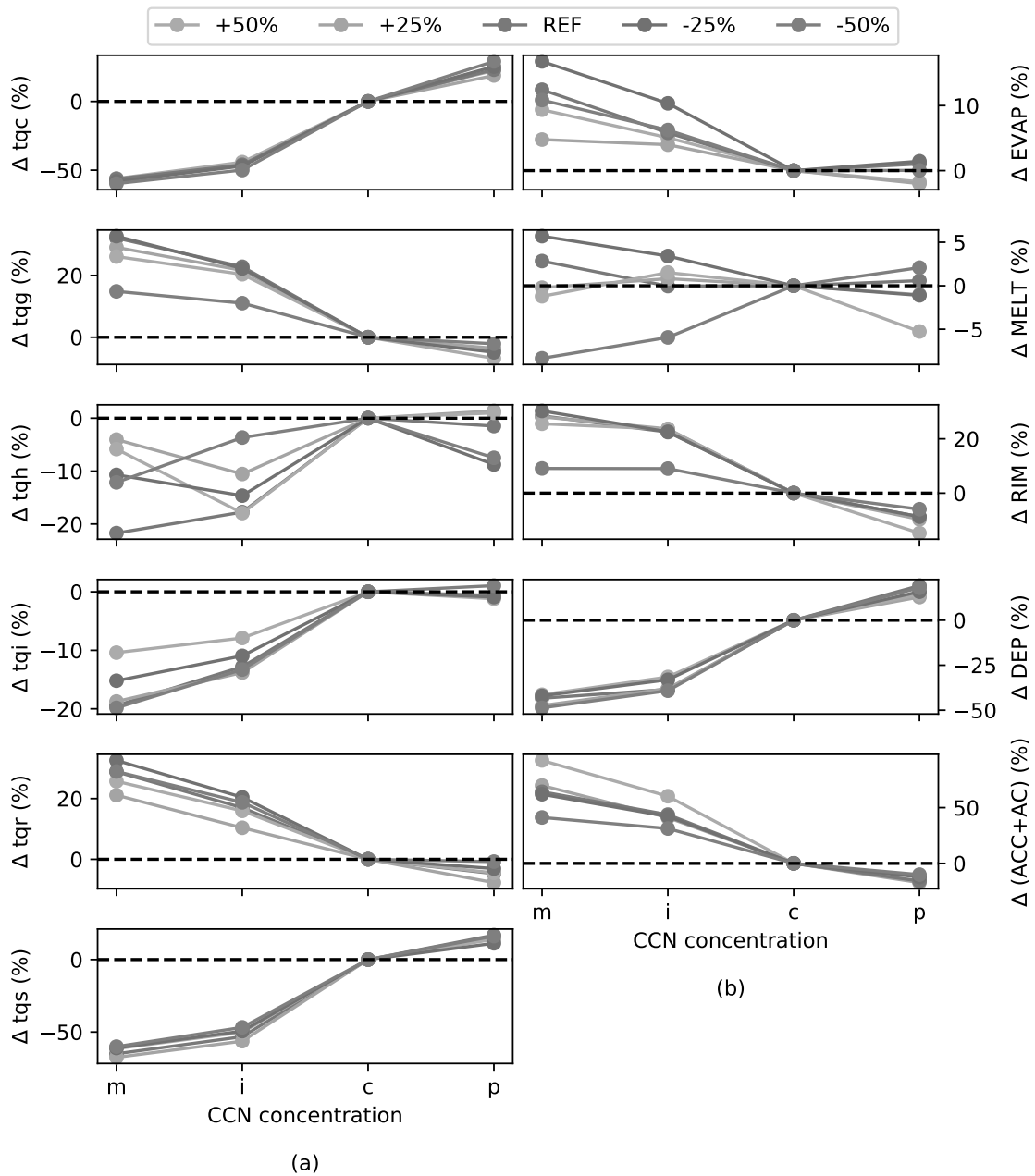


**Figure 5.18:** Same as Fig. 5.14, but for 28 June 2021.

with a higher CCN sensitivity. In both of the increased shear simulations, continental polluted conditions also produce less precipitation than maritime conditions. In between, however, there is both times no steady decrease. The  $-50\%$ -simulations are the only simulations with a systematic increase. Even if the percentage deviations of total precipitation between the different CCN concentrations are smaller than on 23 June, it is striking that the  $-25\%$ -simulations and the  $-50\%$ -simulations give a completely different response for total precipitation when varying the CCN concentration. As on 23 June, varying CCN concentration has a weaker impact on convective precipitation than varying wind shear.

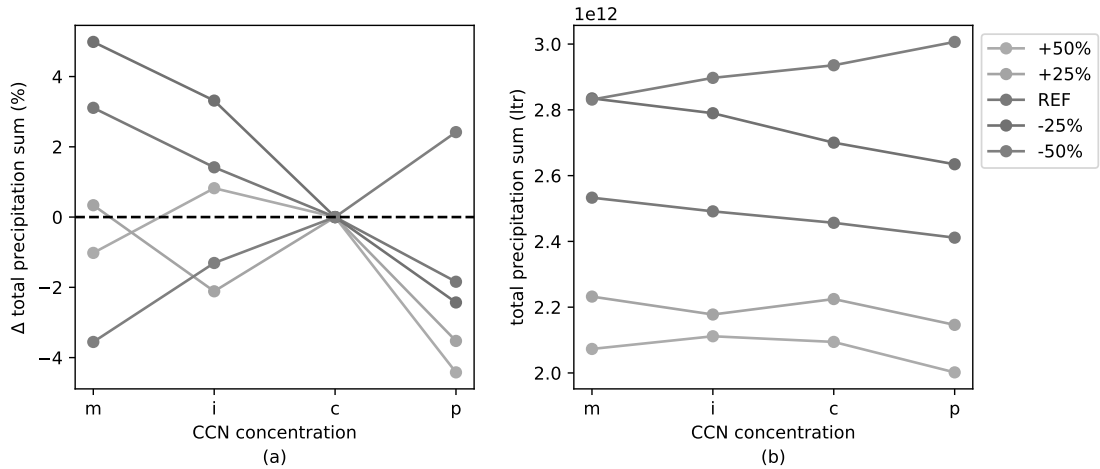


**Figure 5.19:** Same as Fig. 5.17, but for 28 June 2021.

The difference between the  $-50\%$ -simulations and the others is a much earlier onset of precipitation in the former (section 5.1.2 and also Fig. 5.20a). The earlier precipitation is stronger in low CCN concentrations (Fig. 5.20b). As a consequence of this higher precipitation rate, the mixed-layer CAPE reaches higher values in the cases with high CCN concentrations in the afternoon (Fig. 5.20d). This holds for several hours, leading to a higher precipitation rate in the late afternoon and evening for the continental and continental polluted conditions. Due to these higher precipitation rates in the late hours of the day, the lines of the accumulated precipitation in Fig. 5.20c intersect around 21 UTC. For a shorter forecast period, also a systematic decrease of precipitation amount for increasing CCN concentration would have been observed for the  $-50\%$ -simulations. This is an important result as it shows that the simulation period determines whether precipitation increases or decreases for increasing CCN concentration. It is similar for the non-steady decrease of the increased shear simulations where the CCN sensitivity is not completely systematic before but also different for shorter forecast periods (not shown).

### 5.2.3 Case of 22 July 2015

On 22 July 2015, the hydrometeor variables give a similar response on changing CCN concentrations as on the other days (Fig. 5.21a). However, for hail, a clear increase for increasing CCN concentration exists in the stronger wind shear simulations, while no CCN sensitivity takes place in the  $-25\%$ -simulations. For graupel, the CCN dependency is weaker for stronger shear cases (especially for the  $+50\%$ -simulations). For the other simulation days, the dependency was weakest in the  $-50\%$ -simulations.

The decrease in autoconversion and accretion is very similar to the other simulation days (Fig. 5.21b), especially to 28 June 2021. Deposition increases again but with

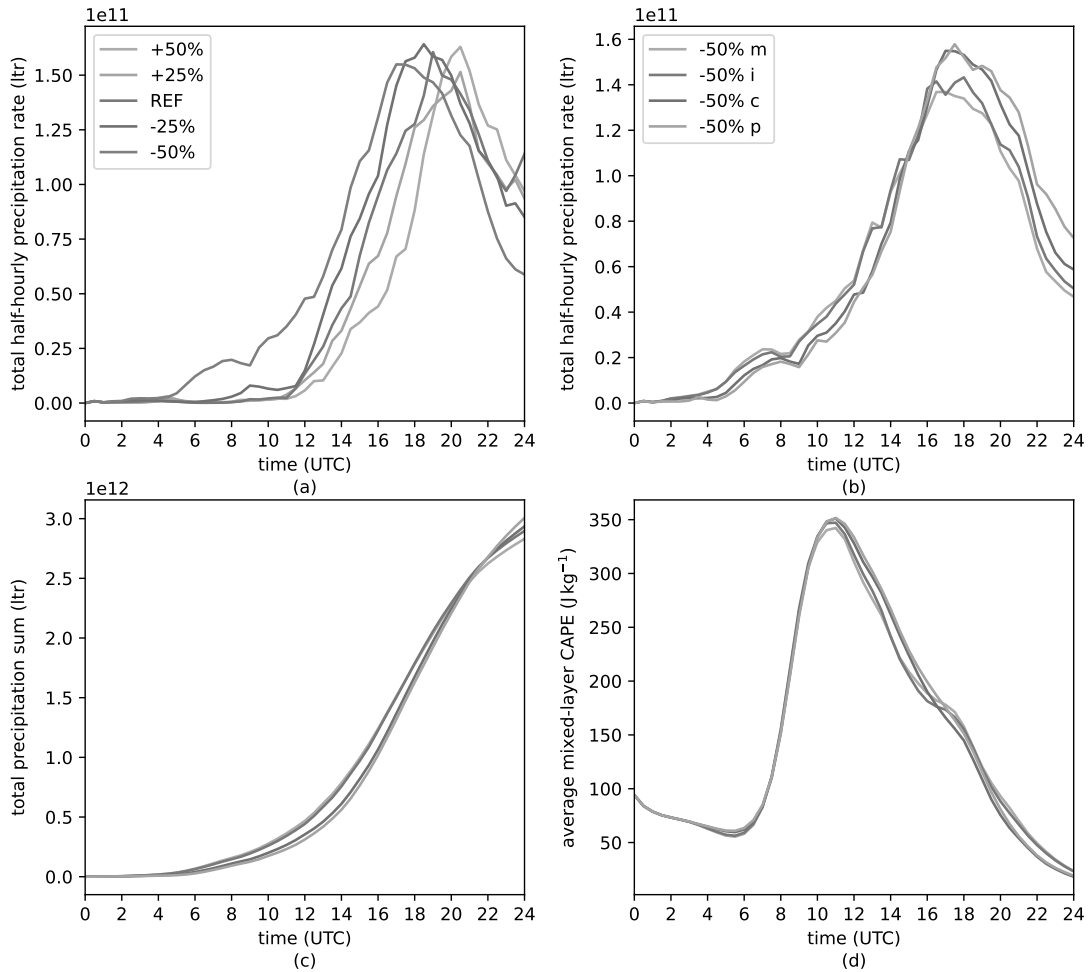


**Figure 5.20:** (a) Half-hourly precipitation rate over DE-domain in simulations with continental CCN concentration; colors indicate different wind shear cases. (b) Half-hourly precipitation rate, (c) accumulated precipitation sum and (d) averaged mixed-layer CAPE inside the DE-domain. Figure (b-d) depict model output for the  $-50\%$ -simulations. Different colors indicate different CCN concentrations, therefore, the legend of subfigure (b) holds also for (c) and (d).

a clearly higher CCN sensitivity of the  $+50\%$ -simulations. The variable deposition consists of positive values for actual deposition and negative values for sublimation in the model simulations. For the  $+50\%$ -simulations, deposition is very small, with slightly negative values for the maritime and intermediate CCN concentrations and slightly positive values for continental and continental polluted conditions. These low values lead to large percentage deviations. Riming decreases for larger CCN amounts. In contrast to 23 June 2021, the sensitivity of the reference and the  $+50\%$ -simulations is reduced. This fits with the weaker decrease of  $t_{qg}$  and the stronger increase of  $t_{qh}$ . Melting increases with increasing CCN concentration. For evaporation, there is only weak CCN dependency with increasing, decreasing or constant behavior dependent on the shear case.

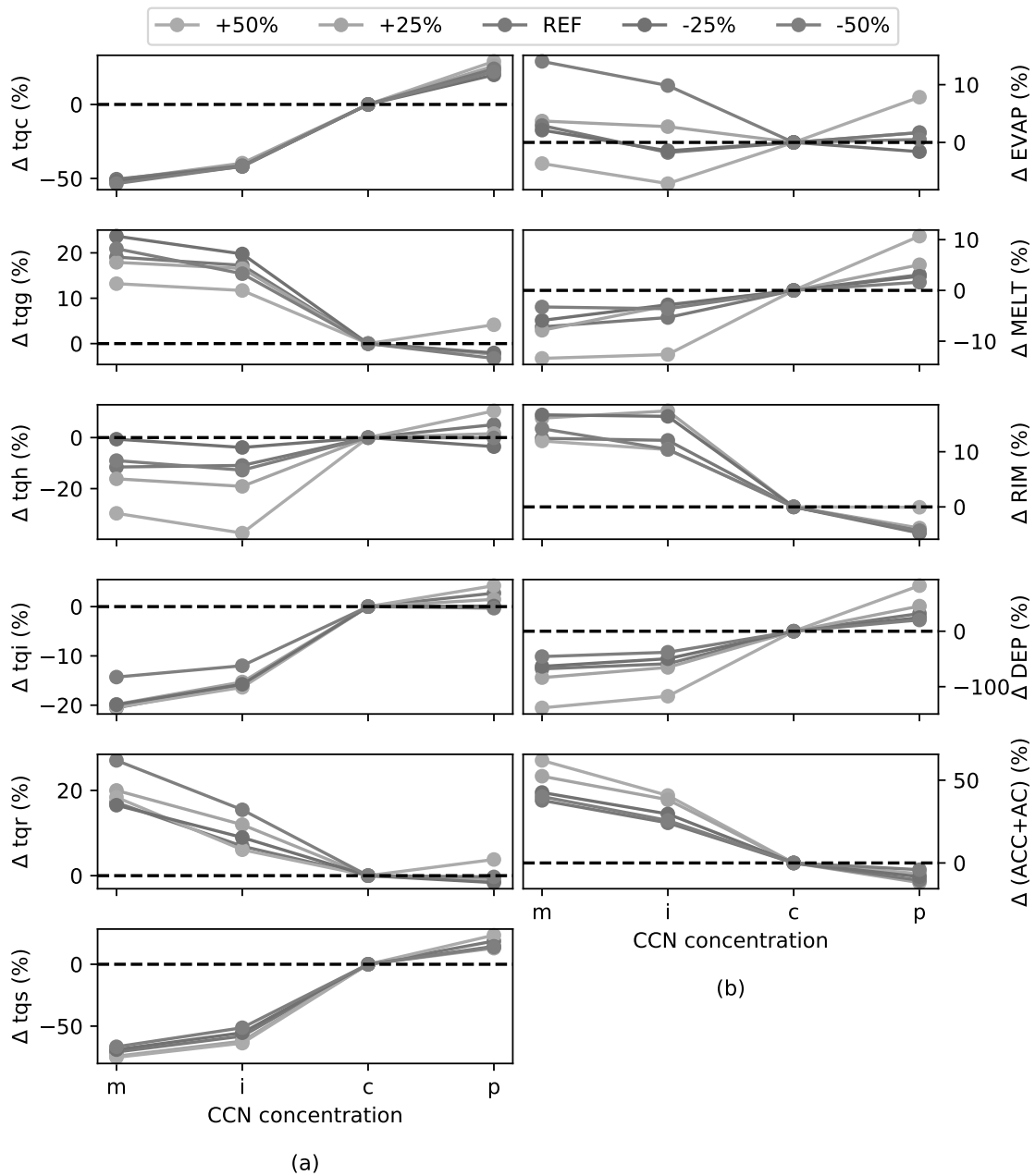


**Figure 5.21:** Same as Fig. 5.14 and Fig. 5.18, but for 22 July 2015.

Even if the results for the vertically integrated rainwater are similar to the other days, the surface precipitation is clearly different (Fig. 5.22). As on 28 June 2021, more precipitation occurs the smaller the wind shear is (Section 5.1.3). For the CCN dependency applies: the higher the CCN concentration, the larger the precipitation amount. This is the exact opposite of 23 June 2021. As on the other days, the aerosol effect is much smaller than the wind shear effect. The highest CCN dependency occurs in the +50%-simulations, but there is no systematic way in which the wind shear affects the CCN sensitivity of the precipitation response. Results to explain the increase in precipitation are shown in the following for these simulations, even

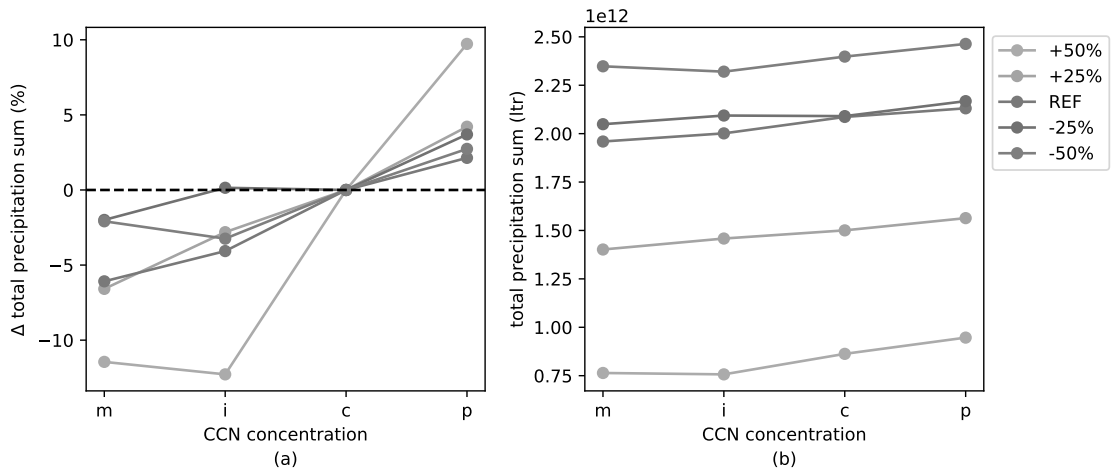


**Figure 5.22:** Same as Fig. 5.17 and Fig. 5.19, but for 22 July 2015.

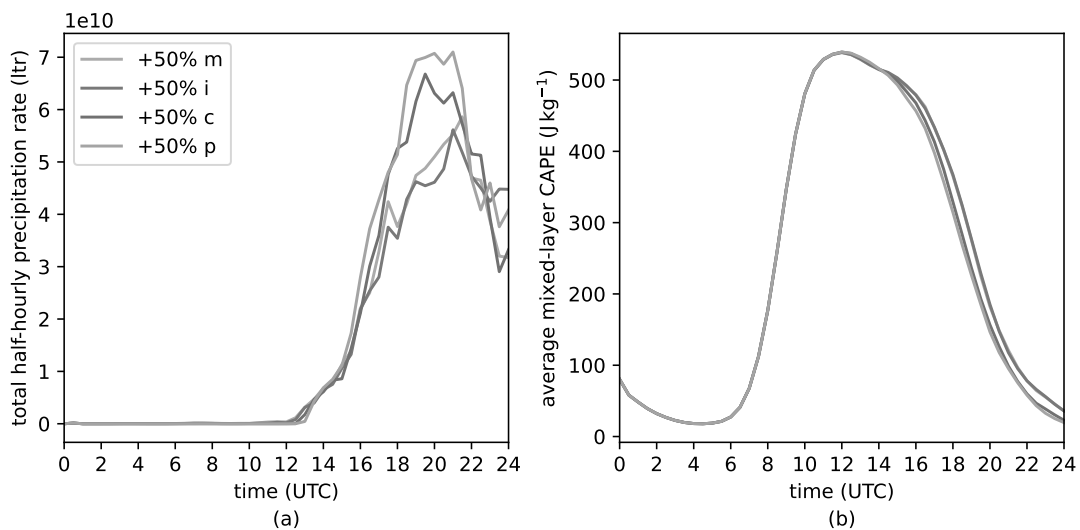


**Figure 5.23:** (a) Half-hourly precipitation rate and (b) averaged mixed-layer CAPE inside the DE-domain in the +50%-simulations on 22 July 2015. Different colors indicate different CCN concentrations.

if it is basically the same in the other shear cases (with the exception of the -50%-simulations).

On 22 July 2015, precipitation starts at the same time in each simulation (Fig. 5.23a). Therefore, no response can be seen in the maximum of the averaged CAPE (Fig. 5.23b). Later in the day, the precipitation rate is higher in more polluted conditions, as more CAPE is consumed in these cases. A larger average CAPE is left in the simulations with low CCN concentrations. This greater consumption of CAPE corresponds to what the cold-phase convective invigoration theory by Rosenfeld et al. (2008) postulates.

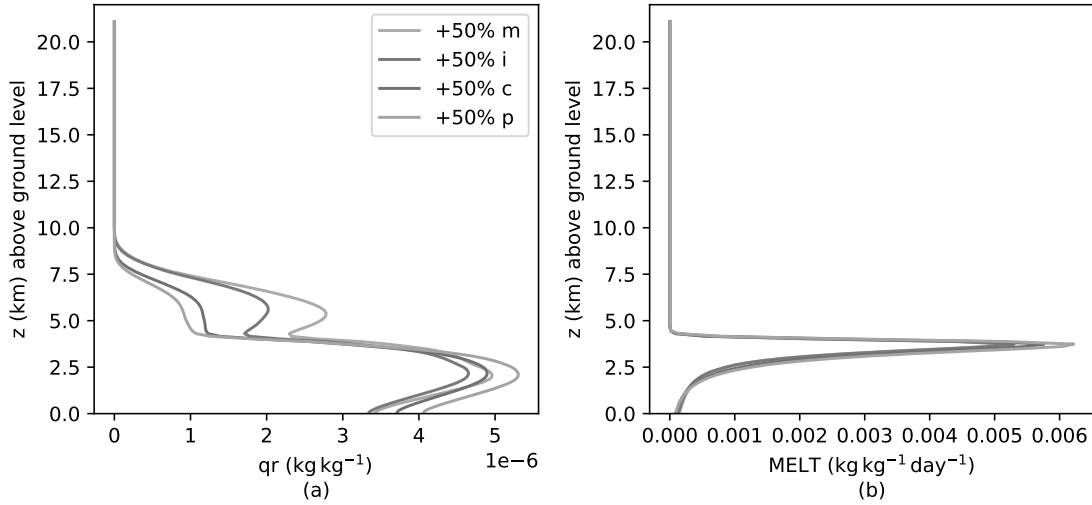


**Figure 5.24:** Spatiotemporal averages over the DE-domain for the vertical profiles of (a) rainwater ( $qr$ ) and (b) rain production rate by melting of all frozen hydrometeors (MELT), exemplary for the +50%-simulations on 22 July 2015.

The averaged profile of  $qr$  has two maxima (Fig. 5.24a). There are various reasons for this structure: first, the profile is spatially averaged over many grid points, which have their maximum at different heights. Second, it is temporally averaged over the whole day during that the height of the maximum  $qr$  shifts. Third, there are also grid points that have this kind of double maximum structure for one specific time point. On average, clearly less rain is above 4 km for the simulations with higher CCN concentrations on average, resulting in the shown decrease of  $tqr$ . Below 4 km, it is the other way round, leading to more surface precipitation the higher the CCN concentration is. In the altitudes of the upper maximum, warm rain processes are clearly stronger for the lower CCN concentrations. Therefore, more rainwater occurs for these conditions at this height. In contrast to the other two simulation days, the rain production rate by melting of the frozen hydrometeors is increased for increasing amounts of CCN. This could be connected with the higher altitude of the  $0^\circ\text{C}$  level over several hours in the afternoon (not shown). However, it results in more rainwater in the lowest layers for higher CCN concentrations. This effect is even stronger in the MOSES-domain.

As mentioned above, the effect of melting on the larger precipitation amounts in more polluted conditions holds for all simulations except for the  $-50\%$ -simulations. In these simulations, precipitation starts a bit earlier for lower CCN concentrations. As CAPE is then consumed earlier, it becomes on average larger for the simulations with higher CCN concentrations. This results in a higher precipitation rate later in the day. Therefore, similar to the  $-50\%$ -simulations on 28 June 2021 (Fig. 5.20) but

in a weakened manner, a negative relation exists between precipitation amount and CCN concentration at first, later a positive one (not shown).

### 5.2.4 General conclusions

For all three simulation days, the hydrometeor variables show a similar CCN dependency. The amounts of cloud water, hail, ice and snow increase with increasing CCN concentration, and the amounts of graupel and rainwater decrease. The exact size of percentage deviations varies from day to day. Which wind shear simulations are most sensitive to varying CCN concentration differ also for the three simulation days. The same applies to the microphysical process rates where an increase for increasing CCN concentration always occurs for the deposition and a decrease for riming and the warm rain processes accretion and autoconversion. The warm rain processes show a higher sensitivity to changing CCN concentration for the stronger shear cases on all three simulation days. Evaporation mainly decreases and melting increases with increasing CCN amount, but not in each simulation.

The response of total precipitation is different for all three simulation days. While a decrease with increasing CCN concentration occurs for all simulations on 23 June 2021, there is an increase for all simulations on 22 July 2015. On 28 June 2021, an increase takes place in the  $-50\%$ -simulations, a non-steady decrease for the increased wind shear simulations and a steady decrease for reference and  $-25\%$ -simulations. With that, no general statements for the precipitation response are found from the simulations of the present work. Likewise, the systematics found by Fan et al. (2009) with decreasing precipitation amounts for increasing CCN concentrations in the strong wind shear cases and with an increase up to an optimum value and a decrease for further aerosol loading in the weak wind shear cases cannot be confirmed in general due to different reasons mentioned above.

## 5.3 Precipitation efficiency

Above, it was shown that the three simulation days respond differently to the changing CCN concentrations for several reasons. However, even if the microphysical process rates show a systematical behavior, some of them decrease, and some of them increase with increasing CCN concentration. Also the CCN sensitivity of the different wind shear cases varies. Therefore, this section deals with the question of how the precipitation varies in the different simulations in relation to the processes which generate precipitation particles.

For that, the precipitation efficiency  $PE$  calculated after Baur et al. (2022) is used:

$$PE = \frac{P}{G}. \quad (5.2)$$

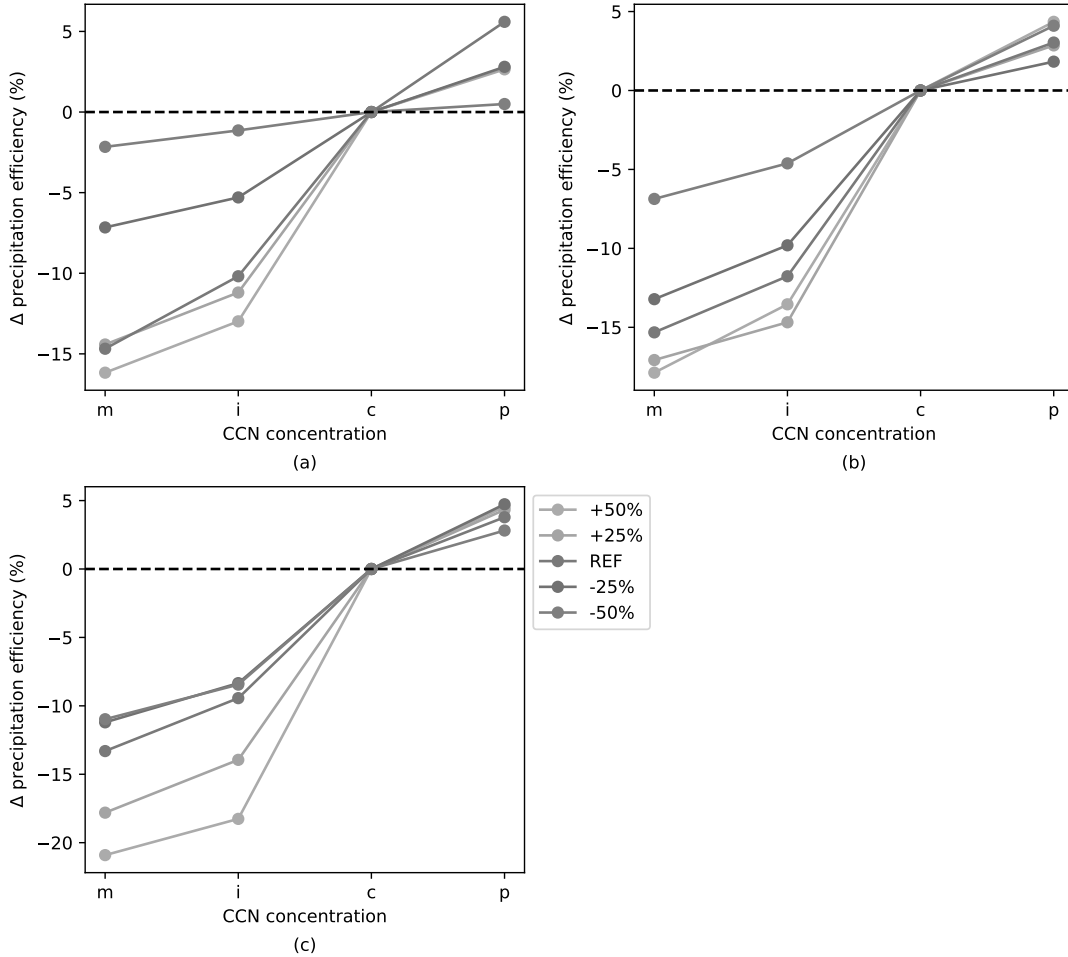


**Figure 5.25:** Relative change to the respective simulation with continental CCN concentration for precipitation efficiency on the three simulation days (a) 23 June 2021, (b) 28 June 2021 and (c) 22 July 2015. Calculation is done with 24-hourly precipitation and generation term values. Different colors indicate different shear cases.

In that equation,  $P$  describes precipitation and  $G$  the generation terms deposition (including sublimation), riming, autoconversion and accretion. All variables are used accumulated over the simulation period of 24 hours. As in Baur et al. (2022), the precipitation efficiency is dependent on the CCN concentration with increasing values for increasing CCN concentration (Fig. 5.25). This holds for all simulations, even for them with decreasing precipitation amounts. The CCN sensitivity is mainly higher the stronger the wind shear is on all three simulation days.

For all three days, three of four generation terms (riming, autoconversion and accretion) decrease with increasing CCN concentration, only deposition increases. For most of the simulations, the decrease of the absolute values of the warm rain processes autoconversion and accretion already exceeds the increase of the deposition. An additional decrease of the riming leads to an even larger decrease. As a general

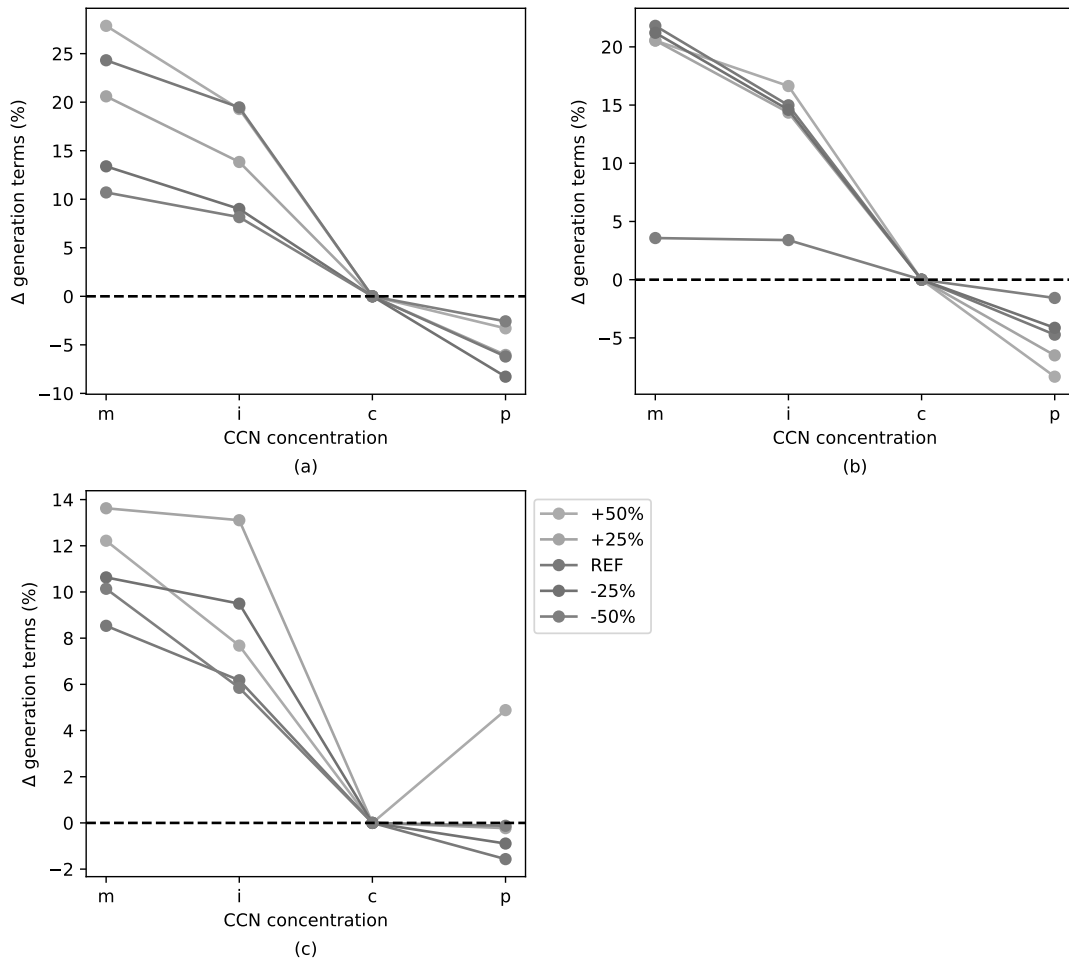


**Figure 5.26:** Relative change to the respective simulation with continental CCN concentration for the sum of generation terms (deposition, riming, autoconversion and accretion) on the three simulation days (a) 23 June 2021, (b) 28 June 2021 and (c) 22 July 2015.

conclusion, it follows from the simulations of all three days that the rain generation is reduced with increasing CCN concentration.

On the first simulation day, 23 June 2021, there is a strong decrease of generation terms for increasing CCN concentration. This high sensitivity is necessary to invert the decrease of precipitation sum in an increase of precipitation efficiency. The absolute values of generation terms are clearly higher the greater the wind shear is, as all four generation terms show this shear sensitivity (not shown), leading to the larger precipitation sums found in section 5.2.1. The decrease of generation terms for increasing CCN concentration is also clearly stronger for the strong wind shear cases and becomes visible in the relative changes (Fig. 5.26a) despite the larger absolute values. This systematic stronger decrease of the generation terms is a consequence of the stronger decrease of the riming rate and the warm rain processes, and explains the systematic behavior in the precipitation efficiency with a stronger increase for

greater wind shear (Fig. 5.25a).

On 28 June 2021, the generation terms are slightly larger for weaker wind shear, however, with only much smaller differences compared to 23 June 2021. Only the  $-50\%$ -simulations do not fit with this systematic behavior: the decrease for increasing CCN concentration is only weak, resulting in lowest values of  $G$  for low CCN concentrations and highest values of  $G$  for high CCN concentrations compared to the other shear cases. This weak decrease for increasing CCN concentration in the  $-50\%$ -simulations is partly a result of a weaker decrease in the warm rain processes but mainly a result of the clearly weaker CCN sensitivity of riming (Fig. 5.18b). However, as the precipitation sum increases with increasing CCN concentration for this shear case, an increase in precipitation efficiency is the consequence. In the other four shear cases, a slightly stronger decrease for increasing CCN concentration occurs the greater the wind shear is (Fig. 5.26b) as a consequence of the stronger decrease in the warm rain processes. This systematic behavior in turn results in the stronger increase of precipitation efficiency with increasing CCN concentration for greater wind shear (Fig. 5.25b).

On 22 July 2015, the reason for the systematic response in precipitation efficiency is slightly different. The decrease in the generation terms for increasing CCN concentration is weaker than on the other days. However, in combination with the increasing precipitation sums for increasing CCN concentrations, increasing precipitation efficiency is again the result on this day. The wind shear sensitivity in the generation terms is not as systematic as on the other days (Fig. 5.26c). For the  $+50\%$ -simulations, there is no steady decrease as the generation terms are larger in the continental polluted than in the continental conditions. Note here, that the decrease in these simulations is only that strong between maritime and continental conditions as a consequence of much lower absolute values in  $G$ . However, as the precipitation sum increase is strongest for these simulations, the strongest increase in precipitation efficiency results for the  $+50\%$ -simulations. Also for the other shear cases, a combination of CCN sensitivity in precipitation and generation term response explains the systematic behavior of the precipitation efficiency for varying wind shear.



## 6. Conclusion and discussion

Clouds and precipitation are influenced to a large extent by ACI, which arise from many different microphysical and thermodynamical processes. In the past years, the vertical wind shear was found to have a large impact on how aerosols affect precipitation. From idealized simulations in Fan et al. (2009), it followed that increasing aerosol concentration lead to weaker convection with less precipitation in environments of strong wind shear. Under weak wind shear, greater aerosol loading invigorates convection leading to larger amounts of precipitation up to an optimum CCN concentration. For further increased aerosol loading, the convection becomes weaker also in the weak wind shear environment.

Therefore, the aim of this study was to investigate the impact of wind shear on ACI and convective precipitation using real-case simulations. The simulations were done with a 1-km ICON grid for two days with convective activity of the Swabian MOSES field campaign, 23 June 2021 and 28 June 2021, and one day with supercells over Germany from the data set of Tonn et al. (2023), 22 July 2015. For each simulation day, twenty simulations were performed. The first four simulations were done with four different CCN concentrations (maritime, intermediate, continental, continental polluted) and reference wind shear. Afterwards, the wind shear of the initial data was increased and decreased in two ways, and simulations with the four different CCN concentrations were repeated for each case of wind shear. The model output over Germany and some bordering regions was analyzed in two steps: first, the impact of wind shear on convective precipitation was studied, while CCN dependency was excluded by working only with the simulations with continental CCN concentration. In the second step, it was also analyzed how thermodynamics and microphysical process rates develop for varying CCN concentrations in the different wind shear cases.

The following conclusions can be drawn from the analyses of the model output of the ICON real-case simulations:

- The three convective active days do not provide a consistent result on how the precipitation amounts depend on vertical wind shear. The precipitation response is systematic in general, however, with increasing amounts on 23 June 2021 and decreasing amounts on 28 June 2021 and 22 July 2015 for increasing wind shear.
- The potential for convection (expressed by averaged mixed-layer CAPE) is always higher the stronger the wind shear is. The differences are largest on 23 June 2021, where the different potential is also reflected in the precipitation amount. On the other days, a larger energy barrier (expressed by averaged

CIN) in the convective relevant areas is responsible for the fact that the convection potential can not be used.

- The vertically integrated hydrometeor variables behave similarly for varying CCN concentrations on the three simulation days. The amounts of cloud water, cloud ice, snow and hail increase for increasing CCN concentration, and the amounts of graupel and rainwater decrease. Which wind shear case has the largest CCN sensitivity is different for the three days.
- The vertically integrated microphysical process rates also behave similarly for varying CCN concentrations on the three simulation days. The warm rain processes accretion and autoconversion decrease for increasing CCN concentration as well as riming. Deposition increases for increasing CCN concentration. Evaporation mainly increases and melting mainly decreases, however, not in each simulation. For accretion and autoconversion, a lower CCN sensitivity for weaker wind shear cases occurs. The same is the case for riming on 23 June 2021 and 28 June 2021.
- As for the dependency of precipitation on the wind shear, no consistent result for the CCN dependency of convective precipitation follows from the three simulation days. On 23 June 2021, precipitation amounts decrease, and on 22 July 2015, they increase for increasing CCN concentration. On 28 June 2021, the results are different for the different wind shear cases. However, on this day, simulations show a similar behavior as on 23 June 2021 for the first roughly 20 hours of the day. For a longer forecast period, the CCN dependency reverses.
- On all three simulation days, there is no systematic behavior of how vertical wind shear influences the CCN sensitivity of the precipitation response.
- The precipitation amounts clearly vary stronger for varying wind shear than for varying CCN concentration on all three simulation days.
- A clear systematic behavior is found for the precipitation efficiency. For all three simulation days, the precipitation efficiency increases with increasing CCN concentration as in Baur et al. (2022). This effect is stronger the greater the vertical wind shear is, which is a consequence of a stronger sensitivity in the generation terms on 23 and 28 June 2021. On 22 July 2015, a combination of precipitation and generation terms response leads to the same behavior of precipitation efficiency as on the other days.

There are differences in the methodology of the ICON real-case simulations and the idealized simulations of Fan et al. (2009) leading to the different precipitation responses. Only four different CCN concentrations are used in the present thesis.

---

This makes it difficult to resolve a potential maximum for weak wind shear cases when the precipitation amounts decrease with increasing CCN concentration, as it occurs in the cited study. The forecast period also plays a role. In Fan et al. (2009), simulations were run for only 3 hours, whereas in this thesis, convective days are simulated for the full 24 hours of the day. It was shown above that the simulation period is highly important for the CCN sensitivity as the results sometimes reverse in the last hours of the day.

The output of the real-case simulations in this work makes it possible to explain the evolution of atmospheric conditions as a whole, leading to the different responses in precipitation. With that, it becomes clear that the initiation of convection is more individual from day to day than expected from the idealized simulations by Fan et al. (2009). Therefore, and as the forecast of such convective events is of great importance, a study with further real-case simulations of convective active days is recommended for future research. For that, data from the Swabian MOSES follow-up campaign of the summer of 2023 could be used. It might be beneficial to better resolve the range between clean and polluted CCN concentrations in that further simulations. Also, it might be valuable to look at more individual cell development in smaller areas and smaller time frames, even if this has proved difficult in the process of the present work, after the cells are created at somewhat different times and in somewhat different places. In a further study, it might also be interesting to investigate how the results for the simulation days of this work change when not only the wind speed but also the wind direction of the initial data is changed.



# Bibliography

- Abbott, T. H. and T. W. Cronin, 2021: Aerosol invigoration of atmospheric convection through increases in humidity. *Science*, **371 (6524)**, 83–85.
- Altaratz, O., I. Koren, T. Reisin, A. Kostinski, G. Feingold, Z. Levin, and Y. Yin, 2008: Aerosols’ influence on the interplay between condensation, evaporation and rain in warm cumulus cloud. *Atmospheric Chemistry and Physics*, **8 (1)**, 15–24.
- Altaratz, O., I. Koren, L. Remer, and E. Hirsch, 2014: Cloud invigoration by aerosols—Coupling between microphysics and dynamics. *Atmospheric Research*, **140**, 38–60.
- Barthlott, C. and C. Hoose, 2018: Aerosol effects on clouds and precipitation over central Europe in different weather regimes. *Journal of the Atmospheric Sciences*, **75 (12)**, 4247–4264.
- Barthlott, C., A. Zarboo, T. Matsunobu, and C. Keil, 2022a: Impacts of combined microphysical and land-surface uncertainties on convective clouds and precipitation in different weather regimes. *Atmospheric Chemistry and Physics*, **22 (16)**, 10 841–10 860.
- Barthlott, C., A. Zarboo, T. Matsunobu, and C. Keil, 2022b: Importance of aerosols and shape of the cloud droplet size distribution for convective clouds and precipitation. *Atmospheric Chemistry and Physics*, **22 (3)**, 2153–2172.
- Barthlott, C., et al., 2023: The impact of aerosols and model grid spacing on a supercell storm from Swabian MOSES 2021. *Quarterly Journal of the Royal Meteorological Society*, submitted.
- Baur, F., C. Keil, and C. Barthlott, 2022: Combined effects of soil moisture and microphysical perturbations on convective clouds and precipitation for a locally forced case over Central Europe. *Quarterly Journal of the Royal Meteorological Society*, **148 (746)**, 2132–2146.
- Bolton, D., 1980: The computation of equivalent potential temperature. *Monthly weather review*, **108**, 1046–1053.
- Buizza, R., 2019: Chapter 2 – Ensemble Forecasting and the Need for Calibration. *Statistical Postprocessing of Ensemble Forecasts*, Elsevier, 15–48.
- Bunkers, M. J., B. A. Klimowski, J. W. Zeitler, R. L. Thompson, and M. L. Weisman, 2000: Predicting supercell motion using a new hodograph technique. *Weather and Forecasting*, **15**, 61–79.
- Byers, H. R. and R. R. J. Braham, 1948: Thunderstorm structure and circulation. *Journal of Meteorology*, **5**, 71–86.

- Cotton, W. R. and R. Walko, 2021: Examination of aerosol-induced convective invigoration using idealized simulations. *Journal of the Atmospheric Sciences*, **78** (1), 287–298.
- Cui, Z., S. Davies, K. Carslaw, and A. Blyth, 2011: The response of precipitation to aerosol through riming and melting in deep convective clouds. *Atmospheric Chemistry and Physics*, **11** (7), 3495–3510.
- Doswell, C. A., 1985: *The Operational Meteorology of Convective Weather. Storm Scale Analysis. Vol. 2*. Air Weather Service, Scott Air Force Base, Belleville, USA, 240 pp.
- DWD, 2023: Radargestützte Analysen stündlicher Niederschlagshöhen im Echtzeit- betrieb für Deutschland (RADOLAN) und Mitteleuropa (RADOLAN-ME). URL: [https://www.dwd.de/DE/leistungen/radolan/radarniederschlagsprodukte/radolan Kurzbeschreibung\\_pdf.pdf?\\_\\_blob=publicationFile&v=8](https://www.dwd.de/DE/leistungen/radolan/radarniederschlagsprodukte/radolan Kurzbeschreibung_pdf.pdf?__blob=publicationFile&v=8), accessed on 11 November 2023.
- Emanuel, K. A., 1994: *Atmospheric Convection*. Oxford University Press, Inc., New York, USA, 592 pp.
- Fan, J., L. R. Leung, D. Rosenfeld, Q. Chen, Z. Li, J. Zhang, and H. Yan, 2013: Microphysical effects determine macrophysical response for aerosol impacts on deep convective clouds. *Proceedings of the National Academy of Sciences*, **110** (48), E4581–E4590.
- Fan, J., Y. Wang, D. Rosenfeld, and X. Liu, 2016: Review of aerosol–cloud interactions: Mechanisms, significance, and challenges. *Journal of the Atmospheric Sciences*, **73** (11), 4221–4252.
- Fan, J., et al., 2009: Dominant role by vertical wind shear in regulating aerosol effects on deep convective clouds. *Journal of Geophysical Research: Atmospheres*, **114** (D22).
- Hande, L., C. Engler, C. Hoose, and I. Tegen, 2015: Seasonal variability of Saharan desert dust and ice nucleating particles over Europe. *Atmospheric Chemistry and Physics*, **15** (8), 4389–4397.
- Heise, E., B. Ritter, and R. Schrodin, 2006: Operational implementation of the multilayer soil model. Technical Report 9. URL: <https://www.cosmo-model.org/content/model/cosmo/techReports/docs/techReport09.pdf>, accessed on 11 November 2023, 19 pp.
- Iribarne, J. V. and H.-R. Cho, 1980: *Atmospheric Physics*. D. Reidel Publishing Company, Dordrecht, Niederlande, 212 pp.
- Kalthoff, N., et al., 2013: KITcube – a mobile observation platform for convection studies deployed during HyMeX. *Meteorologische Zeitschrift*, **22** (6), 633–647.
- Kärcher, B., J. Hendricks, and U. Lohmann, 2006: Physically based parameterization of cirrus cloud formation for use in global atmospheric models. *Journal of Geophysical Research: Atmospheres*, **111** (D1).
- Kärcher, B. and U. Lohmann, 2002: A parameterization of cirrus cloud formation: Homogeneous freezing of supercooled aerosols. *Journal of Geophysical Research: Atmospheres*, **107** (D2), AAC–4.

- Kirshbaum, D. J., B. Adler, N. Kalthoff, C. Barthlott, and S. Serafin, 2018: Moist orographic convection: Physical mechanisms and links to surface-exchange processes. *Atmosphere*, **9** (3), 80.
- Kohler, M., N. Kalthoff, and C. Kottmeier, 2010: The impact of soil moisture modifications on CBL characteristics in West Africa: A case-study from the AMMA campaign. *Quarterly Journal of the Royal Meteorological Society*, **136** (S1), 442–455.
- Kraus, H., 2004: *Die Atmosphäre der Erde: Eine Einführung in die Meteorologie*. Springer-Verlag Berlin Heidelberg, Deutschland, 422 pp.
- Kunz, M., U. Blahak, J. Handwerker, M. Schmidberger, H. J. Punge, S. Mohr, E. Fluck, and K. M. Bedka, 2018: The severe hailstorm in southwest Germany on 28 July 2013: characteristics, impacts and meteorological conditions. *Quarterly Journal of the Royal Meteorological Society*, **144**, 231–250.
- Kunz, M., et al., 2022: Swabian MOSES 2021: An interdisciplinary field campaign for investigating convective storms and their event chains. *Frontiers in Earth Science*, 1886.
- Lamb, D. and J. Verlinde, 2011: *Physics and Chemistry of Clouds*. Cambridge University Press, 584 pp.
- Lemon, L. R. and C. A. Doswell, 1979: Severe thunderstorm evolution and mesocyclone structure as related to tornadogenesis. *Monthly Weather Review*, **107**, 1184–1197.
- Leuenberger, D., M. Koller, O. Fuhrer, and C. Schär, 2010: A generalization of the SLEVE vertical coordinate. *Monthly Weather Review*, **138** (9), 3683–3689.
- Lin, J., et al., 2022: Atmospheric convection. *Atmosphere-Ocean*, **60** (3-4), 422–476.
- Maddox, R. A., 1980: Mesoscale convective complexes. *Bulletin of the American Meteorological Society*, **61**, 1374–1387.
- Magnusson, L. and E. Källén, 2013: Factors influencing skill improvements in the ECMWF forecasting system. *Monthly Weather Review*, **141** (9), 3142–3153.
- Markowski, P. and Y. Richardson, 2010: *Mesoscale Meteorology in Midlatitudes*. John Wiley & Sons, Ltd., Publication, Chichester, Vereinigtes Königreich, 407 pp.
- Mlawer, E. J., S. J. Taubman, P. D. Brown, M. J. Iacono, and S. A. Clough, 1997: Radiative transfer for inhomogeneous atmospheres: RRTM, a validated correlated-k model for the longwave. *Journal of Geophysical Research: Atmospheres*, **102** (D14), 16 663–16 682.
- Munich Re, 2020: Medieninformationen, Münchener Rückversicherungs-Gesellschaft, München, Deutschland. URL: <https://www.munichre.com/de/unternehmen/media-relations/medieninformationen-und-unternehmensnachrichten/medieninformationen/2020/milliardenschaeden-praegen-bilanz-naturkatastrophen-2019.html#1480610047>, accessed on 11 November 2023.
- Öktem, R., D. M. Roms, and A. C. Varble, 2023: No warm-phase invigoration of convection detected during GoAmazon. *Journal of the Atmospheric Sciences*, **80** (10), 2345–2364.

- Raschendorfer, M., 2001: The new turbulence parameterization of LM. COSMO-Newsletter. 89–97 pp., URL: [http://www.cosmo-model.org/content/model/documentation/newsLetters/newsLetter01/newsLetter\\_01.pdf](http://www.cosmo-model.org/content/model/documentation/newsLetters/newsLetter01/newsLetter_01.pdf), accessed on 11 November 2023, 115 pp.
- Reinert, D., et al., 2023: DWD Database Reference for the Global and Regional ICON and ICON-EPS Forecasting System. URL: [https://www.dwd.de/SharedDocs/downloads/DE/modelldokumentationen/nwv/icon/icon\\_dbbeschr\\_aktuell.html](https://www.dwd.de/SharedDocs/downloads/DE/modelldokumentationen/nwv/icon/icon_dbbeschr_aktuell.html), accessed on 11 November 2023, 126 pp.
- Rosenfeld, D., U. Lohmann, G. B. Raga, C. D. O’Dowd, M. Kulmala, S. Fuzzi, A. Reissell, and M. O. Andreae, 2008: Flood or drought: how do aerosols affect precipitation? *Science*, **321** (5894), 1309–1313.
- Schneider, L., C. Barthlott, A. I. Barrett, and C. Hoose, 2018: The precipitation response to variable terrain forcing over low mountain ranges in different weather regimes. *Quarterly Journal of the Royal Meteorological Society*, **144** (713), 970–989.
- Schneider, L., C. Barthlott, C. Hoose, and A. I. Barrett, 2019: Relative impact of aerosol, soil moisture, and orography perturbations on deep convection. *Atmospheric Chemistry and Physics*, **19** (19), 12 343–12 359.
- Segal, Y. and A. Khain, 2006: Dependence of droplet concentration on aerosol conditions in different cloud types: Application to droplet concentration parameterization of aerosol conditions. *Journal of Geophysical Research: Atmospheres*, **111** (D15).
- Seifert, A. and K. D. Beheng, 2006: A two-moment cloud microphysics parameterization for mixed-phase clouds. Part 1: Model description. *Meteorology and atmospheric physics*, **92** (1-2), 45–66.
- Seifert, A., C. Köhler, and K. Beheng, 2012: Aerosol-cloud-precipitation effects over Germany as simulated by a convective-scale numerical weather prediction model. *Atmospheric Chemistry and Physics*, **12** (2), 709–725.
- SwissRe, 2014: Sigma: Natural catastrophes and man-made disasters in 2013. Swiss Re Economic Research and Consulting, Zürich, Schweiz.
- Tao, W.-K., X. Li, A. Khain, T. Matsui, S. Lang, and J. Simpson, 2007: Role of atmospheric aerosol concentration on deep convective precipitation: Cloud-resolving model simulations. *Journal of Geophysical Research: Atmospheres*, **112** (D24).
- The ATMO Hub of KIT, 2023: Measurement campaigns/Swabian MOSES 2021. URL: <https://www.atmohub.kit.edu/105.php>, accessed on 11 November 2023.
- Tonn, M., J. Wilhelm, and M. Kunz, 2023: Evaluating Bunkers’ storm motion of hail-producing supercells and their storm-relative helicity in Germany. *Meteorologische Zeitschrift*, **32** (3), 229–243.
- Trapp, R. J., 2013: *Mesoscale-Convective Processes in the Atmosphere*. Cambridge University Press, Cambridge, Vereinigtes Königreich, 346 pp.
- Twomey, S., 1974: Pollution and the planetary albedo. *Atmospheric Environment (1967)*, **8** (12), 1251–1256.

- Twomey, S., 1977: The influence of pollution on the shortwave albedo of clouds. *Journal of the atmospheric sciences*, **34** (7), 1149–1152.
- Vallis, G. K., 2017: *Atmospheric and Oceanic Fluid Dynamics*. Cambridge University Press, Cambridge, Vereinigtes Königreich, 946 pp.
- Wilhelm, J., S. Mohr, H. J. Punge, B. Mühr, M. Schmidberger, J. E. Daniell, K. M. Bedka, and M. Kunz, 2020: Severe thunderstorms with large hail across Germany in June 2019. *Weather*, **76** (7), 228–237.
- Zängl, G., D. Reinert, P. Rípodas, and M. Baldauf, 2015: The ICON (ICOsahedral Non-hydrostatic) modelling framework of DWD and MPI-M: Description of the non-hydrostatic dynamical core. *Quarterly Journal of the Royal Meteorological Society*, **141** (687), 563–579.



# Acknowledgement

I would like to express my sincere thanks to my supervisor Christian Barthlott who helped me a lot with the setup of my computer and digital workplace and taught me how to do my first own model simulations. I could also come into his room at any time if I needed feedback on the results or a discussion about the further course of the work in the past year. Thank you for that!

Further, I would like to thank my advisors Corinna Hoose and Michael Kunz for their helpful feedback when I presented my progress to them from time to time. I would also like to thank the members of their working groups, cloud physics and atmospheric risks, respectively, for some discussions or feedback.



# Erklärung

Ich versichere wahrheitsgemäß, die Arbeit selbstständig verfasst, alle benutzten Hilfsmittel vollständig und genau angegeben und alles kenntlich gemacht zu haben, was aus Arbeiten anderer unverändert oder mit Abänderungen entnommen wurde sowie die Satzung des KIT zur Sicherung guter wissenschaftlicher Praxis in der jeweils gültigen Fassung beachtet zu haben.

Karlsruhe, den 11.11.2023

Mathis Tonn